COMENIUS UNIVERSITY IN BRATISLAVA
FACULTY OF MATHEMATICS, PHYSICS
AND INFORMATICS

STUDY OF NEUTRON-DEFICIENT POLONIUM ISOTOPES

Dissertation Thesis

2016 **Mgr. Boris Andel**

COMENIUS UNIVERSITY IN BRATISLAVA
FACULTY OF MATHEMATICS, PHYSICS
AND INFORMATICS

STUDY OF NEUTRON-DEFICIENT POLONIUM ISOTOPES

Dissertation Thesis

Study Program: Nuclear and Subnuclear Physics
Branch of Study: Nuclear and Subnuclear Physics
Department: Department of Nuclear Physics and Biophysics
Supervisor: doc. Mgr. Stanislav Antalic, PhD.

Bratislava 2016 **Mgr. Boris Andel**

78651341

Comenius University in Bratislava
Faculty of Mathematics, Physics and Informatics

THESIS ASSIGNMENT

Name and Surname: Mgr. Boris Andel
Study programme: Nuclear and Subnuclear Physics (Single degree study, Ph.D. III. deg., full time form)
Field of Study: Nuclear And Subnuclear Physics
Type of Thesis: Dissertation thesis
Language of Thesis: English
Secondary language: Slovak

Title: Study of neutron-deficient polonium isotopes

Literature: P.E. Hodgeson, E. Gadioli and E. Gadioli Erba, Introductory Nuclear Physics, Oxford University Press, 1997.
K. Heyde, Basic Ideas and Concepts in Nuclear Physics, Institute of Physics Publishing, 3rd edition 2004.
R. Casten, Nuclear Structure from a Simple Perspective, Oxford University Press, 1990.
K. S. Krane, Introductory Nuclear Physics, John Wiley & Sons, 1988.
Články publikované v karentovaných časopisoch.

Aim: Proposed PhD project is aimed at analysis of experimental data and following physical interpretation. Experimental measurements will be performed at the SHIP separator at GSI Darmstadt (Germany) and experimental facility ISOLDE at CERN (Switzerland). Presently, we have proposals of measurements that were accepted at both experiments and we have available data as well. Primary objective of the dissertation thesis is the analysis and interpretation of spectroscopic data for neutron-deficient polonium isotopes, in respect to existence of isomeric states in even-even polonium isotopes, and possibilities of their production.

In the frame of the dissertation thesis the student will take a responsibility for one of the topics in ongoing research projects. The project includes participation and work at experimental measurements, data analysis and physical interpretation of results. Student is supposed to attend a series of stays abroad, therefore flexibility and ability to work independently are desirable.

Annotation: Experimental studies of atomic nuclei near the closed shells Z = 50 and 82 and new data demonstrate the necessity to improve our understanding of the nuclear structure. The difficulties to describe the nuclei are especially critical for nuclei far from the stability line, so called exotic nuclei. These nuclei provide unique possibilities to study various phenomena of nuclear physics, such as coexistence of states with different deformations, significant changes of nuclear shapes near the closed shells, beta delayed fission or isomeric states in nuclei.

Important information for the studies of exotic nuclei is the ability to describe their structure and estimate their production rates. The important source of new data is the study of long-lived isomeric states in atomic nuclei. One of the longest isomeric chains exists in even-even polonium nuclei in the region of neutron deficient nuclei at the region of closed shell with 82 protons. Dissertation thesis will be focused on the production and spectroscopy study of neutron-deficient polonium isotopes. The main goal of the thesis will be the topic of nuclear isomerism, which provides a possibility for detailed study low-lying excited states in atomic nuclei.

Comment: Collaboration: GSI Darmstadt (Germany), CERN (Switzerland), University of Paisley (UK), KU Leuven (Belgium)

Keywords: nuclear structure, decay spectroscopy, gamma spectroscopy, nuclear reactions

Tutor: doc. Mgr. Stanislav Antalic, PhD.
Department: FMFI.KJFB - Department of Nuclear Physics and Biophysics
Head of department: prof. RNDr. Stanislav Tokár, DrSc.

Assigned: 01.09.2012

Approved: 28.02.2012 prof. RNDr. Jozef Masarik, DrSc.
Guarantor of Study Programme

Student

Tutor

Univerzita Komenského v Bratislave
Fakulta matematiky, fyziky a informatiky

ZADANIE ZÁVEREČNEJ PRÁCE

Meno a priezvisko študenta: Mgr. Boris Andel
Študijný program: jadrová a subjadrová fyzika (Jednoodborové štúdium, doktorandské III. st., denná forma)
Študijný odbor: jadrová a subjadrová fyzika
Typ záverečnej práce: dizertačná
Jazyk záverečnej práce: anglický
Sekundárny jazyk: slovenský

Názov: Study of neutron-deficient polonium isotopes
Štúdium neutrónovo-deficitných izotopov polónia

Literatúra: P.E. Hodgeson, E. Gadioli and E. Gadioli Erba, Introductory Nuclear Physics, Oxford University Press, 1997.
K. Heyde, Basic Ideas and Concepts in Nuclear Physics, Institute of Physics Publishing, 3rd edition 2004.
R. Casten, Nuclear Structure from a Simple Perspective, Oxford University Press, 1990.
K. S. Krane, Introductory Nuclear Physics, John Wiley & Sons, 1988.
Články publikované v karentovaných časopisoch.

Cieľ: Predkladaný PhD projekt je zameraný na spracovanie a analýzu experimentálnych dát a ich následnú fyzikálnu interpretáciu. Merania budú realizované na separátore SHIP v GSI Darmstadt (Nemecko) a na experimentálnom zariadení ISOLDE v CERNe (Švajčiarsko). V súčasnosti máme na oboch experimentoch schválené návrhy na realizáciu meraní, resp. dostupné dáta. Primárnym cieľom dizertačnej práce je analýza a interpretácia spektroskopických dát pre neutrónovo deficitné izotopy polónia s ohľadom na existenciu izomérnych stavov v párno-párnych izotopoch polónia a možnosti ich produkcie.

Vrámci dizertačnej práce preberie študent zodpovednosť za niektorú z tém v rámci riešených projektov, pričom úlohou je spolupráca na realizácii meraní, analýza nameraných experimentálnych dát a fyzikálna interpretácia výsledkov. Počas štúdia by mal študent absolvovať sériu pobytov na zahraničných pracoviskách, preto je žiadúca flexibilita, znalosť angličtiny a schopnosť samostatne pracovať. Téma je zabezpečená grantovými prostriedkami a dlhodobou úspešnou medzinárodnou spoluprácou.

Anotácia: Výsledky dosiahnuté pri experimentálnom štúdiu jadier v okolí uzavretých vrstiev Z = 50 a 82 poukazujú na fakt, že ich štruktúra stále nie je dostatočne dobre pochopená. Obzvlášť to platí v prípade jadier ďaleko od oblasti stability. Táto oblasť poskytuje jedinečnú možnosť študovať viaceré fenomény jadrovej fyziky, ako je napr. koexistencia stavov s rôznou deformáciou, výrazné zmeny v deformácii jadier pozorované pre jadrá v blízkosti uzavretých vrstiev, zriedkavý rozpad jadier – oneskorené štiepenie po beta premene, či existenciu izomérnych stavov jadier.

Kľúčovou informáciou pre štúdium exotických jadier je možnosť opisu ich štruktúry a odhadu ich produkcie. Dizertačná práca sa zameria na problematiku produkcie a rozpadu neutrónovo-deficitných izotopov z okolia uzavretej protónovej vrstvy olova (Z = 82), ktoré prinesú nové informácie k uvedeným fyzikálnym problémom. Práca sa pritom zameria na tému jadrovej izomérie, ktorá poskytuje možnosť detailného štúdia nízko-ležiacich vzbudených hladín atómových jadier.

Poznámka: Spolupracujúce pracoviská:
GSI Darmstadt (Nemecko), CERN (Švajčiarsko), Univerzita v Paisley (V. Británia), KU Leuven (Belgicko)

Kľúčové slová: jadrová štruktúra, rozpadová spektroskopia, gama spektroskopia, jadrové reakcie

Školiteľ: doc. Mgr. Stanislav Antalic, PhD.
Katedra: FMFI.KJFB - Katedra jadrovej fyziky a biofyziky
Vedúci katedry: prof. RNDr. Stanislav Tokár, DrSc.

Dátum zadania: 01.09.2012

Dátum schválenia: 28.02.2012 prof. RNDr. Jozef Masarik, DrSc.
garant študijného programu

....
študent školiteľ

Abstrakt

Témou práce je štúdium neutrónovo deficitných izotopov polónia a astátu s hlavným zameraním na γ spektroskopiu izomérnych stavov v ^{192,194}Po. Skúmané izotopy boli produkované vo fúzno-výparných reakciách ^{56}Fe + ^{141}Pr a ^{51}V + ^{144}Sm v GSI v Darmstadte (Nemecko). Produkty reakcií boli odseparované od primárneho zväzku rýchlostným filtrom SHIP a študované pomocou detektorov umiestnených za separátorom. Izoméru v ^{194}Po boli priradené štyri nové γ prechody a po prvý krát boli pre tento izomér analyzované γ-γ koincidencie. Prechod, ktorý bol predtým navrhnutý ako prechod de-excitujúci izomérnu hladinu, bol nahradený novým prechodom s energiou 248 keV. Priradenie spinu izoméru bolo zmenené z (11^-) na (10^-), čo spôsobilo nečakanú zmenu v sérii izomérov v izotopoch Po. Bola určená presnejšia doba polpremeny izoméru s hodnotou 12.9(5) μs. V prípade izoméru v ^{192}Po bol podporený predpokladaný spin a parita (11^-) a bolo mu priradených 14 nových γ prechodov. Aj pre tento izomér boli po prvý krát študované γ-γ koincidencie. Ku prechodu s energiou 154 keV, ktorý de-excituje izomérnu hladinu, bol navrhnutý paralelný ($E3$) prechod s energiou 733 keV. Navyše bolo navrhnuté bočné napájanie pásu základného stavu kaskádou dvoch prechodov. Práca diskutuje systematiku 11^- izomérov a sily $E3$ prechodov v izotopoch Po a Pb z hľadiska nových spektroskopických výsledkov. Skúmaná bola aj jemná štruktúra α premeny ^{192}Po a ^{194}Po. Známe jemné α prechody vedúce na vzbudené 0^+ hladiny boli identifikované pre oba izotopy a boli vyhodnotené horné limity intenzít pre prípadné ďalšie, zatiaľ nepozorované α prechody. Bol pozorovaný náznak nového α prechodu v ^{192}Po. Pre izotopy $^{193-195}$Po a ^{194,195}At, produkované v reakcii ^{56}Fe + ^{141}Pr, boli vyhodnotené excitačné funkcie. Výsledky boli porovnané s výpočtami uskutočnenými pomocou kódu HIVAP, ktorý je založený na štatistickom modeli.

Kľúčové slová: izomér, γ spektroskopia, excitačná funkcia

Abstract

The topic of this Thesis is the study of neutron-deficient polonium and astatine isotopes with main focus on γ-ray spectroscopy of isomeric states in ^{192,194}Po. Investigated isotopes were produced in fusion-evaporation reactions ^{56}Fe + ^{141}Pr and ^{51}V + ^{144}Sm at GSI in Darmstadt (Germany). Reaction products were separated from the primary beam by the velocity filter SHIP and studied using detectors placed at the focal plane of the separator. Four new γ transitions were attributed to the isomer in ^{194}Po and γ-γ coincidences were investigated for the first time for this isomer. The transition, which was in previous experiment suggested to de-excite the isomeric level, was replaced by the new 248 keV transition. Moreover, the spin of the isomer was reassigned from (11^-) to (10^-), which caused an unexpected change in the chain of isomers in Po isotopes. More precise half-life of 12.9(5) μs was determined. Spin and parity (11^-) of the isomer in ^{192}Po was supported and 14 new γ transitions were attributed to the isomer. Also for this isomer, γ-γ coincidences were studied for the first time. De-excitation of the isomeric level by the 733 keV ($E3$) transition parallel to the 154 keV transition was proposed. Moreover, side-feeding of the ground-state band by the cascade of two transitions was suggested. The Thesis discusses systematics of 11^- isomers and $E3$ transition strengths in neutron-deficient Po and Pb isotopes in respect to new decay-spectroscopy results. In addition, fine structure in the α decay of both ^{192}Po and ^{194}Po was investigated. Previously known fine α-decay lines decaying to excited 0^+ states were identified and upper limits of intensity for additional fine α transitions were evaluated. Hint of a new fine α transition in ^{192}Po was observed. Excitation functions of isotopes $^{193-195}$Po and ^{194,195}At produced in reaction ^{56}Fe + ^{141}Pr were evaluated. Results were compared with calculations performed using statistical model code HIVAP.

Keywords: isomer, γ spectroscopy, excitation function

Preface and Acknowledgement

In spite of the continuous extensive research in nuclear physics, many open questions remain. Study of nuclei far from the stability line, so called exotic nuclei, is an excellent source of new information. Very sensitive tool for the investigation of these nuclei is the decay spectroscopy. Isotopes of interest are produced at accelerator facilities, separated from unwanted nuclei by electromagnetic separation and delivered to a detection systems optimized for registration of their radioactive decays. Careful analysis of obtained decay-spectroscopic data gives us invaluable insight into nuclear structure and properties of studied atomic nuclei.

Presented Dissertation Thesis is aimed at decay-spectroscopic studies of neutron-deficient polonium isotopes. The Thesis starts with definition of its objectives in Chapter 1 and continues with physical background related to the subject of study and description of experiment and detection system in Chapters 2 - 3. Calibrations of detectors are explained in Chapter 4. Main objective of the Thesis was the decay spectroscopy of ^{194}Po and ^{192}Po, especially the γ-ray spectroscopy of short-lived isomeric states present in these isotopes. New results are discussed in connection to series of isomers in even-even isotopes of Po and Pb. Decay-spectroscopy results include study of the fine structure in the α decay of both investigated isotopes. Second objective was evaluation of production cross-sections and comparison of experimental values with HIVAP calculations. All results are presented in dedicated sections of Chapter 5. At the end of the Thesis, Appendix A is attached, which discusses the analysis code for the new detection system at experiment SHIP.

Here, I would like to thank my supervisor Dr. Stanislav Antalic for guidance, valuable advices, discussions and all the help during my study. I am grateful for the opportunity to work on this project and to participate in research at unique experimental facilities.

I would also like to thank prof. Andrei N. Andreyev and Dr. Fritz P. Heßberger for productive discussions concerning data analysis and interpretation and for cooperation during experiments.

I am grateful to Dr. Zdenka Kalaninová for help with learning to work with the SHIP analysis code at the beginning of my PhD study and for many useful discussions.

Moreover, I would like to thank my friends and all the people that helped or supported me, either during experiments and stays abroad or at the faculty.

Finally, I am grateful to my mum and brother for continuous support and help.

Contents

List of Figures

List of Tables

List of Abbreviations

ADC	analogue to digital converter
ANL	Argonne National Laboratory
ATLAS	Argonne tandem linac accelerator system
CE	conversion electron
CERN	European Organization for Nuclear Research
CN	compound nucleus
DAQ	data acquisition
DSSD	double sided silicon (strip) detector
EC	electron capture
ER	evaporation residue
FEBEX	front end board with optical link extension
FMA	Fragment mass analyzer
FWHM	full width at half maximum
FPGA	field-programmable gate array
GANIL	Grand accélérateur national d'ion lourds
GSI	Gesellschaft für Schwerionenforschung
GUI	graphical user interface
ISOL	isotope separation on-line
ISOLDE	Isotope separator on-line device
JYFL	Department of Physics, University of Jyväskylä
LISOL	Leuven separator on-line
MBS	Multi branch system
MCP	microchannel plate
MoDSS	Mobile decay spectroscopy set-up
PSSD	position sensitive silicon (strip) detector
RITU	Recoil ion transport unit
SHIP	Separator for heavy ion reaction products
TAC	time to amplitude converter
TOF	time of flight
UNILAC	Universal linear accelerator

Introduction

Over the last decades, production of exotic nuclei, i.e. nuclei not occurring naturally on Earth, became almost a routine. Our knowledge about fundamental nuclear properties and number of artificially produced isotopes are growing expeditiously. However, as the boundaries of table of known isotopes are pushed asides, creation of new isotopes and elements becomes more and more challenging. Production yields and life times are decreasing rapidly and improvements of experimental techniques, detection set ups and development of new technologies are necessary.

To produce exotic nuclei, two approaches are widely used. Firstly, a bombardment of a thick target by highly energetic particles, resulting in fragmentation, spallation or fission of target nuclei, which is followed by electromagnetic separation. This technique is called ISOL (Isotope Separation On-Line) and is successfully used for example at ISOLDE at CERN (Switzerland), where the beam of ≈ 1 GeV protons is employed [Kug00]. Second approach employs fusion evaporation or transfer reactions, where thin target is bombarded by low-energy projectiles. Reaction products leave the target due to the reaction kinematics and are separated from projectiles in gas-filled or vacuum-mode separators. Advantage of the second approach is a possibility to study shorter-lived isotopes. More importantly, it is the only accessible way of production of heaviest elements.

Example of an outstanding vacuum-mode separator is a velocity filter SHIP (Separator for Heavy Ion reaction Products) at GSI. Although it was built more than 30 years ago [Mun79] and was significantly upgraded already in the early '90s [Hof00], it is still one of the best facilities for investigation of exotic nuclei in the world. Its major advantage is location at the beam line of the accelerator UNILAC, which provides beams of heavy ions with high intensity. In years 1981 - 1996, six new elements (107-112) were discovered at SHIP [Hof00]. Furthermore, many isotopes of heavy and superheavy elements were synthesized and identified here for the first time. These and even many other isotopes were involved in extensive nuclear structure studies carried out at SHIP since it became operational until nowadays.

In recent years, research in the area of the superheavy elements was ongoing (e.g. studies of the element 112 [Hof07] and 116 [Hof12]) and properties of the heaviest nuclei were investigated, as for example single-particle level systematics in $N = 153, 151$ isotones [Ant15] and einsteinium isotopes [Hes05], or identification and studies of K-isomers [Ant11; Sul07].

Moreover, extensive research was aimed on the region around proton closed shell $Z = 82$, where many interesting phenomena can be studied. For example, β-delayed fission (several cases studied [And13a]), fine structure in α decay (e.g. [And09; And06; Kal13]) and behaviour of α-decay properties near shell closure $Z = 82$ [And13b] or shape coexistence. Triple shape coexistence was observed for the first time in this region (^{186}Pb) [And00].

In this region near $Z = 82$, one of the longest series of isomers is known. Isomeric states with spin and parity 11^- are present in all even-A polonium isotopes with $196 \leq A \leq 210$ and their typical half-lives are between 0.5 ns and 1 μs. Most of these isomers de-excite via $E3$ transitions to 8^+ states [Alb91; Maj90; Fan90; Bax90; Pol97; Man88] with unexpected increase of transition strengths towards lower neutron numbers. The increase was discussed in connection to deformation of nuclei in [Dra01]. Short-lived isomeric states were identified also in isotopes ^{192,194}Po [Hel99; Vel03]. However, their spins, parities and decay paths were uncertain.

Presented Dissertation Thesis is based on analysis of data on ^{192,194}Po collected at the SHIP. At the beginning, objectives of the thesis are defined in Chapter 1 and are followed by physical background mainly in radioactive decay and fusion reactions (Chapter 2). Afterwards, the velocity filter SHIP is described in Chapter 3 alongside with its detection system. Experimental results start with Chapter 4 dedicated to calibrations of the detectors. Main part of the Thesis with physical results is aimed at γ spectroscopy of short-lived isomeric states in ^{192,194}Po and following discussion on systematics of (11^-) isomers in neutron-deficient Po and Pb isotopes (Chapter 5, Sections 5.1 - 5.3). Main results and discussions from these sections are going to be published in Physical Review C [And16].

Remaining results include study of the fine structure in the α decay of ^{192,194}Po (Section 5.4) and evaluation of production cross-sections of $^{193-195}$Po and ^{194,195}At (Section 5.5), which were synthesized in reaction $^{56}Fe + {}^{141}Pr \longrightarrow {}^{197}At^*$. Cross-sections are compared with results of calculations in statistical model HIVAP. Partial preliminary results on cross-sections and γ spectroscopy were published in AIP Conference Proceedings [And15]. The Thesis is complemented by Appendix A dedicated to new detection system at SHIP, mainly the analysis code for this new system.

Chapter 1

Objectives of the Dissertation Thesis

1.1 Decay Spectroscopy of ^{192}Po and ^{194}Po

The first objective of the Thesis is γ-ray spectroscopy of isomeric states in ^{194}Po and ^{192}Po, on which only limited information was available so far. Isomeric states with $I^{\pi} = 11^{-}$ are present in all heavier, even-A isotopes of Po up to ^{210}Po. The dominant configuration of the 11^{-} levels is $\pi h_{9/2} i_{13/2}$ [Hel99] and they are decaying mostly via $E3$ transitions to 8^{+} states. These decays exhibit unexpected enhancement of $B(E3)$ values with decreasing neutron number [Maj90; Alb91]. Isomers in ^{194}Po and ^{192}Po are expected to have a similar character as the isomers in heavier Po isotopes based on the systematics [Hel99; Vel03]. However, their spin and parity assignments and decay schemes were uncertain. In respect to unexpected increase of $B(E3)$ values, it is of interest to determine whether the chain of the 11^{-} isomeric states continues down to ^{194}Po and ^{192}Po and what would be the behaviour of $E3$ transition strengths. Additional goal is to investigate and confirm fine-structure α decays in discussed nuclei.

1.2 Cross Sections for the Production of At and Po Isotopes

The second objective of the Thesis is to evaluate experimental reaction cross sections for isotopes produced in reactions $^{56}Fe + ^{141}Pr \longrightarrow ^{197}At^{*}$ via pn and pxn channels. The goal is to obtain excitation functions of the reactions, i.e. dependence of the reaction cross section on the excitation energy of the compound nucleus. The next step is to compare the experimental data with results of calculation using statistical model code HIVAP. This will help to improve accuracy of cross-sections calculations in this area of isotopes, which is important for planning of future experimental measurements. Cross sections are extremely sensitive to excitation energy. A change in excitation energy of few MeV can result in change of the cross section greater than one order of magnitude, as for example for production reactions of neutron deficient bismuth and polonium isotopes [And05].

Chapter 2

Physical Background

2.1 Nuclear Shell Model

Dependence of various nuclear properties on proton (Z) or neutron (N) numbers, as for example two-proton or two-neutron separation energies, neutron capture cross-sections or energies of emitted α particles, exhibit sudden sharp changes in the vicinity of specific numbers of N or Z. These originally observed so-called "magic numbers" are 2, 8, 20, 28, 50, 82 and for neutrons also 126. Moreover, elements with "magic" proton number have higher relative abundances and higher number of stable isotopes, "magic" nuclei have high-lying first excited states. Similar behaviour was observed for atomic properties, which depend on number of electrons, and was explained by atomic shell model. Electrons obeying Pauli principle are filling shells with increasing energy. Filled (closed) shells act like an inert core and atomic properties depend mainly on the remaining valence electrons. Therefore, there was a motivation to develop to some extend analogical model also for nuclei. However, there are striking differences between the conditions for atomic electrons and nucleons in nuclei. Electron orbitals are defined mainly by the potential supplied by the nucleus (external agent) and electrons can move in their spatial orbits relatively without collisions with other electrons. Nucleons, on the other hand, are in the potential created by themselves and they are relatively large compared to size of the nucleus. Moving nucleon should then have high probability of collision with another nucleon.

These difficulties were overcome by fundamental assumption of nuclear shell model, which says that a spherically symmetric nuclear potential for a single nucleon is created by the other nucleons. Then, individual nucleons can be treated in this manner in turn and placed into energy levels in this potential. Moreover, they obey Pauli principle. In case of collision of the two nucleons, they would transfer energy and move to other energy levels. However, all energy levels up to valence level are already filled and cannot accept additional nucleon. For most nucleons it is unlikely to transfer correct amount of energy via collision to move them to unoccupied levels, which means that collisions cannot occur between them.

Levels are labelled using nl notation as in atomic physics ($1s, 2s, 1p$ etc.) with the exception, that n stands just for the order of level with a specific value of l and not for the principal quantum number. Parity of nucleon in the level with given l is $(-1)^l$ [Kra88; Cas05].

As a realistic approximation of shell model potential, a Wood-Saxon's potential is used:

$$V(r) = \frac{-V_0}{1 + exp[(r - R)/a]}, \tag{2.1}$$

where V_0 is the depth of potential well and it is of the order of 50 MeV, R is the nuclear radius and $a = 0.524\,\mathrm{fm}$ [Kra88]. Energy levels calculated for this potential can reproduce "magic numbers" only up to 20, which is the same as for unrealistic infinite well of harmonic oscillator potentials. To properly reproduce numbers of nucleons in closed shells, Wood-Saxon's potential has to be modified by spin-orbit term $V_{so}(r) l \cdot s$, where $l \cdot s$ is a key factor. A nucleon has a spin $s = 1/2$ and for a given angular momentum l it can have total angular momentum $j = l + 1/2$ or $j = l - 1/2$. There is exception for $l = 0$, where only $j = 1/2$ is possible. From equation $j^2 = (l + s)^2$ we can express the term $l \cdot s = 1/2(j^2 - l^2 - s^2)$ and for the expectation value we then get:

$$\langle l \cdot s \rangle = \frac{1}{2}[j(j + 1) - l(l + 1) - s(s + 1)]\hbar^2. \tag{2.2}$$

A level with a given value of $l > 0$ is then split into two new levels, e.g. f level ($l = 3$) is split into $f_{7/2}$ and $f_{5/2}$. Degeneracy of the new levels is $(2j + 1)$, which arises from possible m_j values. Energy difference of the new levels is proportional to:

$$\langle l \cdot s \rangle_{j=l+1/2} - \langle l \cdot s \rangle_{j=l-1/2} = \frac{1}{2}(2l + 1)\hbar^2. \tag{2.3}$$

A proper reordering or energy levels is obtained by choosing negative value of $V_{so}(r)$. With this form of nuclear potential, all "magic numbers" were reproduced and a new one at 184 was predicted [Kra88; May79].

The shell model explains ground-state spins (now standing for the total angular momentum denoted as J or I) and parities of spherical nuclei. A spin and parity of a filled (closed) j-shell is 0^+, thus nuclei with all j-shells filled have ground-states with $I^\pi = 0^+$. A spin and parity of an odd-A nucleus with one nucleon outside of the filled shell or one vacancy (hole) in the shell is defined by the spin and parity of this nucleon/hole. Moreover, it was found out, that nucleons occupying partly filled shells couple to pairs with $j = 0$. As a result, ground-states of even-even nuclei (even numbers of protons and neutrons) have $I^\pi = 0^+$ and spins and parities of odd-A nuclei are defined by the odd (unpaired) nucleon. Additionally, many excited states of odd-A nuclei can be explained by moving the odd nucleon to a higher shell, or by filling a vacancy in valence shell by moving a nucleon from a lower-lying shell. In the latter case, I^π of the excited state is defined by a newly-formed vacancy in the lower-lying shell [Cas05]. The shell model also explains for example spin isomers in odd-A nuclei [May79], which is discussed in subsection 2.6.1.

If an excited state of even-even nucleus is created by breaking a pair of nucleons, spin and parity is determined by coupling of j_1 and j_2 values of these two nucleons. Resulting angular momentum can have values between $j_1 + j_2$ and $|j_1 - j_2|$ [Kra88].

2.2 Collective Motion

The shell model works within a framework of inert filled shells and a few valence nucleons defining properties of entire nucleus. Although it can explain many properties of spherical nuclei, it cannot effectively account for collective motions of many nucleons, such as vibrations of even-even nuclei around a spherical equilibrium shape or rotations of nuclei with permanent deformation.

2.2.1 Nuclear Vibrations

When a nucleus is vibrating around spherical equilibrium, we can express coordinate of a point on the surface in the spherical harmonics:

$$R(t) = R_{av} + \sum_{\lambda \geq 1} \sum_{\mu=-\lambda}^{+\lambda} \alpha_{\lambda\mu}(t) Y_{\lambda\mu}(\theta, \phi), \tag{2.4}$$

where $Y_{\lambda\mu}(\theta, \phi)$ are spherical harmonics, $\alpha_{\lambda\mu}$ are amplitudes of harmonic components and R_{av} is average radius of the nucleus. Parity is determined similarly as for states with a given l, that is (-1)$^{\lambda}$. A constant term with $\lambda = 0$ is just R_{av} and a dipole term with $\lambda = 1$ is movement of the center of mass, which cannot be done by internal nuclear forces. Therefore the first excited state caused by vibrations has $\lambda = 2$ (quadrupole vibration) and $I^{\pi} = 2^{+}$. It is the first excited state of spherical even-even nuclei. Octupole vibration ($\lambda = 3$) causes in turn 3^{-} excited states. A term for a quantum unit of vibrational energy is phonon, analogically to photon in electromagnetism. By adding another quadrupole phonon to 2^{+} vibrational state, we will get a triplet of $0^{+}, 2^{+}, 4^{+}$ excited states. Vibrational features are typical for nuclei with $A < 150$ [Kra88].

2.2.2 Nuclear Rotations

Nuclear rotations are possible for nuclei with deformed equilibrium states. Such nuclei occur in the regions of $150 < A < 190$ and $A > 220$. The deformed shape of the nucleus can be described as an ellipsoid of revolution independent of ϕ:

$$R(\theta, \phi) = R_{av}[1 + \beta Y_{20}(\theta, \phi)], \tag{2.5}$$

where R_{av} is customarily approximated to a radius of a spherical nucleus with the same A and β is the deformation parameter defined as follows:

$$\beta = \frac{4}{3}\sqrt{\frac{\pi}{5}}\frac{\Delta R}{R_{av}}. \tag{2.6}$$

The ΔR is the difference between semimajor and semiminor axes of the ellipse. The deformed nucleus of this kind can have a prolate shape ($\beta > 0$), similar to rugby ball, or an oblate shape ($\beta < 0$), similar to disc. The nucleus rotates around axis perpendicular to symmetry axis, no rotations around symmetry axis can be observed.

An object with moment of inertia $\mathcal{J}$ rotating with angular frequency ω has the kinetic energy equal to $\frac{1}{2}\mathcal{J}\omega^2$. Since the angular momentum of the object is $l = \mathcal{J}\omega$, we can write for the energy an expression $\frac{l^2}{2\mathcal{J}}$. Then, transition to quantum mechanics and using nuclear angular momentum I results in:

$$E = \frac{\hbar^2}{2\mathcal{J}} I(I+1). \tag{2.7}$$

Rotational energy is increasing with increasing I, which forms a sequence of excited states called rotational band. For example, rotational band of the nucleus with 0^+ ground state is a sequence of $2^+, 4^+, 6^+, 8^+ ...$ states [Kra88].

In case of higher values of I, centrifugal force stretches the nucleus and the moment of inertia is enlarged. To take this effect into account, Equation 2.7 can be modified as follows:

$$E = \frac{\hbar^2}{2\mathcal{J}}[I(I+1) - \alpha I^2(I+1)^2]. \tag{2.8}$$

The value of nuclear moment of inertia lies between the values for a rigid rotor and for a frictionless fluid. Specifically, values between 0.2 and 0.5 of the value for rigid rotor were determined in experimental measurements [Hod00].

2.3 Fusion Evaporation Reactions

Fusion evaporation reactions (or compound nucleus reactions), occurring when excitation energy is around $\lesssim$ 100 MeV, are two step processes [Gho50]. In the first step, a compound nucleus (CN) with a particular excitation energy is formed by merging projectile and target nucleus. The second step is disintegration of the CN by emission of particles and photons. Schematically, we can write the process with emission of one particle as follows:

$$A + a \longrightarrow C^* \longrightarrow B + b \tag{2.9}$$

Mean life of the CN is long compared to the time needed for the projectile to pass through the target nucleus ($\approx 10^{-21} - 10^{-22}$ s). This leads to basic assumption in theory of CN, that the second step of reaction is independent from the first step. The CN "forgets" how it was created and resulting products depends only on the excitation energy of the compound state.

Cross section of reaction 2.9 is therefore given by:

$$\sigma(a,b) = \sigma_a(\epsilon)\eta_b(E), \tag{2.10}$$

where $\sigma_a(\epsilon)$ is the cross section of CN formation from the incident particle a with kinetic energy ϵ and the target nucleus A. The probability, that the CN will transform into final state $B + b$ is $\eta_b(E)$, where E is the excitation energy of the compound system. If the same CN with the same excitation energy is created by different projectile-target combination, the probability of decaying into $B + b$ will be the same as in Equation 2.10.

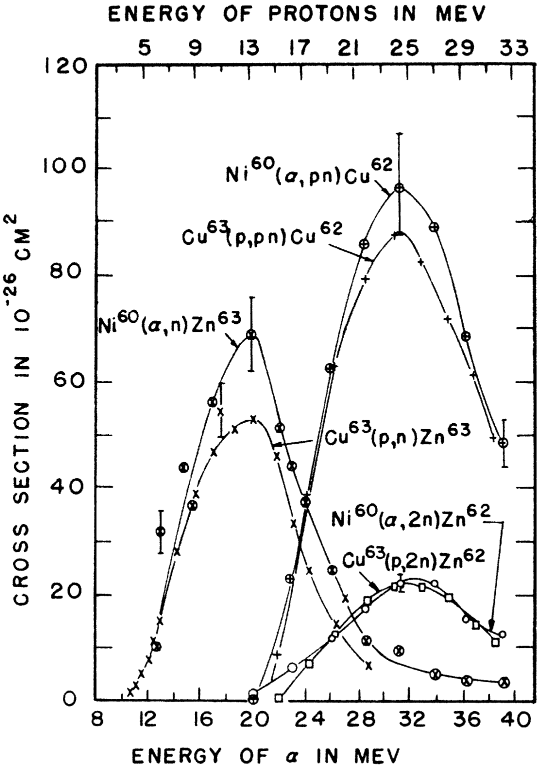

Figure 2.1: Experimental cross sections reprinted from [Gho50]. The proton energy scale is shifted by 7 MeV with respect to energy scale of α particles, so that the corresponding peaks are overlaying.

As a result, if we have another possible decay channel of C^* from 2.9, for example $D + d$, and another reaction channel $(A' + a')$ leading to C^* with the same excitation energy, we can get following relation using Equation 2.10:

$$\frac{\sigma(a,b)}{\sigma(a,d)} = \frac{\eta_b(E)}{\eta_d(E)} = \frac{\sigma(a',b)}{\sigma(a',d)} \tag{2.11}$$

Experimental verification of Equation 2.11 was done using reactions:

$$^{60}Ni(\alpha, n)^{63}Zn \qquad ^{60}Ni(\alpha, 2n)^{62}Zn \qquad ^{60}Ni(\alpha, pn)^{62}Cu \tag{2.12}$$

$$^{63}Cu(p, n)^{63}Zn \qquad ^{63}Cu(p, 2n)^{62}Zn \qquad ^{63}Cu(p, pn)^{62}Cu. \tag{2.13}$$

Resulting cross sections are shown in Fig. 2.1. Within experimental uncertainties, ratios $\sigma(\alpha, n) : \sigma(\alpha, 2n) : \sigma(\alpha, pn)$ for the target ^{60}Ni are in agreement with ratios $\sigma(p, n) : \sigma(p, 2n) : \sigma(p, pn)$ for the target ^{63}Cu [Gho50].

The theory of compound nucleus reactions is most accurate for low excitation energies (10 − 20 MeV) and medium-weight up to heavy target nuclei. For these conditions, the projectile has a small probability to escape from the nucleus with its identity and energy mostly intact, because of the relatively small energy available and large nuclear interior of the target.

In compound nucleus reactions, the original energy of projectile is shared amongst many nucleons in random collisions. Therefore, particles emitted in the decay channel of reaction have isotropic angular distribution. This is in contrast to direct reactions, where forward direction in respect of beam trajectory if preferred [Kra88].

We can calculate excitation energy of a CN using Q_0 value of the reaction and momentum conservation. Q_0 value of the compound nucleus reaction is given by:

$$Q_0 = (m_1 + m_2 - m_3)c^2 \tag{2.14}$$

where c is the speed of light and m_1, m_2 and m_3 are the ground-state masses of the projectile, the target and the compound nucleus, respectively. We use square of momentum in the form:

$$p^2 = m^2 v^2 = 2mE_k, \tag{2.15}$$

where m, v, E_k are the mass, the velocity and the kinetic energy of the body, respectively. Momentum conservation for the CN reaction can be expressed using Eq. (2.15) as:

$$m_1 E_{k1} = (m_1 + m_2)E_{k2}, \tag{2.16}$$

where E_{k1} is the kinetic energy of the projectile and E_{k2} is the kinetic energy of the CN. We made an approximation $m_3^* \approx m_1 + m_2$, where m_3^* is the mass of the CN in an excited state. Now we may express E_{k2} from Equation 2.16 and derive the change in internal energy caused by decrease of kinetic energy:

$$\Delta U = E_{k1} - E_{k2} = \frac{m_2}{m_1 + m_2} E_{k1}. \tag{2.17}$$

Since $\Delta U = E_{exc} - Q$, where E_{exc} is an excitation energy, we can determine the excitation energy of the CN as follows:

$$E_{exc} = \frac{m_2}{m_1 + m_2} E_{k1} + Q. \tag{2.18}$$

2.3.1 HIVAP

Important characteristic of a fusion evaporation reaction leading to a particular nucleus is its excitation function, i.e. the dependence of reaction cross section on excitation energy of a compound nucleus. Excitation function is very sensitive to the excitation energy. Change of excitation energy by few MeV may result in change of cross section by more than one order of magnitude, as for example in case of production of neutron deficient Bi and Po isotopes [And05].

While planning experiments, it is crucial to have reliable information about excitation functions, so it is possible to choose the right reaction and projectile energy. Cross sections of reactions, for which there is a lack of experimental data, can be calculated only approximately using models optimised by experimental data from similar reactions. One of the successful codes to calculate excitation functions is the statistical model code HIVAP [Rei92; Rei81].

Two different models of a fusion step of reaction are used in HIVAP. First model, so called inverted parabola, approximates Coulomb and nuclear part of the fusion barrier by a potential of an inverted harmonic oscillator. This approach gives mostly good results for projectile energies above the barrier, while for sub-barrier reactions the fusion probability is strongly underestimated. Second model, so called barrier fluctuations, was developed to effectively reproduce also sub-barrier fusion probability. It proved to be applicable in both sub-barrier and over barrier energy regions.

For the second step of the reaction, de-excitation of the compound nucleus, a standard evaporation theory is employed. Competition of γ emission, particle emission (neutron, proton, α) and fission is taken into account. Level density parameters are needed for γ- and particle-emission calculations, while the fission barrier is determined according to following formula [And05]:

$$B_f = C_f B_f + \Delta W^{exp}. \tag{2.19}$$

C_f is a free scaling parameter, B_f is a fission barrier calculated according to rotating liquid drop model [Coh74] and W^{exp} is a correction to the fission barrier. The correction is negative and often expressed as a ground state shell correction ΔW^{gs}, which in turn can be determined as a difference between empirical mass and theoretical mass from liquid drop model.

2.4 Transfer Reactions

Transfer reactions are a type of direct reactions involving transfer of one or a few nucleons between projectile and target. Direct reactions in general involve small number of valence nucleons of the target and proceed very fast. They take time in order of 10^{-22} s, which is much shorter compared to compound nucleus reactions with times of the order of 10^{-16} – 10^{-18} s. They become more important for higher projectile energies for which de Broglie wavelength is comparable to size of individual nucleons. However, both compound nucleus and direct reactions may be possible simultaneously. Even a specific reaction, as e.g. inelastic scattering, might occur either as direct process or as compound nucleus reaction [Kra88].

Typical example of transfer reaction is a stripping reaction, in which target nucleus catches a nucleon from projectile as in (d, p) reaction. Opposite process is a pickup reaction, e.g. (^{3}He, α), in which projectile takes a nucleon from target nucleus. Transfers of more than one nucleon are also possible, e.g. (d, α) [May79]. Reactions with transfer of single nucleon are used to investigate low-lying shell-model excited states [Kra88]. Other types of transfer reactions are knock out, e.g. (p, α), (p, p') and direct breakup reactions, e.g. (p, pp), (α, 2α) [Sch14].

Transfer reactions are competent processes in experiments aimed at production of very heavy nuclei via fusion reactions. Their products belong to most important sources of background [Hof00], but some of them may be useful for energy calibration as for example ^{211}Po and ^{212m}At produced during experiments with ^{209}Bi target [Ant08; Hes10].

2.5 Nuclear Decay

A nucleus in an energetically unstable state will decay until it reaches ground-state of the stable nucleus. For the given nuclide, one can define constant probability of decay per time unit - decay rate λ. When we have $N(t)$ nuclei of one nuclide at the time t, the decrease of this number in time will be:

$$-dN(t) = \lambda N(t)dt, \tag{2.20}$$

which, after integration, gives:

$$N(t) = N_0 e^{-\lambda(t-t_0)}. \tag{2.21}$$

N_0 is the number of decaying nuclei at the initial time t_0.

Mean-life of the radioactive species is defined as:

$$\tau = \frac{\int_0^\infty t\lambda N(t)dt}{N_0} = \frac{1}{\lambda} \tag{2.22}$$

and half-life $T_{1/2}$ is the time in which the number of decaying nuclei will decrease by one half. It is given by [Hod00]:

$$T_{1/2} = \frac{ln2}{\lambda} = \tau ln2. \tag{2.23}$$

2.5.1 Alpha Decay

Alpha decay is a process, when a helium nucleus (α particle) is emitted by an unstable nucleus. The process can be represented by a following formula:

$$ {}^{A}_{Z}X_N \;\rightarrow\; {}^{A-4}_{Z-2}X'_{N-2} + \alpha. \tag{2.24} $$

Assuming that the initial nucleus was at rest, the conservation of energy results in:

$$ m_X c^2 = m_{X'} c^2 + T_{X'} + m_\alpha c^2 + T_\alpha, \tag{2.25} $$

where m_X and $m_{X'}$ are masses of initial and final nucleus, m_α is a mass of α particle and $T_{X'}$ and T_α are kinetic energies of final nucleus and α particle, respectively.

By rearranging members of Equation 2.25, we will get the energy of reaction - Q value:

$$ Q = (m_X - m_{X'} - m_\alpha)c^2 = T_{X'} + T_\alpha. \tag{2.26} $$

Apparently, spontaneous α decay is possible only if $Q > 0$.

In our case of the initial nucleus at rest, the conservation of linear momentum requires that the final nucleus and α particle are moving in an opposite direction with equally large momenta:

$$ p_\alpha = p_{X'}. \tag{2.27} $$

Typical energies of α decays are about 6 MeV, therefore we can use nonrelativistic formula $T = \frac{p^2}{2m}$. Using kinetic terms of Equation 2.26 and Equation 2.27, we can derive the kinetic energy of an α particle from Q value:

$$ T_\alpha = \frac{Q}{\left(1 + \frac{m_\alpha}{m_{X'}}\right)}. \tag{2.28} $$

To make an approximation, we can replace m_α by 4 and $m_{X'}$ by $A - 4$, where A is the mass number of the initial nucleus. After small adjustments we can rewrite Equation 2.28 as follows:

$$ T_\alpha = Q\left(1 - \frac{4}{A}\right). \tag{2.29} $$

The kinetic energy of the α particle is typically around 98 % of Q value and the recoiling nucleus carries away remaining 2 % [Kra88].

Positive Q_α value by itself is not sufficient for α decay to occur, because α particle has to overcome a Coulomb barrier. Alpha particles from natural nuclides have energies much smaller than the Coulomb barrier (the barrier height is $\approx 30\,\text{MeV}$ in heavy nuclei), therefore they have to tunnel through the barrier and the decay is a quantum mechanical process. The wavefunction of the particle passing through the barrier is exponentially attenuated. For a reasonable probability of the process, α particle energy of at least few MeV is needed. The probability of α decay is extremely sensitive to the energy of the particle, which explains large range of half lives of α emitters [Hod00; Kra88].

From the barrier tunnelling point of view, we can write α decay rate λ as:

$$\lambda = \lambda_0 T, \tag{2.30}$$

where λ_0 consists of two factors. First one depends on the structure of the nucleus and states the probability of α particle formation inside the nucleus and the second one expresses the number of attempts of the particle to go through the barrier per second. The second factor can be roughly approximated as $\frac{v_0}{2R}$, where v_0 is the velocity of the particle and R is the nuclear radius.

The term T in Equation 2.30 is a barrier penetration factor, which is the probability, that the particle will successfully get through once it hits the barrier. It is defined as the ratio of the flux going through the barrier and the incident flux.

So far, we mentioned Coulomb barrier only, which is outside the nucleus defined as:

$$V(r) = \frac{1}{4\pi\epsilon_0}\frac{2Ze^2}{r}, \tag{2.31}$$

where Z is the proton number of the daughter nucleus and r is the distance between centres of the nucleus and the α particle. However, if the particle carries away orbital angular momentum $l_\alpha > 0$, the barrier also consists of an additional centrifugal term:

$$V_L(r) = \frac{l_\alpha(l_\alpha + 1)\hbar^2}{2\mu_\alpha r^2}, \tag{2.32}$$

where μ_α is a reduced mass of the α particle defined as:

$$\mu_\alpha = \frac{m_\alpha m_{X'}}{m_\alpha + m_{X'}}. \tag{2.33}$$

The centrifugal term causes a fast decrease of α particle emission probability with increasing l_α [Hod00].

If an initial nuclear state has an angular momentum I_i and a final state after α decay has an angular momentum I_f, an α particle can carry away angular momentum l_α with value from following range:

$$|I_i - I_f| \leq l_\alpha \leq I_i + I_f. \tag{2.34}$$

Since the spin of the α particle is 0, the angular momentum is purely orbital. The change of the parity caused by such transition is equal to $(-1)^{l_\alpha}$. Conservation of parity gives us therefore selection rules for α decays. If the initial and final states of the transition have the same parity, l_α has to be even, if the initial and final states have opposite parity, l_α has to be odd. For example, when one of the states has spin 0, Eq. (2.34) gives only one possible value of l_α, which is equal to I of the other state. Thus, if the state is 0^+, transitions to (or from) *even*$^+$ and *odd*$^-$ states are allowed and transitions to (or from) *even*$^-$ and *odd*$^+$ states are forbidden. However, when neither of the states has the angular momentum equal 0, there are no completely forbidden transitions. In this case, there are more possible l_α values. More importantly, l_α can be odd, if there is a change in parity or even, if the parity remains the same. For example, in transition $2^- \rightarrow 2^+$, the value of l_α must be between 0 and 4. Since the states have different parities, allowed orbital angular momenta of α particles are $l_\alpha = 1$ and $l_\alpha = 3$ [Kra88].

Fine Structure in Alpha Decay

Alpha decay of an initial nucleus may possibly lead to a number of different states in a final nucleus, not only to ground-state or one particular excited state. Naturally, α transitions to different states will have accordingly different Q values:

$$Q_i = Q_{g.s.\longrightarrow g.s.} - E_i^*, \tag{2.35}$$

where Q_i is the Q value of transition to ith excited state, $Q_{g.s.\longrightarrow g.s.}$ is the Q value of transition between ground states and E_i^* is the excitation energy of the ith state in daughter nucleus. An energy spectrum of emitted α particles will have in such case a number of distinctive peaks - fine structure.

A decay probability to a particular state in the daughter nucleus will mainly depend on decay hindrance by structure differences between initial and final state and by change of angular momentum [San12]. Fine structure in α decay is used as a sensitive tool to probe nuclear structure and especially shape coexistence (e.g. [And00; Dup00]).

2.5.2 Beta Decay

During β decay, neutron and proton numbers are changed by 1 unit ($Z' = \pm 1$, $N' = N \mp 1$), while mass number remains the same ($A' = A$). There are three types of the β decay:

1. β^- decay: a neutron in nucleus transforms to proton, electron and electron antineutrino and the latter two are emitted:

$$ {}^{A}_{Z}X_N \rightarrow {}^{A}_{Z+1}X'_{N-1} + e^- + \bar{\nu}_e. \tag{2.36}$$

When neglecting the difference in binding energies of electrons between initial and final atom, the energy of the decay can be calculated from atomic masses as follows:

$$Q_{\beta^-} = [m_X - m_{X'}]\, c^2. \tag{2.37}$$

The β^- decay is energetically possible and occurs not only in nuclei, but also on free neutrons with half-life about 10 minutes.

2. β^+ decay: a proton in the nucleus transforms to neutron, positron and electron neutrino, while the latter two are emitted:

$$ {}^{A}_{Z}X_N \;\rightarrow\; {}^{A}_{Z-1}X'_{N+1} + e^+ + \nu_e. \tag{2.38}$$

Energy of the decay is given by:

$$Q_{\beta^+} = \left[m_X - m_{X'} - 2m_e\right] c^2. \tag{2.39}$$

3. Electron Capture - EC or ε: atomic electron is captured by the nucleus, proton transforms into neutron and an electron neutrino is emitted:

$$ {}^{A}_{Z}X_N + e^- \;\rightarrow\; {}^{A}_{Z-1}X'_{N+1} + \nu. \tag{2.40}$$

Once again, Q value of the decay in terms of atomic masses is given by:

$$Q_{\beta^+} = \left[m_X - m_{X'}\right] c^2 - B_n. \tag{2.41}$$

The term B_n arises from the fact, that after capture of the electron from an atomic shell, the atom is left in an excited state with the binding energy of captured electron. Vacancy in the atomic shell is filled by an electron from higher shell and characteristic x ray or cascade of x rays is emitted.

Although both β^+ decay and EC transform the same parent nucleus to the same daughter nucleus, they are not always both possible for the same nucleus. The term $2m_e$ from Equation 2.39 is much higher than the term B_n from Equation 2.41, thus, when EC is already energetically possible, β^+ decay may still have $Q < 0$.

In all equations concerning Q values, transitions from ground-state to ground-state were considered. However, β decay can lead to an excited state and in such case the Q value has to be decreased:

$$Q_{ex} = Q - E_{ex}, \tag{2.42}$$

where E_{ex} is excitation energy of the state [Kra88].

Energy spectrum of β particles is continuous. Assuming that energy of the recoiling nucleus is negligible, the sum of kinetic energies of neutrino and β particle is constant and equal to the energy of β decay, which is also the maximum energy of β particles.

Shapes of β^- and β^+ spectra are different due to the effect of nuclear Coulomb field. Emitted electrons are attracted while positrons are repelled, what results in the slight shift of β^- spectrum mean energy towards lower energies and in case of β^+ the shift is towards higher energies.

Important tool in analysis of β spectra is the Fermi plot. It is a plot of the function:

$$\sqrt{\left(\frac{N(\eta)}{\eta^2 F(Z,\eta)}\right)} = const.(\varepsilon_0 - \varepsilon) \tag{2.43}$$

and it is used to determine maximum energy of the spectrum (ε_0). $F(Z,\eta)$ is a correction factor taking the effects of nuclear Coulomb field into account. η is the momentum of β particle and ε its energy defined as:

$$\eta = \frac{p}{m_0 c} \qquad \varepsilon = \frac{W}{m_0 c^2}, \tag{2.44}$$

where p is the momentum, W the total energy and m_0 the mass of the β particle [May79].

In the allowed approximation of the Fermi theory of the β decay, electron and neutrino cannot carry orbital angular momentum ($l = 0$). Both electron and neutrino have spins $s = \frac{1}{2}$, which can be antiparallel or parallel. Therefore, their total spin can be either $S = 0$ (Fermi decay) or $S = 1$ (Gamow-Teller decay). In case of Fermi decay there cannot be any change of nuclear spin. In case of Gamow-Teller decay the change can be $\Delta I = 0$ or 1 due to $S = 1$ (with the exception of transition $0 \rightarrow 0$, which is not possible by Gamow-Teller decay). The change of parity is equal to $(-1)^l$, which means no change in allowed decays. Thus the selection rules for the allowed β decays are as follows:

$$\Delta I = 0, 1 \qquad \pi_i = \pi_f, \tag{2.45}$$

where π_i and π_f are parities of initial and final state, respectively.

Although so called forbidden decays are usually less probable then allowed ones, there are cases in which only forbidden decays are possible. In these decays, also orbital angular momentum $l > 0$ is carried away from nucleus by β particle and neutrino. First forbidden decays occur, when $l = 1$ therefore the selection rules are given by:

$$\Delta I = 0, 1, 2 \qquad \pi_i \neq \pi_f. \tag{2.46}$$

Second forbidden decays happen when $l = 2$ is carried away. Following selection rules are applied:

$$\Delta I = 2, 3 \qquad \pi_i = \pi_f. \tag{2.47}$$

Similarly it continues for third and fourth forbidden decays. It has to be noted, that for second forbidden decays, also $\Delta I = 0, 1$ is possible. However, these cases fulfil selection rules for allowed decays, and thus contribution of forbidden decays is negligible [Kra88].

2.5.3 Gamma Decay

Nucleus in an excited state may release its energy via emission of a γ ray. Usually, an emission of a particle is preferred, but γ decay can successfully compete when particle emission is hindered (for example by Coulomb barrier, selection rules, etc.). Moreover, if emission of the particle is energetically impossible, the nucleus can de-excite only by electromagnetic processes, mostly by γ decay [May79].

In nuclear transition from initial state with energy E_i to final state with energy E_f, energy $\Delta E = E_i - E_f$ is released. From momentum and energy conservation we can calculate energy of emitted γ ray as:

$$E_\gamma \approx \Delta E - \frac{(\Delta E)^2}{2Mc^2}, \tag{2.48}$$

where M is the rest mass of recoiling nucleus and in last term we used approximation $E_\gamma^2 \approx (\Delta E)^2$ since $E_\gamma \ll Mc^2$. Regarding γ-ray spectra, the difference between E_γ and ΔE is usually negligible [Hod00].

The multipolarity of γ radiation is given by 2^l, where l is angular momentum carried by a γ ray. Radiation of lowest multipolarity is a dipole radiation ($l = 1$), since γ ray cannot have $l = 0$. There are two types of γ radiation - electric and magnetic. Electric multipoles are denoted as El and magnetic multipoles are denoted as Ml, for example $E2$ is electric quadrupole radiation, $M3$ is magnetic octupole radiation etc.

Conservation of angular momentum gives selection rules for electromagnetic transitions. In case of transition from initial state with angular momentum I_i into final state with angular momentum I_f, selection rules for γ-ray angular momentum l and its components in z direction m are:

$$|I_i - I_f| \leq l \leq I_i + If, \qquad m = m_i - m_f. \tag{2.49}$$

Decays with the lowest possible l have the highest probability, because transition probability depends on the term $(R/\lambda\!\!\!^{-})^{2l}$, where R is nuclear radius. Selection rules are thus in most cases reduced to $l = |I_i - I_f|$.

Parity has to be conserved in electromagnetic transitions as well. Parity of electric multipole radiation is $(-1)^l$, while magnetic multipole radiation has parity $(-1)^{l+1}$. This gives us following selection rules:

$$\pi_i = (-1)^l \pi_f \qquad \text{for electric multipole radiation,} \tag{2.50}$$

$$\pi_i = (-1)^{l+1} \pi_f \qquad \text{for magnetic multipole radiation,} \tag{2.51}$$

where π_i and π_f are parities of initial and final state of the nucleus, respectively.

Electric transitions are of several orders of magnitude stronger than magnetic transitions of the same multipolarity. However, due to selection rules, both radiation types of the same multipolarity l cannot be emitted together in transition between given states. Possible combination is for example $M1$ and $E2$ radiation. In this case, transition probabilities are of the same order of magnitude, despite the higher order of multipolarity of the electric transition [May79].

Internal Conversion

Nuclear multipole electromagnetic fields of an excited nucleus may interact with an electron from atomic shell and cause its emission. This phenomenon is called internal conversion and it is a competitive process to γ-ray emission. Internal conversion is especially important for $E0$ transitions, since they cannot proceed via emission of electromagnetic radiation. A vacancy is left in the atomic shell after the process and it is filled by an electron from higher shell. Internal conversion is therefore accompanied by emission of characteristic x rays.

Energy of a conversion electron is given by:

$$T_e = \Delta E - B, \tag{2.52}$$

where ΔE is the transition energy and B is the binding energy of the electron, taken as a positive value (energy needed to free the electron from the shell). Binding energies are different for different shells, thus a source with a single γ-ray energy will have several discrete energies of conversion electrons. These electrons are often denoted by the shell from which they were emitted as K, L, M and so forth. Moreover, electrons from one atomic shell have slightly different energies, according to atomic orbitals they originate from.

Since γ-ray emission and internal conversion are competitive processes, the total decay probability λ_t is the sum of γ-ray emission probability λ_γ and internal conversion probability λ_e. These partial probabilities are connected through internal conversion coefficient as:

$$\alpha = \frac{\lambda_e}{\lambda_\gamma}. \tag{2.53}$$

The total decay probability then can be given by:

$$\lambda_t = \lambda_\gamma(1 + \alpha). \tag{2.54}$$

Conversion coefficients increase with increasing Z and multipole order and decrease with increasing transition energy [Kra88].

Weisskopf Estimates

Half-life of the photon emission by single-particle nuclear transition can be estimated using equations derived by Weisskopf. If we have transition of multipolarity l and photon energy E_γ [keV] in a nucleus with A nucleons, estimates for half-life [s] of photon emission by electric (El) and magnetic (Ml) transitions are:

$$t_{1/2}(El) = \frac{ln2l[(2l+1)!!]^2\hbar}{2(l+1)e^2R^{2l}}\left(\frac{3+l}{3}\right)^2\left(\frac{\hbar c}{E_\gamma}\right)^{2l+1} \tag{2.55}$$

$$t_{1/2}(ML) = \frac{ln2l[(2l+1)!!]^2\hbar}{80(l+1)\mu_N^2R^{2l-2}}\left(\frac{3+l}{3}\right)^2\left(\frac{\hbar c}{E_\gamma}\right)^{2l+1}, \tag{2.56}$$

where $R = 1.2x10^{-13}A^{1/3}$ [cm]. Constants from the equations have following values: $\hbar = 6.58212\times10^{-19}$ keV s, $e^2 = 1.44\times10^{-10}$ keV cm, $b = 10^{-24}$ cm^2, $\hbar c = 197.327\times10^{-10}$ keV cm and $\mu_N^2 = 1.5922\times10^{-38}$ keV cm^3 [Fir96].

Weisskopf estimates of transition probabilities are often given in units $[e^2fm^{2l}]$ and corresponding formulae are [Suh07]:

$$B_W(El) = \frac{1.2^{2l}}{4\pi}\left(\frac{3}{l+3}\right)^2 A^{2l/3} \tag{2.57}$$

$$B_W(Ml) = \frac{10}{\pi}1.2^{2l-2}\left(\frac{3}{l+3}\right)^2 A^{(2l-2)/3}\left(\frac{\mu_N}{c}\right)^2 \tag{2.58}$$

These estimates show, that in general, lower multipole transitions are much more probable. Increase in multipolarity by 1 decreases probability approximately by a factor of 10^{-5}. Moreover, in medium and heavy nuclei for a given l, electric transitions are more probable than magnetic transitions by a factor of about 100 [Kra88].

In nuclear structure studies, it is useful to evaluate ratio of Weisskopf single-particle estimate and experimental half-life [Fir96]:

$$B(El;Ml) = \frac{t_{1/2}(El;Ml)_W}{t_{1/2}(El;Ml)_{Exp}}[W.u.], \tag{2.59}$$

where W.u. are so called Weisskopf units. However, we need to take into account that de-excitation of the level may be possible by different γ transitions and that internal conversion competes γ emission. Combining Equations 2.54, 2.59 and using partial half-life $t_{1/2}(i) = t_{1/2}(level)/I_i$, ratio $B(El;Ml)$ for the ith possible de-exciting transition can be written as follows [Fir96]:

$$B(El;Ml) = \frac{t_{1/2}(El;Ml)_W I_i}{t_{1/2}(level)_{Exp}(1+\alpha_i)}, \tag{2.60}$$

where I_i is the relative intensity of ith transition and α_i is its total conversion coefficient. If the ratio is many orders of magnitude lower than 1, the transition may be hindered by weak overlap of initial and final wave functions. On the other hand, if it is much higher than 1, we may expect that more than only one nucleon is involved in the transition [Kra88].

2.6 Isomeric States

Isomeric states are nuclear meta-stable excited states. Usually, a nuclear state is regarded as isomeric, when its half-life is long compared to most other excited states. This typically means that the half-life of the isomer should be longer than 1 ns [Wal99].

2.6.1 Spin isomers

Spin isomers occur, when the de-excitation to a lower energy state involves a large change in nuclear spin. A transition with high multipolarity is needed, thus electromagnetic transitions are hindered. Moreover, the fact, that the decay probability decreases with decreasing transition energy is important for low energy electromagnetic transitions. Spin isomers de-excite mostly by γ decay or internal conversion, but there are cases of the isomers decaying by α decay, β decay or proton emission [Wal99].

Typical examples of spin isomers are single-particle isomeric states in the vicinity of closed shells. They occur in odd-A nuclei, where first excited state is achieved by moving one nucleon to the orbital with a higher energy. For nuclei with N or Z from the range of $39-49$ it means moving a nucleon from $p_{1/2}$ orbital to $g_{9/2}$ orbital, that is a change of spin by 4. Similar situation arises when number N or Z is from range of $65-81$. The odd nucleon is moved between orbital with spin of 3/2 or 1/2 and orbital with spin of 11/2. The last "island of isomerism" is for specific nucleons from the range of $101-125$, where a nucleon moves between orbital with spin of 5/2, 3/2 or 1/2 and orbital with spin of 13/2 [May79]. However, it does not necessarily mean, that the isomer has higher spin than the ground state. In indium isotopes ($Z = 49$), isomers with $I = 1/2$ occur, while the ground states have $I = 9/2$. In the ground state, unpaired proton lies in the $1g_{9/2}$ orbital. The isomeric state is created by moving additional proton from $2p_{1/2}$ to $1g_{9/2}$ and leaving unpaired proton in $2p_{1/2}$ orbital, which gives $I = 1/2$ to the isomeric state. Opposite situation takes place in thallium isotopes ($Z = 81$), where ground states have $I = 1/2$. The isomeric state is created when odd proton from $3s_{1/2}$ is excited to $1h_{9/2}$, thus giving $I = 9/2$ to the isomer [Ben84].

An example of extremely long-lived spin isomer is ^{180m}Ta with half-life greater than 10^{15} years. It has the excitation energy only 75 keV and the difference in spin between the isomer and the ground state is $\Delta I = 8$ [Wal99].

Another extreme isomer is ^{212m}Fr with very high excitation energy of 8.5 MeV and suggested very high spin of $I = 34$ [Byr90].

2.6.2 *K* isomers

K isomers are a type of spin isomers. They are formed, when decay to a lower energy state requires a large change in *K* quantum number. *K* is a projection of total nuclear spin vector to a symmetry axis of the nucleus. *K* isomers occur only in axially symmetric nuclei with prolate deformation (shape similar to a rugby ball). Selection rule arises from the K quantum number, that multipolarity of radiation has to be greater than or at least equal to a change in K. However, also K forbidden transitions with lower multipolarities are possible. Although they are hindered, they may be more probable, than transitions fulfilling K-selection rule [Wal99].

A hindrance factor of a transition de-exciting a K isomer can be written as follows:

$$F_W = \frac{T_{1/2\gamma}(experiment)}{T_{1/2\gamma}(Weisskopf\ estimate)} \tag{2.61}$$

and the degree of forbiddenness is expressed as $\nu = \Delta K - \lambda$, where λ is multipolarity of the transition. It was found from systematics, that F_W decreases by a factor of ≈ 100 per degree of forbiddenness [Lob68]. This relation can be expressed through "reduced hindrance" f_ν as follows [Wal99]:

$$f_\nu = F_W^{1/\nu} \approx 100 \tag{2.62}$$

K isomers can be found for example in Hf and W isotopes. Notable example is the isomer with long half-life of 31 years and high $K = 16$ present in ^{178}Hf. In ^{178}W, there is an isomer with unusually high number of unpaired nucleons. It is formed by 4 unpaired protons and 4 unpaired neutrons. To produce K or spin isomers, fusion evaporation, partial fusion and fragmentation reactions can be used [Wal99].

K isomers have been found also in nuclei with $Z > 100$. Moreover, the heaviest nuclei are expected to be deformed. Multi quasiparticle states with low energy and high K were predicted in these nuclei, thus K isomers could be formed there. As high-spin isomerism increase stability in respect to fission and α decay, it is possible that high-K states with longer half-lives than ground states can be present. Therefore, superheavy nuclei with too short half-lives may be experimentally accessible through production of their K isomers [Xu04].

2.6.3 Shape isomers

Shape isomers appear, when a nucleus has a local minimum in the potential energy surface at large deformation. Typical examples of shape isomers are fission isomers. They have unusually short fission half-lives (from ~ ps up to ~ ms) compared to spontaneous fission from the ground state. Short half-lives were explained by double-humped fission barrier, where the isomers are located in the second energy minimum of the barrier (the first energy minimum is the ground state) and thus fission from the isomer has to overcome smaller fission barrier. De-excitation of the isomer to the ground state via γ emission is hindered, because it requires change in deformation and thus large collective rearrangement of the nucleus. Fission isomers are known in isotopes of actinides from uranium to berkelium [Hal92; Hal90].

2.6.4 Seniority isomers

Seniority ν is a quantum number stating a number of unpaired nucleons, which are not coupled to angular momentum $J = 0$. Conservation of seniority defines selection rules, which lead to formation of seniority isomers. For example, in even-even semi-magic nuclei, the ground states have $\nu \approx 0$ and low energy yrast states with $J = 2, 4, 6...$ have two unpaired nucleons and thus $\nu \approx 2$. Since $E2$ transitions between $\nu = 2$ states are hindered in semi-magic nuclei, seniority isomers may be formed there [Isa11].

Chapter 3

Experiment SHIP

SHIP (Separator for Heavy Ion Reaction Products) is a vacuum-mode recoil separator, located at GSI in Darmstadt, Germany. It was designed to investigate nuclei with intermediate and very heavy masses, mostly produced by fusion evaporation reactions and to effectively separate these nuclei from the primary beam [Mun79]. The separator became operational in 1976 [Her08] and it was modified in the early '90s in order to increase the capabilities of production and identification of elements beyond Meintnerium (Z = 109) [Hof00].

3.1 Production of Nuclei

To produce exotic nuclei, mostly fusion evaporation reactions are used at SHIP. Beam of accelerated ions is provided by the UNILAC (Universal Linear Accelerator, Fig. 3.1 left). It is able to accelerate heavy ions up to uranium and provide high intensities, e.g. up to 3.0 $p\mu$A for ^{40}Ar^{8+} or 1.2 $p\mu A$ for ^{58}Fe^{8+} (1 pμA = $6.24x10^{12}$ $particles$/s). The beam energy is adjustable and its relative accuracy is ± 0.003 MeV/u. The absolute accuracy is ± 0.01 MeV/u [Hof00].

The beam is pulsed, with 50 Hz frequency. Macropulse with duration 5.5 ms is followed by 14.5 ms period without the beam [Fol95]. The targets are thin foils mounted on a rotational wheel. Target thickness is between 0.1-1 mg/cm^2, which is determined by the maximum velocity width accepted by the separator.

Beam particles passing through the target are additionally ionized. However, some of them may fly through the pinholes in the target, which results in lower ionization and higher magnetic rigidity. Such particles may not be effectively separated and could cause increase of background. Therefore, a thin carbon foil was installed downstream behind the target wheel, which reduces this problem and equilibrates charge states of reaction products [Mun79].

There are 8 targets mounted on the wheel. Rotation of the wheel is synchronized with UNILAC macropulses in a way, that every third target is hit sequentially. This results in a 160 ms cooling period between hits of the same target. Speed of the rotation is 1125 rpm.

The wheels (Fig. 3.1 right) are manufactured from 1.9 mm thick aluminium disks of 99.5 % purity. The targets are usually backed by $40 \pm 4\,\mu$g/cm^2 carbon foils and covered by another $8 \pm 3\,\mu$g/cm^2 layer of carbon. The covering carbon layer protects more sensitive targets from oxidation when they are exposed to open air, reduces sputtering of the target material during the irradiation by the beam of heavy ions [Fol95] and increases emissivity [Ant04].

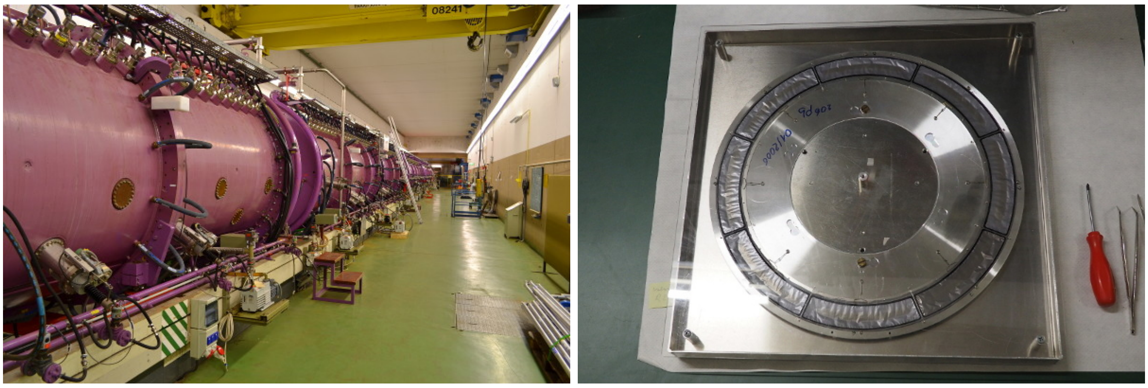

Figure 3.1: Left panel: Linear accelerator UNILAC. Right panel: target wheel used at SHIP with ^{206}Pb target foils.

3.1.1 Reaction Cross Section

At SHIP, the thin target is bombarded by a beam of projectiles. When N_p is the total number of incident projectiles, N_{ER} is the total number of evaporation residues (reaction products) and η is an area density of nuclei in the target [cm^{-2}], the reaction cross section [cm^2] is given as:

$$\sigma = \frac{N_{ER}}{N_p \eta}. \tag{3.1}$$

For η we can write:

$$\eta = f \frac{N}{S}, \tag{3.2}$$

where N is the total number of target nuclei, f is the isotopic purity of the target material normalised to 1 and S is the area of the target.

Using Avogadro constant N_A and molar mass M_m of the target the area density of nuclei is given by:

$$\eta = f N_A \frac{m}{S M_m}. \tag{3.3}$$

We determine the number of evaporation residues (ERs) by measuring decays of ERs, which reached detectors. Thus, if N_i is a number of decays of particular type (e.g. α, spontaneous fission), b_i is corresponding branching ratio, ε_i corresponding detection efficiency and ε is the transmission efficiency of the separator, we can calculate number of ERs as follows:

$$N_{ER} = \frac{N_i}{\varepsilon \varepsilon_i b_i}. \tag{3.4}$$

The number of projectiles is calculated using a SCC (Scale Coulomb Counter). It is a measure of total charge collected by a Faraday cup, which is stopping the beam. However, it is not directly a correct value of charge. When we denote the total collected charge Q, average beam current $\bar{I}$, beam current during pulse I, charge state of projectiles q and elementary charge e, the number of projectiles is:

$$N_p = \frac{Q}{qe} = \frac{\bar{I}t}{qe} = \frac{ItD}{qe}. \tag{3.5}$$

D is a duty factor, which was introduced, because the beam is pulsed. The factor is a ratio of pulse time and total time of one period (macropulse). Time t is the total time of charge collection.

Since the value of SCC (we can denote is as C) is not directly applicable as the total collected charge and beam current is not completely constant, we use information about relation between I and counting rate R of SCC (R is average rate during whole macropulse). That is, when we know that a particular value of I, which is mainly sent from the accelerator, corresponds to a particular value of R, then the time of charge collection normalized to constant value of beam current I will be given by:

$$t = \frac{C}{R} \tag{3.6}$$

and the total number of projectiles can be written as follows:

$$N_p = \frac{C}{R}\frac{ID}{qe}. \tag{3.7}$$

Finally, we can rewrite Equation 3.1 using Equations 3.3, 3.4, 3.7 and evaluate the reaction cross section as follows:

$$\sigma = \frac{N_i}{\varepsilon\varepsilon_i b_i}\frac{R}{C}\frac{qe}{ID}\frac{SM_m}{fmN_A}. \tag{3.8}$$

3.2 Velocity Filter SHIP

SHIP is a vacuum-mode recoil separator, more specifically, a velocity filter. It uses separated static electric and magnetic fields to charge independent separation of ions according to their velocity. Main goal is to suppress intensive primary beam as much as possible and let through fusion-evaporation reaction products [Mun79].

Basic principle of the velocity filters is to use crossed electric and magnetic fields to allow only ions with certain velocity to pass the filter. Electric force F_E and magnetic force F_B are acting on ions flying through the filter:

$$F_E = qE \qquad F_B = qvB. \tag{3.9}$$

The two forces will be in balance only for ions with the right velocity and these ions will not be deflected:

$$qE = qvB \Rightarrow v = \frac{E}{B}. \tag{3.10}$$

In practice, the velocity filters are not completely charge independent and they accept only particular charge range, which causes decrease of transmission [Her08].

Between the separator and the target system (Fig. 3.2), there is a triplet of quadrupole magnets, which are focusing reaction products emerging from the target into the separator. Quadrupoles are followed by the first filter stage (Fig. 3.2 and 3.3). The electric field is provided by a high voltage plate condenser and magnetic field is generated by two subsequent dipole magnets. After the first filter stage, there is a velocity slit, which separates primary beam from reaction products. The second filter stage is following with the same composition as the first stage, however, in reverse order. It starts by two dipole magnets and ends by a plate condenser. Since the deflection fields of the separator are only weakly focusing, the second triplet of quadrupole magnets was added after the filter stages.

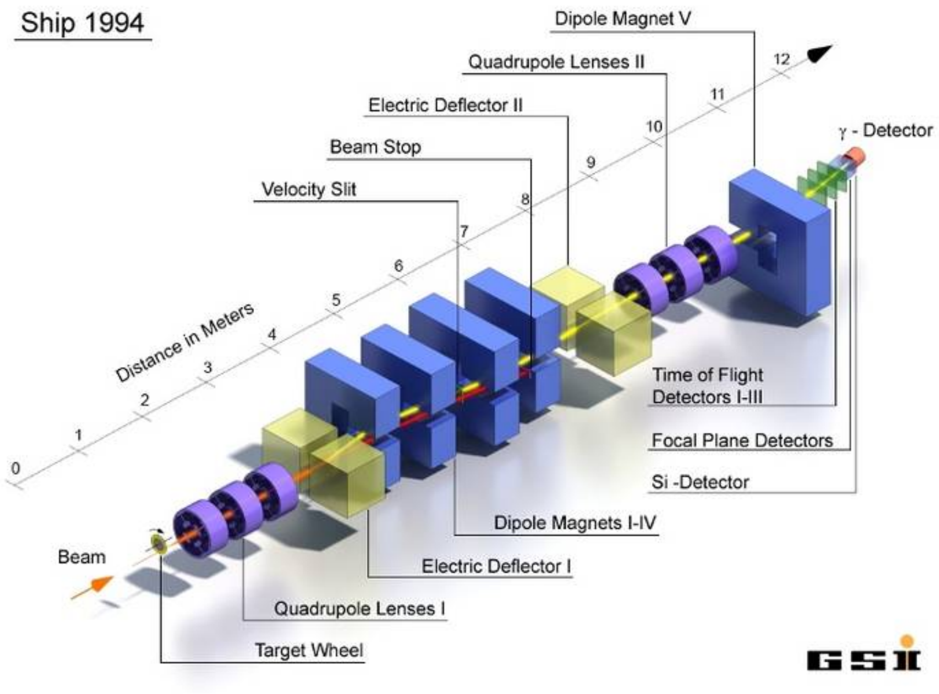

Figure 3.2: Scheme of the velocity filter SHIP after modification in the early ’90s [GSI].

The separator accepts a relative velocity width ± 5 %, angular width ± 26 mrad in both radial and axial directions and a relative charge width ± 10 %. Transmission of the reaction products is 30 – 60 % and the primary beam is suppressed by a factor of $10^7 – 10^{11}$ [Mun79].

In the beginning of the ’90s, the separator was modified to achieve higher transmission of the fusion-reaction products and better suppression of the background. The first goal was reached by placing the target closer to the first quadrupole triplet. In case of the background, a large contribution was caused by a fraction of primary beam particles, which exit the target

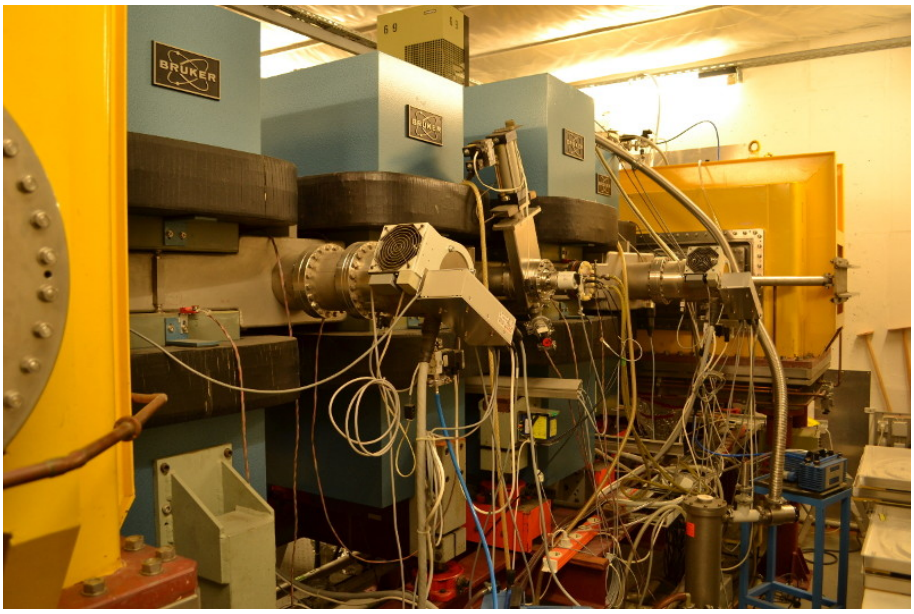

Figure 3.3: Filter stages of the SHIP. From left to right: electrostatic deflector (yellow), four dipole magnets (blue) and second electrostatic deflector (yellow).

stage with low ionization and thus high magnetic rigidity. Such particles may fly through the separator and reach the detector. In order to reduce this background, a dipole magnet with deflection angle of 7.5° was placed at the end of the SHIP. The separator is 11 m long from the target to detector [Hof00]. Depending on the reaction properties (projectile - target mass asymmetry, projectile energy), products need typically $1 - 2\,\mu$s to pass through.

3.3 Detection System

In order to investigate properties of isotopes of heavy and superheavy elements, sophisticated detection setup was assembled at the end of the SHIP. It consists of time of flight detectors, an array of silicon detectors and a germanium clover detector. To identify events of nuclei with a very low production, α decay chains are used [Hof07]. Achieved sensitivity is about one decay chain per five days [Hof00].

3.3.1 Time of Flight Detectors

Construction of time of flight (TOF) detectors (Fig. 3.4) is based on thin carbon foils (≤ 30 μg/cm^2) and microchannel plates (MCP). The foils are placed perpendicularly to the beam direction. As the ions pass through the foil, secondary electrons are emitted and accelerated by an electric field with intensity $1 - 2$ kV/cm. Parallel electrodes generating the field are 38 mm apart. At sides between them, additional correction electrodes are placed (in the Fig. 3.4, they are denoted as FCF - Field Correction Frames). The foil for emission of secondary electrons is built in the first electrode. Similarly, the second electrode has a window filled by a thin carbon foil in trajectory of the beam, so that both electrodes are transparent to the passing ions.

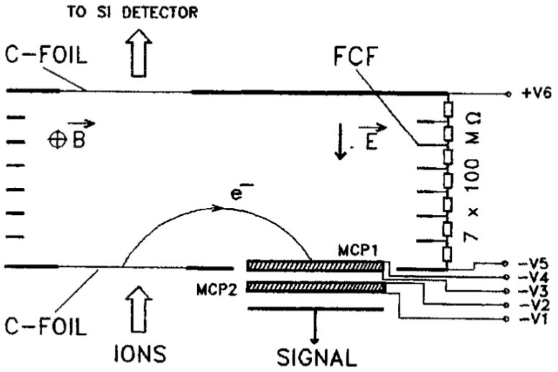

Figure 3.4: Schematic drawing of time of flight detector used at the SHIP, see text for details. Reprinted from [Sar96].

Apart from the electric field, a magnetic field perpendicular to the plane of Fig. 3.4 and 3.5 is applied on secondary electrons. Trajectory of secondary electrons is therefore bent and the electrons hit MCP1, which is placed beside the emission foil. MCP2 is situated 2 mm under MCP1. MCPs have surface of 63 cm^2, from which the used effective area has 55 cm^2. Signals are collected by an anode placed 3 mm under MCP2.

TOF system consists of two detectors as in Fig. 3.5 or three detectors (we will refer to them as TOF1, 2, 3) in order to enhance efficiency. The TOF1 serves as a start detector, TOF2 and also TOF3 (if used) serve as the stop detectors of the TOF system. The emission foil of the TOF1 detector has area of 73 cm^2 (99x74 mm^2) and in case of the TOF2 detector it is 52 cm^2 (95x55 mm^2). The third detector is closest to the silicon detector array and it has the same proportions as the TOF2 detector. To compare, silicon detector in trajectory of the ions has dimensions 80x35 mm^2.

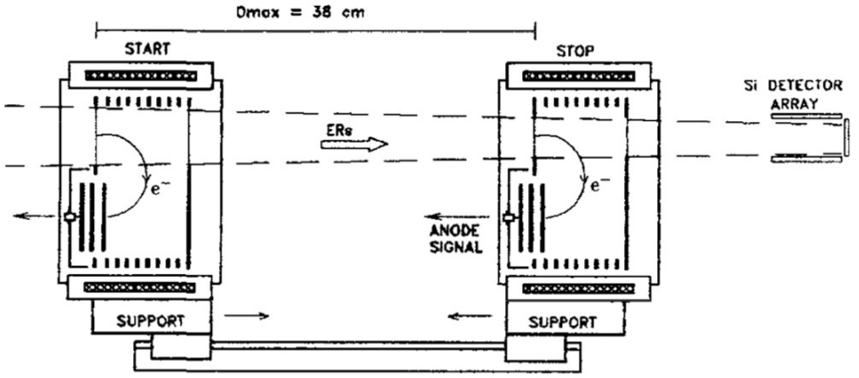

Figure 3.5: Placement of TOF1 (start) and TOF2 (stop) detectors in front of the silicon detector array. Reprinted from [Sar96].

Detection efficiency for low energy heavy ions is 99.8 % in case two TOF detectors are used. Transparency to products of fusion evaporation reactions is 100 %. Time resolution of

700 ps was achieved for fusion products, which is sufficient to distinguish them from scattered projectiles and target-like nuclei (Fig. 3.6). Another important feature of TOF system is to provide signals for (anti)coincidences with silicon detector array and thus differentiate decays from implantations of incoming ions in silicon detectors [Sar96].

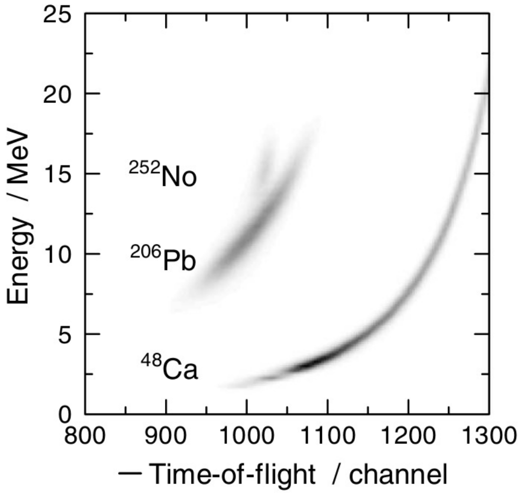

Figure 3.6: Spectrum of time of flight (in channels) versus energy of ions for reaction ^{48}Ca + ^{206}PbS. There are three distinctive groups: scattered projectiles (^{48}Ca), scattered target nuclei (^{206}Pb) and evaporation residues (^{252}No). Reprinted from [Hof07].

In case of asymmetric reactions (the projectile is significantly lighter than the target nucleus), kinetic energy of ERs is low and the TOF system becomes an obstacle which further slows down ERs. Therefore in last experiments with production of superheavy elements, changes were made to gain sufficient implantation depth of ERs in end silicon detector. Only two TOF detectors were used and the foil inside the second electrode was replaced by a grid of gilded tungsten wires. Thickness of wires is 20 μm, spacing is 3 mm and they are oriented vertically. Although replacement of foil by the grid decreased transmission of the detector by 0.67 %, the benefit was in reduction of scattering and energy losses of heavy ions in the TOF system [Hof12; Hof07]. In our measurements, all three TOF detectors were used.

3.3.2 Silicon Detectors

Stop detector is a 300 μm thick position sensitive silicon detector (PSSD) with active surface of 80x35 mm^2 divided into 16 strips. The ions that passed through the SHIP are implanted into the PSSD and time, energy and position of their implantation and subsequent decays are measured. The detector is sensitive mainly to α decays, fission and proton emission. However, under certain conditions also β decays can be measured [And04].

Strips of the PSSD are 5 mm wide and position sensitive in the vertical direction. Each strip has a relative position resolution 150 μm (FWHM - full width at half maximum) and energy resolution 14 keV (FWHM) for α decays of implanted nuclei [Hof00].

Implantation depth of reaction products is smaller than the range of α particles in the silicon detector. For example, implantation depth of Po nucleus with kinetic energy 20 MeV is $\approx 3.8\,\mu$m and range of 7 MeV α particle is $\approx 40\,\mu$m. In this case, the probability that α particle is fully stopped in the PSSD is $\approx 55\,\%$.

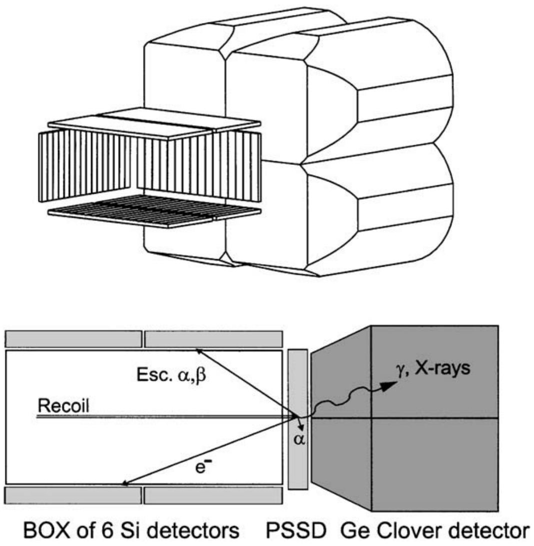

Figure 3.7: Assembly of silicon and germanium detectors at the end of the SHIP. In upper part of the image, from left to right, there are BOX detectors, the PSSD and germanium detectors. One of the BOX detectors is missing, so that the PSSD is visible. In bottom part, there is a sectional side view of the system. Reprinted from [And04].

Six $300\,\mu$m thick silicon strip detectors similar to PSSD are placed around it upstream the beam (Fig. 3.7). They detect escaped particles from the PSSD - α particles, electrons and fission fragments. The six detectors create a 7 cm deep box in front of the PSSD, therefore they are often called the BOX detectors. Neighbouring strips of the BOX detectors are galvanically connected to groups of 2 or 4 and thus reducing the total number of 96 strips to only 28 segments. Coverage of the BOX detectors is 80 % of the remaining solid angle $2\,\pi$ [And04; Hof00].

Partial signals left in the PSSD and the BOX detectors by escaping α particles from the PSSD can be added together, resulting in higher detected statistics. However, the energy resolution of summed signals is 40 keV for α particles. Silicon detectors are cooled down to 263 K [Hof00].

Right behind the PSSD, there is mounted additional silicon detector (Veto detector) of the same size and thickness as the PSSD with four energy-sensitive segments [Hof12]. The veto detector is used to filter out particles, which fly through the PSSD, for example high-energy protons [And04]. These particles leave similar energy in the PSSD as escaped α particles.

3.3.3 Germanium Clover Detector

To detect γ rays, a germanium clover detector is placed behind the PSSD (Fig. 3.7). It is mounted outside SHIP vacuum, behind 1 mm thick aluminium window [Hof07]. The clover detector is either a VEGA type or so called "SHIP Clover". Each of four crystals forming VEGA type clover has diameter 70 mm and length 140 mm. Together they create a block with dimensions (124x124x140) mm^3. "SHIP-Clover" consists of smaller crystals, which have diameter (50-55) mm and length 70 mm. Whole "SHIP-Clover" has dimensions (102x102x140) mm^3 [Hes10].

3.4 Data Acquisition and Electronics

Signals are processed by fast analogue to digital converters with 3.5 μs conversion time and 128-word FIFO buffers (first in first out). For position signals, shaping time constant of 0.3 μs is used and in case of energy signals, shaping constant is 2.0 μs [Hof00].

Signals from strips of the PSSD are taken separately from top and bottom end of each strip to gain position information. Afterwards, corresponding top and bottom signals are summed to obtain energy. Signals from PSSD and BOX detectors are split into two branches. One branch with 10× amplification is for low energy signals up to $\approx$ 16 MeV and the other one is without amplification for high energy signals up to $\approx$ 300 MeV [Ant05]. Exact values of upper limits may vary from experiment to experiment, in case of our measurements, the limits were as stated.

There are two time intervals for measuring delayed particle-γ correlations. Time measurement in the first interval is covered by TAC and it is for time differences $< 5\,\mu$s. This interval is determined by the coincidence time of the data acquisition and we refer to events registered during one window as coincidences. The time resolution is 200 ns. Second interval is for time differences $> 25\,\mu$s, where time is measured by continuously running clock. Upper time limit for correlations above 25 μs is restricted by random correlations and resolution in this interval is 1 μs. Time (5-25) μs between these two intervals is unavailable because of dead time of data acquisition [Ant11].

3.5 Data Analysis

To analyse experimental data, we use analysis code implemented in Go4 analysis framework developed at GSI (GSI Object Oriented On-line Off-line system) [Go4]. More details on the analysis code can be found in Appendix A: Analysis Code for the New Detection System at SHIP, where also the code for the old system is discussed. The new code is modification of the old one. Go4 is based on ROOT, with extensions for medium and low energy nuclear and atomic physics experiments. ROOT is object oriented analysis system created at CERN to analyse large amounts of experimental data in an efficient way [ROOT]. It can also serve as platform for building data acquisition and simulation systems.

3.5.1 Time and Position Correlation Method

To select nuclei of interest in the data analysis, we employ time and position correlation method. The method was introduced in 1979 to be used for identification of new α activities by establishing decay chains leading to known α transitions [Hof79]. Nuclei have to be implanted into position sensitive detector, where energy and time of their subsequent decays are measured. Signal from implantation of the nucleus and all decays of a given decay chain have to occur at the same position in the detector (within its position resolution). The resolution (of the order of a few $100\,\mu$m) is large compared to typical ranges of α particles in the detector, which are $(25-40)\,\mu$m. The range of recoiling nucleus after α decay is even smaller, almost by 1 order of magnitude. To minimize random correlations, there has to be also restriction on the time between signals. Minimal reasonable time window depends on the half-life of the isotope and maximal time depends on average rate in the detector.

Chapter 4

Calibrations of the Detectors

First step in the offline data analysis is thorough calibration of the detectors. Some calibrations have to be done in specific order. Concerning calibrations of the silicon detectors, ballistic calibration has to be done first. Low energy calibration of the PSSD has to be done before the low-energy calibration of the BOX detectors and after that, high energy calibration of the BOX detectors may follow. Gamma calibration is independent from the others.

4.1 Ballistic Calibration (PSSD)

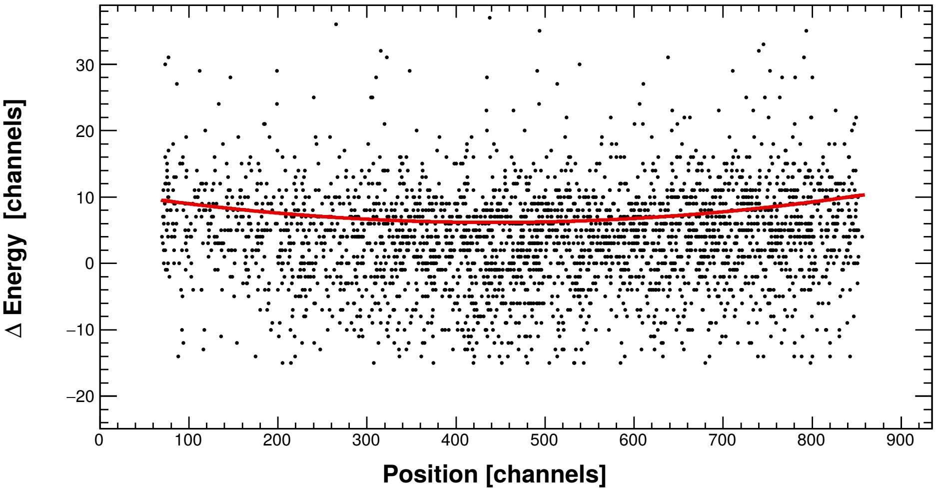

Figure 4.1: Energy differences (uncalibrated) between reference and measured energy as function of position for one strip. Red line is a fit by a quadratic function.

Position sensitivity of the PSSD is achieved by its resistive layer. Signals are read-out on top and bottom ends of each strip. As a result, a signal at one end of the strip from the event of a given energy is weaker when it occurred further from this end and stronger when it occurred closer. Position is thus determined by standard method of signal division

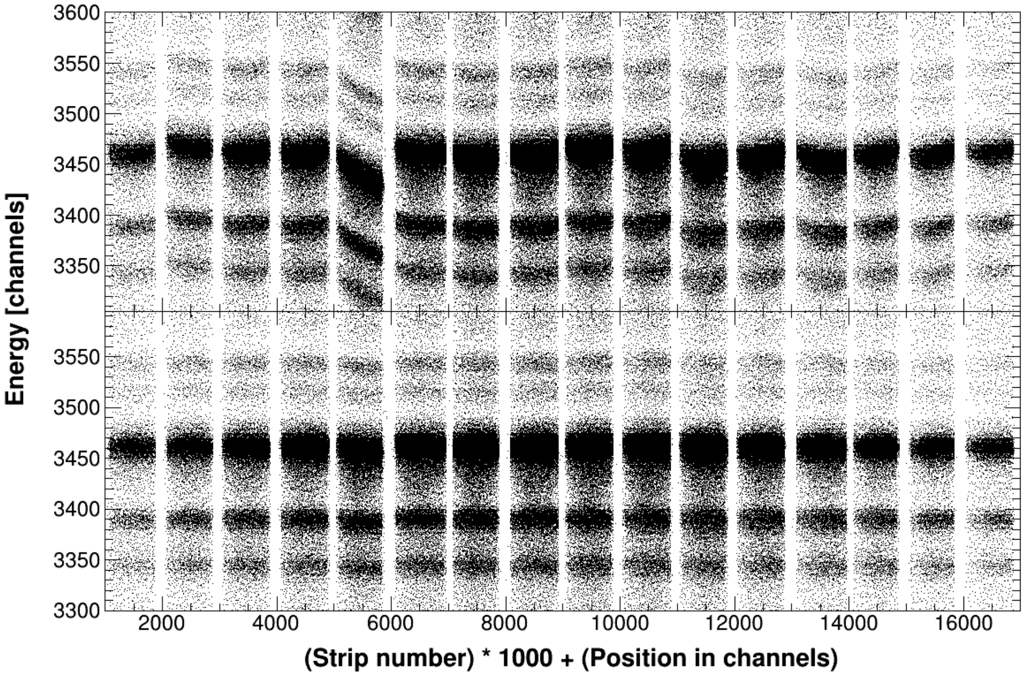

Figure 4.2: Uncalibrated energy in PSSD as a function of position along Y axis of the detector for each strip. Top panel: before ballistic calibration. Bottom panel: after ballistic calibration.

as follows:

$$Position\ top/bottom = \frac{E_{top/bottom}}{E} \cdot 35\,\mathrm{mm}, \tag{4.1}$$

where 35 mm is the length of the strip, $E_{top/bottom}$ is uncalibrated energy from top or bottom end of the strip and E is the sum of uncalibrated energy from top and bottom ends of the strip for a given event. We compare independently top or bottom positions of investigated events, therefore we do not need to do conversion $Position\ top = 35\,\mathrm{mm} - Position\ bottom$. For calibration graphs, position in channels from 0 to 900 is used instead of [mm].

This method of position sensitivity, however, has an unwanted effect. Even the summed energy signal from both top and bottom ends of a strip is dependant on position of the event along the strip. To correct energy information, so called ballistic calibration separate for each strip is necessary. For this purpose well separated peak in the α-energy spectrum is used. We determine its energy in channels and window around it, which will be now fixed for all strips. We plot differences in measured and fixed (reference) energy in the dependence on position for each strip. To obtain calibration coefficients, the dependences are fitted by quadratic functions (Fig. 4.1). This calibration also does a rough alignment of the strips. Comparison of uncalibrated and calibrated strips from the measurement discussed in this Thesis (section 5.1.2) is shown in Fig. 4.2.

4.2 Low-Energy Calibration (PSSD)

For α-decay spectra, standard energy calibration is needed. The best way is to use α decays of nuclei implanted into the PSSD. Isotopes and their α-decay energies used for low-energy calibrations in our measurements are listed in Table 5.1 and 5.6. External α-calibration source is less suitable, because the detector has thin dead layer on the surface, which degrades resolution for incoming particles. Moreover, in case of decay of implanted nucleus, a part of its recoil energy is summed with energy of α particle. Calibration by external source would be therefore shifted to lower energies. Difference for heavy nuclei is several tens of keV [Ant05]. When calibrating with α decays of implanted nuclei, isotopes with recoil energy similar to recoil energy of studied isotopes need to be chosen to achieve precise calibration. Each strip of the detector has to be calibrated separately. Linear functions are used to obtain calibration coefficients.

4.3 Low Energy Calibration (BOX detectors)

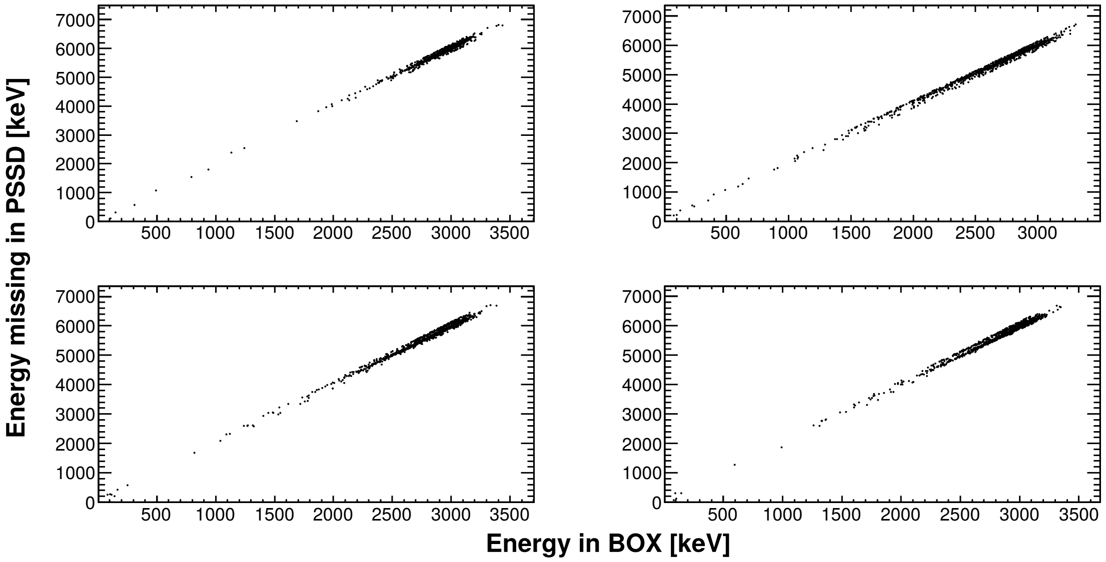

Figure 4.3: Example of calibration graphs for four different segments of BOX detectors. Y axis shows energy missing in the PSSD (calibrated) because α particle escaped, X axis shows uncalibrated energy deposited in BOX detectors by the same particle.

BOX detectors are used to detect particles escaped from the PSSD. To get a full energy left in detectors by such particle, one needs to add signals from BOX and PSSD detectors. However, escaping particle loses part of its energy in dead layers of both BOX and PSSD detectors. Summed energy is therefore smaller than would be energy left by the same particle if it was fully stopped in the PSSD. Moreover, this deficit of energy depends on angle under which the particle escapes (it has to overcome different length in the dead layer based on the angle) and thus it depends on the energy left in the PSSD (since the length of particle trajectory in the PSSD depends on the same angle).

To calibrate 28 energy sensitive segments of BOX detectors, coincidences between residual signals of escaped α particles from the PSSD and signals registered in BOX detectors are used. One has to use well separated peak in α spectrum of BOX detectors and supply value of its correct energy and a range around it in BOX spectrum to the analysis. Created calibration graphs (Fig. 4.3) show the difference of correct energy for the peak and residual energy left in the PSSD plotted against energy left in BOX detectors by corresponding event. In other words, it is dependence of energy missing in the PSSD on energy registered in the BOX detectors for escaping particles belonging to the specific peak. For this calibration, linear function is used.

4.4 Position Calibration (PSSD)

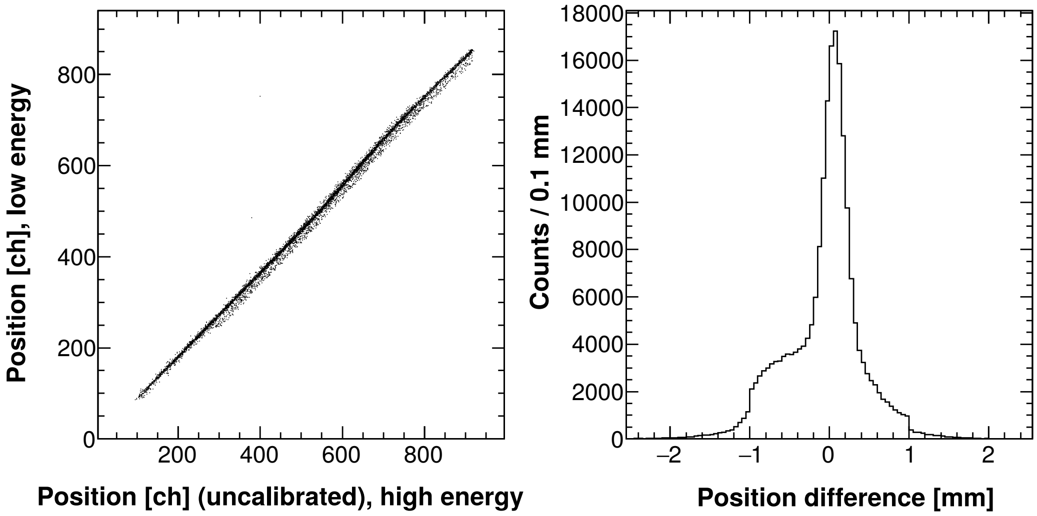

Figure 4.4: Left: Position calibration graph for positions from top end of one strip from the PSSD. Right: Position differences (positions from top end) of correlated high-energy and low-energy events in the same strip.

Position taken from the low-energy branch is not exactly the same as position taken from the high-energy branch of the electronics. This difference has to be corrected by position calibration in offline analysis. The most accurate way is to use ER-α correlations of short-lived isotope. Short half-life of the isotope allows us to use short correlation time and thus minimize number of random correlations. We plot position from low energy branch (α) against position from high energy branch (ER) and fit dependences by polynomial functions of 4^{th} order. Calibration graph for one strip of the PSSD is shown in left part of Fig. 4.4, right part of the figure shows position difference of correlated high-energy and low-energy signals. Separate position calibrations are needed for positions determined from signals from top and bottom ends of each strip.

4.5 High Energy Calibration

Calibration of the PSSD for the high energy branch of the electronics can be done similarly as the low energy calibration. To make rough calibration, one can use α peaks and extrapolation to higher energies, or the peak of projectiles in addition to α peaks. The second method has advantage, that we do not need to make large extrapolation. However, there is a shortcoming that the peak of projectiles has broad distribution and signals from projectiles suffer by pulse height defect [Ant05]. Moreover, the projectiles are not present in all of the detector strips.

In order to calibrate high energy branch of BOX detectors, events that leave signals in both low- and high-energy branches are used. One has to choose well separated peak in low-energy BOX spectrum and set its parameters in calibration conditions of the analysis. Calibration graphs plot calibrated low-energy signals against non calibrated high-energy signals. To obtain calibration coefficients, graphs have to be fitted by linear functions. This calibration is especially important for identification of fission fragments.

4.6 Gamma Calibration

4.6.1 Energy Calibration

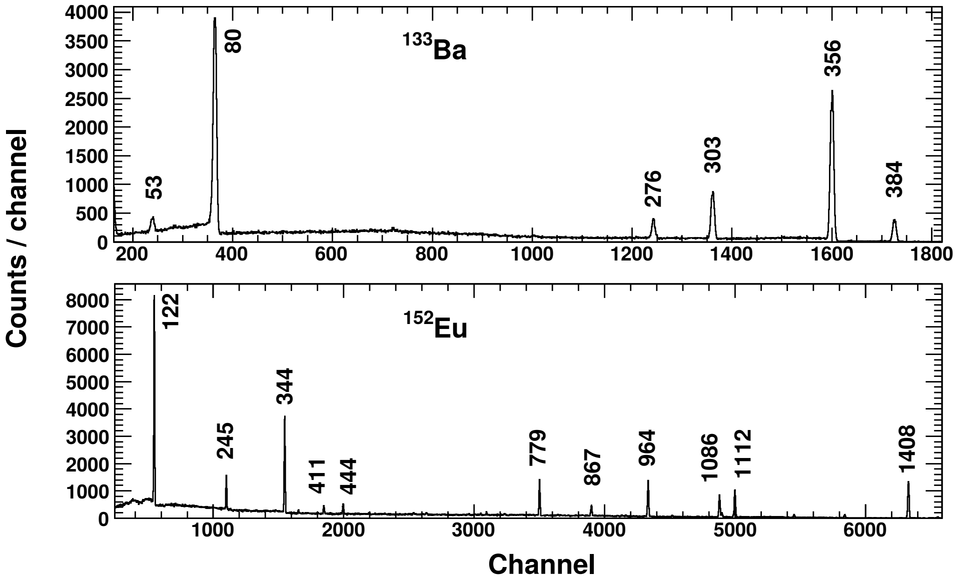

Figure 4.5: Uncalibrated γ-ray spectra with peaks labelled by their tabulated energy (rounded to keV) [Fir96]. Top panel is a spectrum of γ-ray source ^{133}Ba, bottom panel is a spectrum of source ^{152}Eu.

Gamma-ray sources ^{152}Eu and ^{133}Ba are used for calibration of germanium clover detector. Standard procedure is applied, one has to identify peaks in non calibrated spectra (Fig. 4.5) and create plots of their energy versus position in channel spectrum for each germanium crystal. Plotted dependencies are not linear, polynomial function of 3$^{\text{rd}}$ order is used to obtain calibration coefficients.

4.6.2 Efficiency Calibration

Efficiency of γ-ray detection decreases with rise of γ-ray energy. To establish dependence of relative efficiencies, one needs to plot ratios of measured and tabulated relative intensity for γ transitions from calibration sources. This relative efficiency curve then may be scaled to obtain absolute efficiency curve by using points for γ-ray energies with determined absolute efficiency. Absolute efficiency can be retrieved from experimental measurement, if there is a γ transition in coincidence with α decay and a γ-ray intensity relative to α-decay intensity is known. If such γ transitions are not present during a specific experimental run, points for the same type of clover detector established in other experiments are used. Absolute efficiency curves for our measurements are shown in Fig. 4.6(results are discussed in section 5.1.3) and 4.7(results are discussed in section 5.2.3).

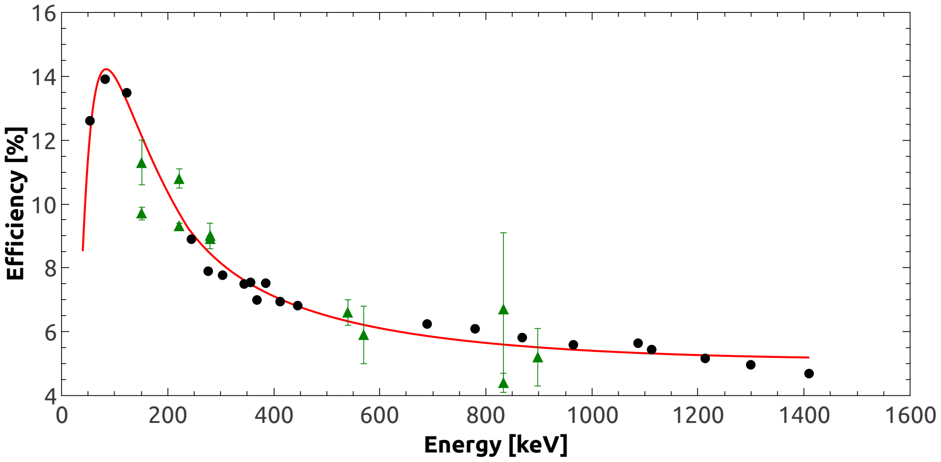

Figure 4.6: Absolute γ-ray detection efficiency for measurement of ^{194}Po. Circles are calibration points for ^{152}Eu and ^{133}Ba from this experimental run (establishing relative efficiency curves), triangles are scaling points from other experiments with known absolute efficiency.

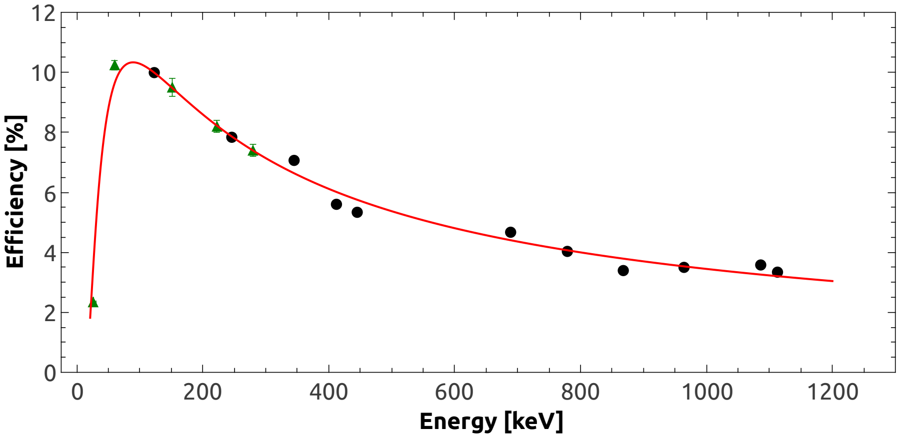

Figure 4.7: Absolute γ-ray detection efficiency for measurement of ^{192}Po. Circles are calibration points for ^{152}Eu from this experiment (establishing relative efficiency curves), triangles are scaling points from other experiments with known absolute efficiency.

Chapter 5

Results and Discussions

This chapter presents results and discussions for experiments with production of ^{194}Po and ^{192}Po. Data were obtained in three experimental runs carried out at the velocity filter SHIP. The isotope ^{194}Po was produced in run R250, while the isotope ^{192}Po was produced in runs R224 and R225. Last two runs will be together denoted in following text as R224. For ^{192}Po, also re-analysis of older data published in [Vel03] was done. In the cases where these data were included in our results, it is indicated at relevant places. Sections 5.1 and 5.2 are dedicated to γ-ray spectroscopy of short-lived isomers in both isotopes. More general discussion and systematics of similar isomeric states in even-*A* Po and Pb isotopes is presented in Section 5.3. Last two sections contain results on fine structure in α decay of ^{194}Po and ^{192}Po (Section 5.4) and reaction cross-sections alongside with HIVAP calculations (Section 5.5). Main results and discussions from Sections 5.1 - 5.3 are going to be published in [And16], partial preliminary results including cross-sections were published in [And15].

5.1 Gamma Spectroscopy of Isomeric State in ^{194}Po

5.1.1 Previous Studies of Isomer in ^{194}Po

In early measurements, the level scheme of ^{194}Po ($T_{1/2}$ = 392(4) ms [Wau93]) was deduced from in-beam studies performed at Argonne Tandem Linac Accelerator System (ATLAS) facility in USA using Fragment Mass Analyzer (FMA) [You95]. Nuclei of ^{194}Po were produced in reaction $^{28}Si+^{170}Yb \longrightarrow {}^{194}Po+4n$. Prompt γ rays were detected with an array of 10 Compton-suppressed germanium detectors mounted at the target position. The ground-state band was established up to (10^+) level, with side feeding from second (4_2^+) and (2_2^+) levels and with (11^-) level de-exciting to (10^+) level. Spin and parity assignments were based on systematics.

The most recent study, containing both in-beam and delayed γ-ray spectroscopic measurements, was carried out in the accelerator laboratory of the University of Jyväskylä employing gas-filled recoil separator RITU (Recoil Ion Transport Unit) [Hel99]. Delayed γ

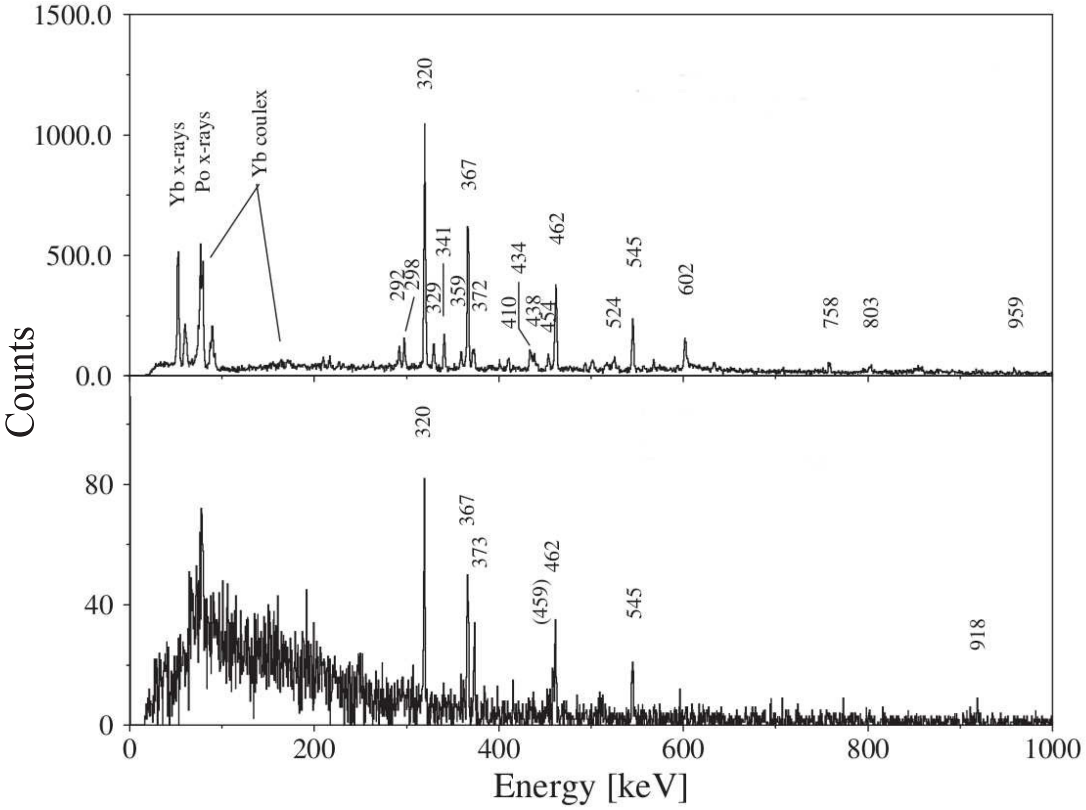

Figure 5.1: Top panel: prompt (in-beam, measured at the target position) single γ-ray spectrum of ^{194}Po; bottom panel: single spectrum of delayed (measured after implantation of ER in the end detector) ^{194}Po γ rays. Reprinted from [Hel99].

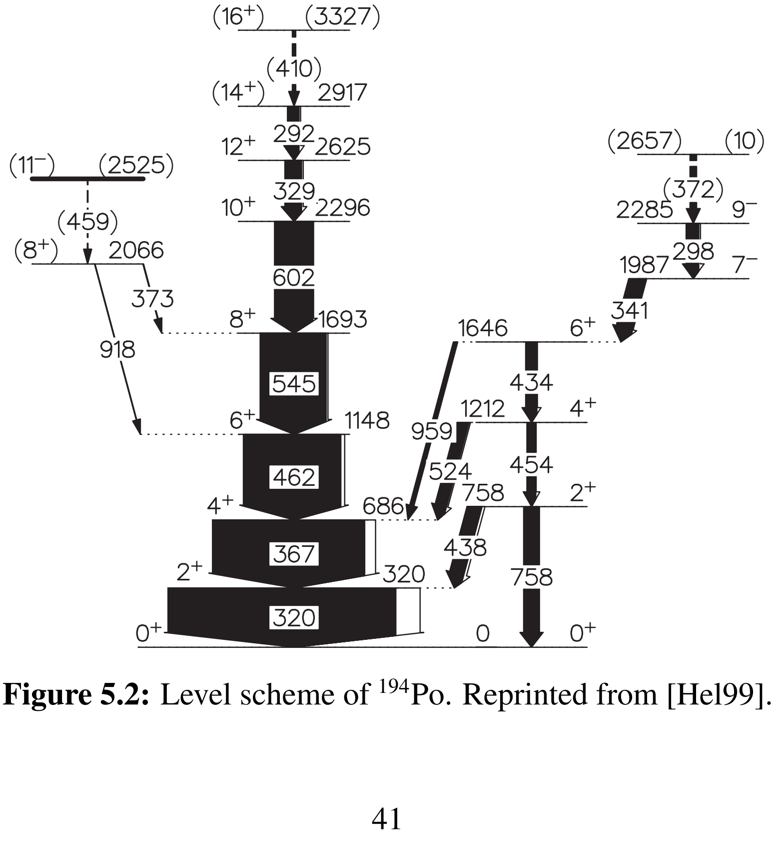

Figure 5.2: Level scheme of ^{194}Po. Reprinted from [Hel99].

rays were obtained as a by product with rather limited statistics during a run dedicated to study of ^{193}Po. Spectrum is shown in the bottom panel of Fig. 5.1. To produce nuclei, fusion evaporation reaction $^{32}S +^{166} Er \longrightarrow {}^{194}Po + 4n$ was used. An isomeric state with $I^{\pi} = (11^{-})$ and excitation energy of 2525 keV was tentatively proposed, de-exciting to the second (8_2^+) state via a 459 keV ($E3$) transition. Spin and parity assignment of the isomer was based on systematics in heavier Po isotopes and its half-life was evaluated as 15(2) μs. The (8_2^+) state was connected to the 8_1^+ state from the ground-state band via the 373 keV and to the 6_1^+ state via the 918 keV transition. No coincidences between delayed γ rays were observed.

They performed also more extensive in-beam studies of ^{194}Po γ rays. Measurements were carried out in three experimental runs, using reactions $^{28}Si + {}^{170}Yb \longrightarrow {}^{194}Po + 4n$ and $^{28}Si + {}^{171}Yb \longrightarrow {}^{194}Po + 5n$. Based on these measurements, the ground-state band was extended up to (16^+) level. The (11^-) level proposed in previous study from FMA was reassigned to 12^+ and moved to the ground-state band. Moreover, a side band from (2_2^+) up to (10) level was established. In the top panel of Fig. 5.1, summed spectrum of prompt ^{194}Po γ rays (measured in-beam at the target position) from these experiments is presented.

Suggested level scheme based on both prompt (yrast band and the side band starting at level with $E = 2657$ keV) and delayed γ rays (side band of (11^-) isomer) is shown in Fig. 5.2. Due to the limited statistics and lack of γ-γ coincidences for delayed γ rays, the part of the level scheme describing de-excitation of the isomer was only tentative.

5.1.2 Experiment

Experiment presented in this Thesis was performed at the velocity filter SHIP using the detection set up described in the Section 3.3. Isotope ^{194}Po was produced in fusion-evaporation reaction $^{56}Fe + {}^{141}Pr \longrightarrow {}^{194}Po + p2n$. New data were obtained also for ^{194}At, which was produced via $3n$ channel of the same reaction [And09].

Target material was 522 μg/cm^2 thick layer of ^{141}PrF$_3$ with 100 % natural enrichment of ^{141}Pr. Contribution of Pr corresponds to layer of 372 μg/cm^2. It was evaporated on 40 μg/cm^2 carbon backing foil and covered by another layer of 10 μg/cm^2 of carbon to increase radiative cooling and reduce sputtering of the target material.

To calibrate the PSSD, we used α decays of isotopes and isomers ^{193m,194,195,195m}Po. All of them were produced via different evaporation channels of the main reaction during the experimental run. Their α energies used for calibration and energies from our measurement are summarised in Table 5.1 in Subsection 5.1.3, alongside another α decaying isotopes produced during measurement. Resolution of the PSSD in the energy range from 6 to 7 MeV was approximately 31 keV (FWHM). For calibration of the clover detector, γ transitions of ^{152}Eu and ^{133}Ba were used. Energy resolution of the clover consisting from four Ge crystals was 1.8 keV (FWHM) for the 344 keV line from ^{152}Eu.

5.1.3 Results for ^{194}Po

Single spectrum of α particles collected during pauses between beam pulses is in top panel in Fig. 5.3. In the bottom panel, there are α particles correlated to signals from implantations of fusion reaction products (evaporation residues - ERs) into PSSD within a correlation time of three half-lives of ^{194}Po ($T_{1/2}(^{194}\text{Po}) = 392$ ms [Wau93]). Position difference of two correlated signals along the strips of PSSD was required to be ≤ 0.6 mm. There is a higher statistics for ^{194}Po in the bottom panel, because restrictions used in the correlation search result in significant suppression of the background, which allows us to use also events collected during beam pulses. Moreover, α peaks of other isotopes with longer half-lives are slightly suppressed. In total, we registered approximately 1.6 million of ^{194}Po α particles in correlations with ERs using PSSD + BOX detectors. Out of this number, 1.2 million of correlations contained α particles fully stopped in the PSSD.

Identified isotopes, measured α energies as well as energies from the literature are summarised in Table 5.1. Since the statistical uncertainty of α energy determination was negligible, only calibration uncertainty is stated, taken as the largest difference between our and reference energy. ^{190}Bi is an exception, because its α peaks were not sufficiently resolved.

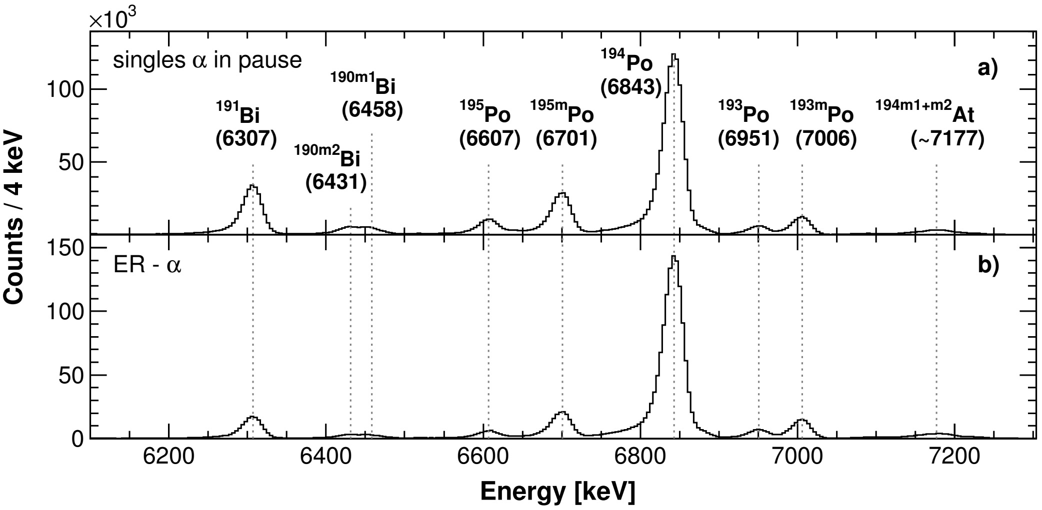

Figure 5.3: Top panel: singles α spectrum from pauses between beam pulses. Bottom panel: α particles from ER-α correlations (registered during pulse or pause) within 1176 ms (3 half-lives of ^{194}Po).

An energy spectrum of all γ rays collected in the focal-plane clover detector is shown in Fig. 5.4 (a). The amount of background γ rays is significantly reduced, when coincidences within 5 μs window measured by TAC (see Section 3.4) between γ rays and ERs were required (see Fig. 5.4 (b)). The spectrum is dominated by decays of the most strongly produced channels, i.e. αp (^{192}Pb) and $p2n$ (^{194}Po). In order to obtain γ rays originating specifically from ^{194}Po, we furthermore requested correlations of ERs to α decays of ^{194}Po for events from (b). The γ-ray spectrum for these events is shown in Fig. 5.4 (c). The application of the correlation procedure reduces the background and thus enhances γ-ray lines from the iso-

Table 5.1: List of isotopes and their α energies present in α spectrum (Fig. 5.3). Reference energies denoted by asterisk were used for calibration of the PSSD.

Isotope	E_α [keV]	$E_{\alpha\ \mathrm{ref}}$ [keV]	Reference
^{191}Bi	6307(2)	6308(3)	[Ket03]
^{190m2}Bi	6431(5)	6431(10)	[Dup91]
^{190m1}Bi	6458(5)	6456(10)	[Dup91]
^{195}Po	6607(2)	6606(5)*	[Wau93]
^{195m}Po	6701(2)	6699(5)*	[Wau93]
^{194}Po	6843(2)	6843(3)*	[NNDC]
^{193}Po	6951(2)	6949(5)	[Wau93]
^{193m}Po	7006(2)	7004(5)*	[Wau93]

mer. We identified all previously reported transitions from the isomer, mainly the 373 keV and 919 keV transitions that were suggested to feed 8^+ and 6^+ states from the ground-state band [Hel99], respectively, and subsequent transitions from this band (545, 462, 366 and 319 keV). In the most intense peak of panel (c) (319 keV), approximately 1900 counts were registered. To compare, in [Hel99] they registered roughly 200 counts in corresponding peak from the isomer (bottom panel in Fig. 5.1). Moreover, we observed transitions from the side band up to 9^- level (formerly seen only in prompt γ-ray spectroscopy [Hel99]) and we attributed four new transitions with energies of 209, 248, 362 and 494 keV to the decay of the isomer. Registered transitions are summarised in Table 5.2.

The last panel of Fig. 5.4 shows γ rays in coincidence (within 5 μs) with conversion electrons (CEs) from correlation chains ER-(γ-CE)-α(^{194}Po). The time difference for ER-(γ-CE) correlations was $(26 - 100)\,\mu$s. Strong background lines originating from isomers in ^{192}Pb (produced via αp channel) disappeared due to their short half-lives ($T_{1/2}(11^-) = 0.756(14)\,\mu$s, $T_{1/2}(12^+) = 1.09(4)\,\mu$s [NNDC]). The 248 and 209 keV transitions from the isomer in ^{194}Po are significantly suppressed, which could mean that they are highly converted and are sources of conversion electrons.

To ascertain that any of γ-ray peaks we attributed to ^{194}Po is not formed by possibly still remaining background peaks, we made further selection based on a simple idea. Occurrence of γ rays from real ER-α correlations must obey the law of radioactive decay ($N = N_0 e^{-\lambda t}$). On the contrary, background from random correlations should be distributed in time more or less constantly. Therefore, we compared γ rays from (ER-γ)-α(^{194}Po) correlations within one half-life of ^{194}Po to γ rays from correlations within four half lives. Ratio of counts in γ-ray peaks from four half-lives correlations to the counts in γ-ray peaks from one half-life correlations should be close to 1.875 for those originating in real correlations. For those originating in random correlations, the ratio should be close to 4. Gamma-ray peaks from real correlations are summarized in Table 5.2. Background or inconclusive γ-ray peaks are summarized in Table 5.3. Although the 847 keV line has the correct ratio, it behaves as a

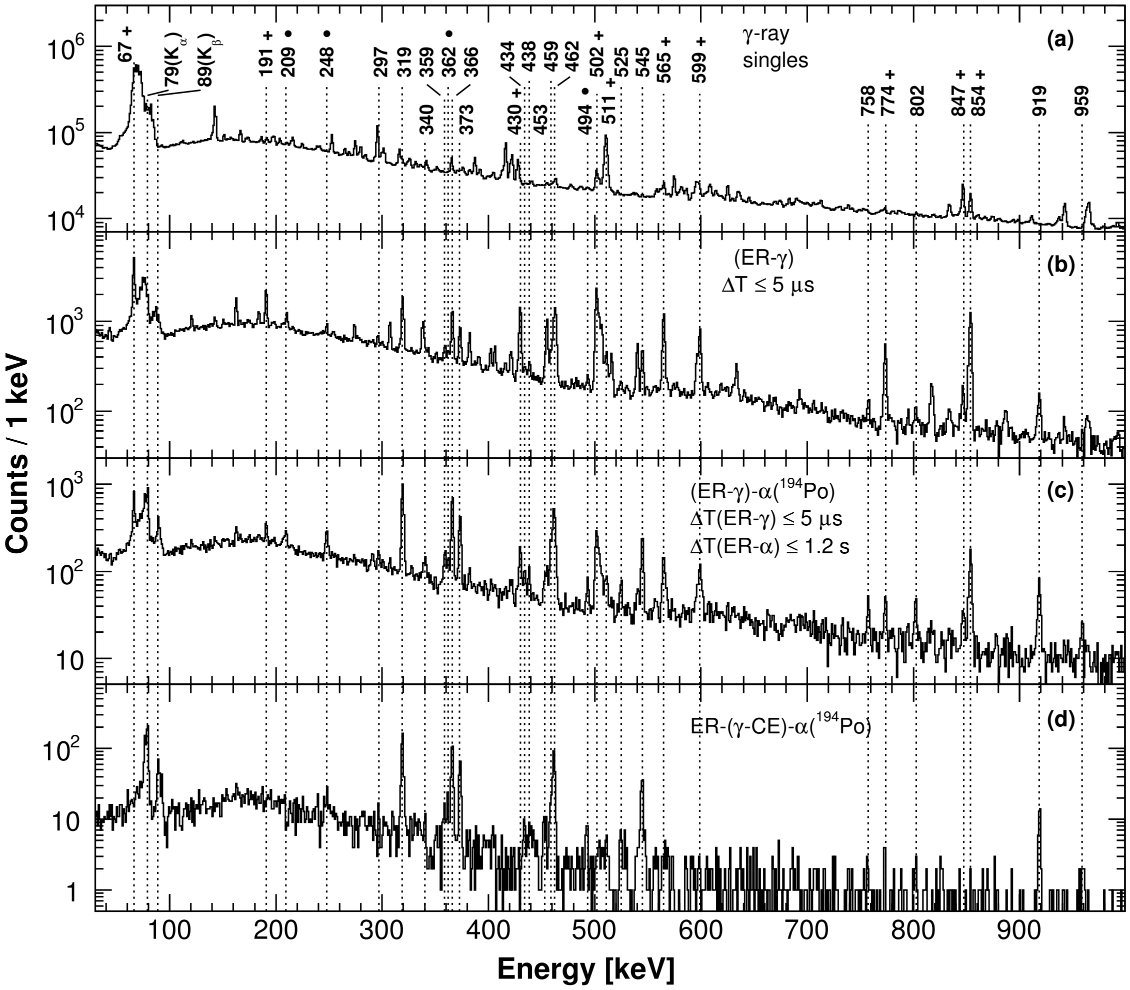

Figure 5.4: (a) all γ rays registered during production of ^{194}Po; (b) γ rays in coincidence with ERs; (c) γ rays in coincidence with ERs correlated to α decays of ^{194}Po with the correlation time up to 1.2 s; (d) γ rays in coincidence with conversion electrons from correlation chains ER-(γ-CE)-α(^{194}Po) within time window $(26 - 100)\,\mu$s for ER-(γ-CE) correlations. Energies are in keV, full circles denote new transitions from ^{194}Po, plus signs denote background lines (mostly from ^{192}Pb produced through αp channel of the main reaction).

background line in Fig. 5.4. Its height relative to height of the 854 keV background line is similar in both panel (b) and (c), while heights of γ lines from ^{194}Po increased relative to background lines in panel (c) compared to panel (b). Therefore the 847 keV line is regarded as inconclusive and labelled as a background transition in the figure.

Table 5.2: Gamma rays from (ER-γ)-α(^{194}Po) correlations, attributed to decay of the isomer in ^{194}Po. Reference energies and multipolarities were taken from previous study [Hel99]. Transitions without the reference energies were observed for the first time. Tentative multipolarity assignments are in brackets. For transitions with unknown multipolarity, we evaluated lower limits of their relative intensities using conversion coefficients for $E1$ multipolarities. In case of transitions between levels with $\Delta J = 0$ (i.e. 373, 438 and 525 keV transitions), we used conversion coefficients for $M1$ multipolarities, since this is the most probable multipolarity based on Weisskopf estimates [Fir96]. However, conversion coefficients could be increased by possible admixtures of $E0$ components or decreased by possible admixtures of $E2$ components. Intensities are relative to the intensity of the 319 keV transition. Ratio is the ratio of counts in peaks from two different correlation time windows. For real (ER-γ) coincidences from ^{194}Po it should be close to 1.875, see the text for details.

E_γ [keV]	$E_{\gamma\ \mathrm{ref}}$ [keV]	I_γ [%]	Multipolarity	Ratio
209.4(2)		≥ 14(1)		2.03(22)
248.0(1)		71(4)	($M2$)	2.03(18)
296.8(2)	297.7(3)	7(1)	$E2$	1.93(29)
319.3(1)	319.7(3)	100	$E2$	1.90(7)
340.1(3)	340.8(3)	11(1)	$E1$	1.73(22)
358.8(1)	359.2(5)	≥ 13(1)		1.98(23)
362.2(2)		≥ 11(1)		1.86(24)
366.1(1)	366.5(3)	78(3)	$E2$	1.92(8)
373.3(1)	373.1(5)	48(2)	($M1$)	1.90(12)
434.1(2)	433.9(5)	8(1)	$E2$	1.87(28)
438.4(1)	438.1(5)	8(1)	($M1$)	1.57(24)
458.8(2)	458.6(5)	≥ 24(1)		1.78(15)
461.6(2)	461.8(3)	70(3)	$E2$	1.81(9)
493.6(2)		≥ 6(1)		1.71(29)
524.9(1)	524.4(5)	6(1)	($M1$)	1.47(25)
545.0(1)	545.2(3)	33(2)	$E2$	1.76(13)
757.6(2)	758.1(5)	5(1)	$E2$	1.89(38)
802.0(2)	802.7(5)	≥ 6(1)		1.91(35)
918.5(2)	918.3(5)	14(1)	($E2$)	1.71(20)
958.7(4)	958.7(5)	2.9(4)	$E2$	1.65(44)

We deduced a half-life of the isomer using ER-γ-α(^{194}Po) correlations to be 12.9(5) μs (Fig. 5.5). We gated with an "OR" condition on the strongest lines from the isomer, i.e. 319, 366, 373 and 545 keV and fitted time differences between ER implantations and γ emissions

Table 5.3: Gamma rays in coincidence with ERs from ER-α(^{194}Po) correlations attributed to background or as inconclusive γ-ray peaks. Lines that originate in ^{192}Pb are listed with reference energies from [Fir96], remaining transitions are unassigned. Intensities are relative to the intensity of the 319 keV transition (in Table 5.2) and they are not corrected to internal conversion. Ratio is the ratio of counts in peaks from two different correlation time windows. For real (ER-γ) coincidences from ^{194}Po it should be close to 1.875, see text for details.

E_γ [keV]	$E_{\gamma\ \mathrm{ref}}$ [keV]	I_γ [%]	Ratio
191.0(1)	191.1(2)	13(1)	3.52(44)
429.8(1)		20(1)	3.30(37)
454.9(4)		8(1)	2.70(41)
501.5(3)	501.8(2)	37(2)	3.54(30)
504.0(6)	504.3(2)	18(1)	4.00(50)
506.8(5)		8(1)	3.32(57)
565.2(1)	565.4(2)	21(1)	3.22(35)
599.0(2)	599.5(2)	22(1)	2.56(26)
847.2(3)		≥ 5(1)	1.90(36)
853.5(1)	853.8(2)	29(2)	3.95(42)

by exponential function. Spectrum for the "OR" condition was created by addition of histograms separately gated by relevant transitions. Background could be fitted by a constant, because our correlation routine looks for multiple possible mother events. Thus, we can correctly reproduce background even for relatively long correlation times. Our value of half-life is consistent with the previously published value of 15(2) μs [Hel99], but more precise.

As a result of significantly higher statistics than in previous measurement [Hel99], we observed γ-γ coincidences of γ rays emitted by the isomer in ^{194}Po for the first time. Coincidences are crucial for construction of the decay scheme, since they reveal which transitions are members of one cascade. Specifically, we analysed γ-γ coincidences for seven most intensive γ transitions and with more limited statistics, also for the 918 keV transition (Fig. 5.6). Coinciding lines are listed in Table 5.4. For (ER-γ-γ)-α(^{194}Po) correlations the time window was equal to three half-lives of ^{194}Po.

The 319 keV and 366 keV transitions are in coincidence with all the other transitions analysed by γ-γ coincidences, according to both their coincidence spectra and the coincidence spectra of the other transitions (Fig. 5.6). The 373 keV transition is in coincidence with all the other transitions except the 918 keV. Behaviour of 319, 366 and 373 keV transitions is thus consistent with the level scheme from previous experiment [Hel99] (Fig. 5.2). As will be discussed later, significant difference is observation of coincidences between these transitions and the new 248 keV transition.

According to the mentioned level scheme, the 459 keV transition should be in coincidence with all the other transitions from the isomer. However, in its coincidence spectrum,

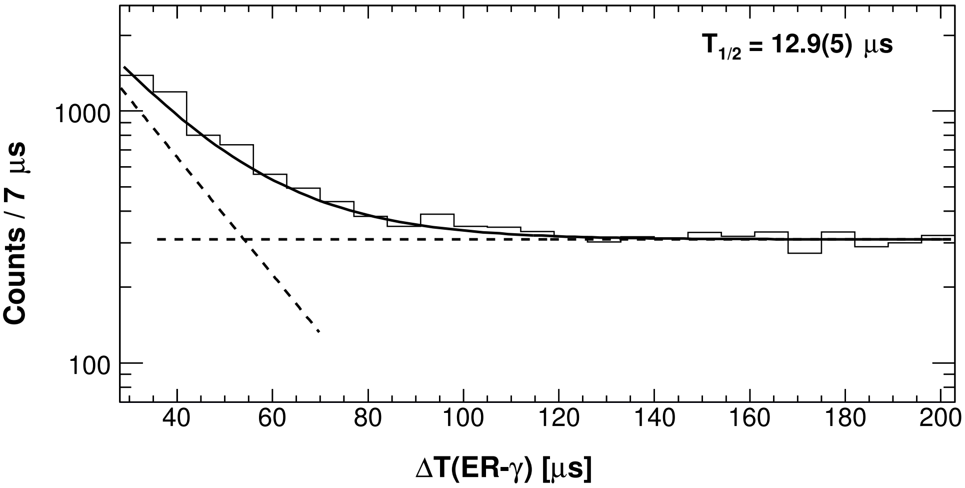

Figure 5.5: Time difference between ERs implantations and subsequent emissions of γ rays from ER-γ-α(^{194}Po) correlations with an "OR" gate on 319, 366, 373 and 545 keV transitions. Solid line represents the fit by exponential function plus constant, the two components are indicated separately by dashed lines.

Table 5.4: List of γ-γ coincidences for de-excitation of the isomeric state in ^{194}Po (from Fig. 5.6). Energies are given in keV, tentative coincidences are written in italic.

Gate	Coinciding lines
248	*Po K x rays*, 319, 366, 373, 459, 462, 545
319	Po *K* x rays, 248, 366, 373, 459, 462, 545, 919
366	Po *K* x rays, 248, 319, 373, 459, 462, 545, 919
373	Po *K* x rays, 248, 319, 366, 459, 462, 545
459	Po *K* x rays, *248*, 319, 366, 373
462	Po *K* x rays, *248*, 319, 366, 373, 545
545	Po *K* x rays, 248, 319, 366, 373, 462
919	Po *K* x rays, 319, 366, 462

the lines 545 keV, 462 keV and 919 keV are absent. It also seems that the 459 keV line is missing in corresponding spectra of these transitions (Fig. 5.6). Although peaks of 459 keV and 462 keV transitions are not sufficiently resolved, the common peak is in spectra of 545 keV and 918 keV lines thinner and shifted towards 462 keV. In spectra of 459 keV and 462 keV transitions, the common peak is completely absent.

In order to minimize mixing of coincidences with 459 and 462 keV transitions, which partly overlap, we used strict gates for these transitions in Fig. 5.6: (457.0 – 459.5) keV for the 459 keV transition and (460.5 – 463.5) keV for the 462 keV transition. Thus, we avoided most of the overlapping region at the cost of lower statistics. To make sure that we did not miss mutual coincidences between the 459 and 462 keV transitions, we also created a spectrum gated on the energy of both of these transitions, including the overlapping region:

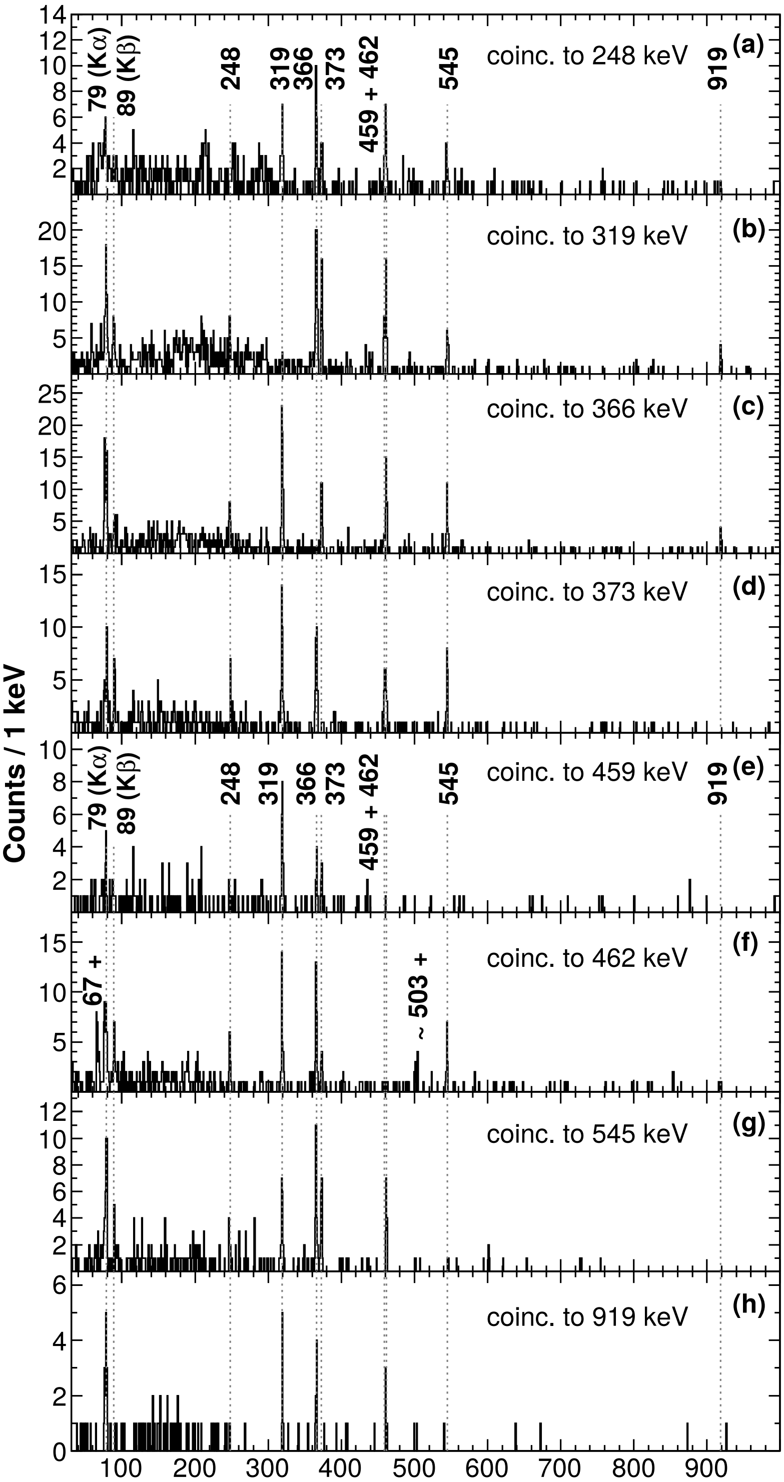

Figure 5.6: Gamma-gamma coincidences for the isomer in ^{194}Po from correlation chains (ER-γ-γ)-α(^{194}Po): γ rays in coincidence with (a) 248 keV, (b) 319 keV, (c) 366 keV, (d) 373 keV, (e) 459 keV, (f) 462 keV, (g) 545 keV and (h) 918 keV transition. Gamma lines marked by a plus sign in panel (f) are from ^{192}Pb, the $\approx$ 503 keV line consists of 502 and 504 keV transitions [NNDC]. These transitions are in coincidence with the 463.4 keV transition from the same isotope, which is partly overlapping the coincidence gate for the 462 keV transition.

(457.0 – 463.5) keV. The result in top panel of Fig. 5.7 shows no counts significantly over the level of the background. To further illustrate the absence of coincidences between the 459 keV and subsequent transitions according to former decay scheme (Fig. 5.2), we created spectrum with an "OR" gate on 545, 462 and 919 keV transitions (i.e. summed spectrum of separate coincidence gates on each of the transitions). Then we compared it to γ rays from an "OR" gate on all transitions which are in coincidence with both the 459 and the 462 keV lines (i.e. 248, 319, 366, 373 keV) in the bottom panel of Fig. 5.7.

Since the 459 keV transition is in coincidence with the 319 and 366 keV transitions, it may feed the 4^+ state of the ground-state band. Nevertheless, it is also in coincidence with the 373 keV and possibly the 248 keV transition and its position in decay scheme remains unclear. Keeping in mind the exception of the 459 keV transition, coincidence spectra of 545, 462 and 918 keV transitions agree with the level scheme.

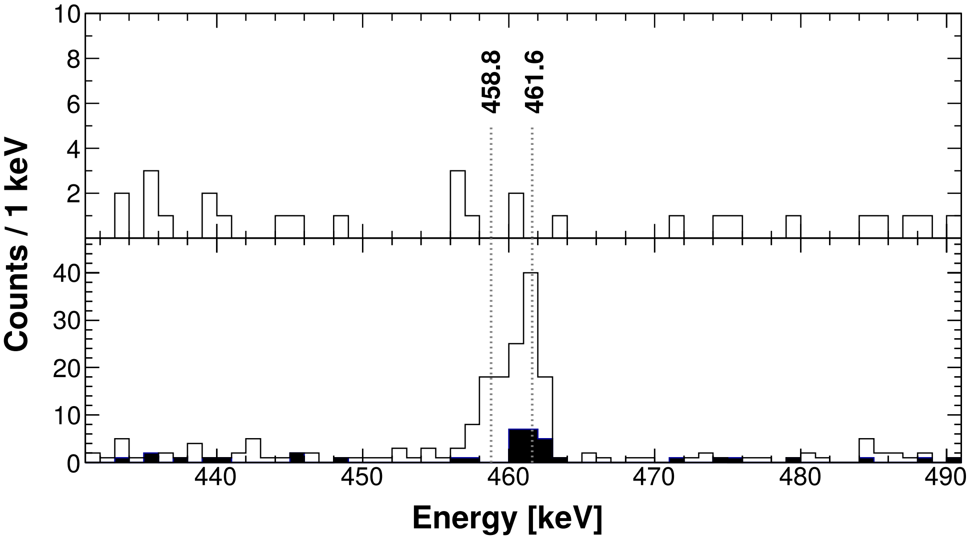

Figure 5.7: Coincidence analysis of the 459 and 462 keV transitions. Top panel: coincidences within a gate of (457.0 – 463.5) keV. Bottom panel: coincidences with 248, 319, 366 or 373 keV transitions (open histogram) compared to coincidences with 462, 545 or 919 keV transitions (solid histogram).

The new 248 keV transition is in coincidence with all investigated transitions, except of the 919 keV transition. However, missing γ-γ coincidences between the 248 and the 919 keV transition (possibly also between 459 and 919 keV) are likely to be caused by low intensity of the 919 keV line. We would expect only few counts, and there is one count at right energy in both panel (a) and (h), which is inconclusive given the level of the background. Based on these observations, we suggested to replace the 459 keV transition by the 248 keV transition in the decay scheme.

5.1.4 Discussion for ^{194}Po

Our observation is summarised in Fig. 5.8, which shows a modified decay scheme from previous study [Hel99]. In this scheme, we included only transitions observed in our measurement.

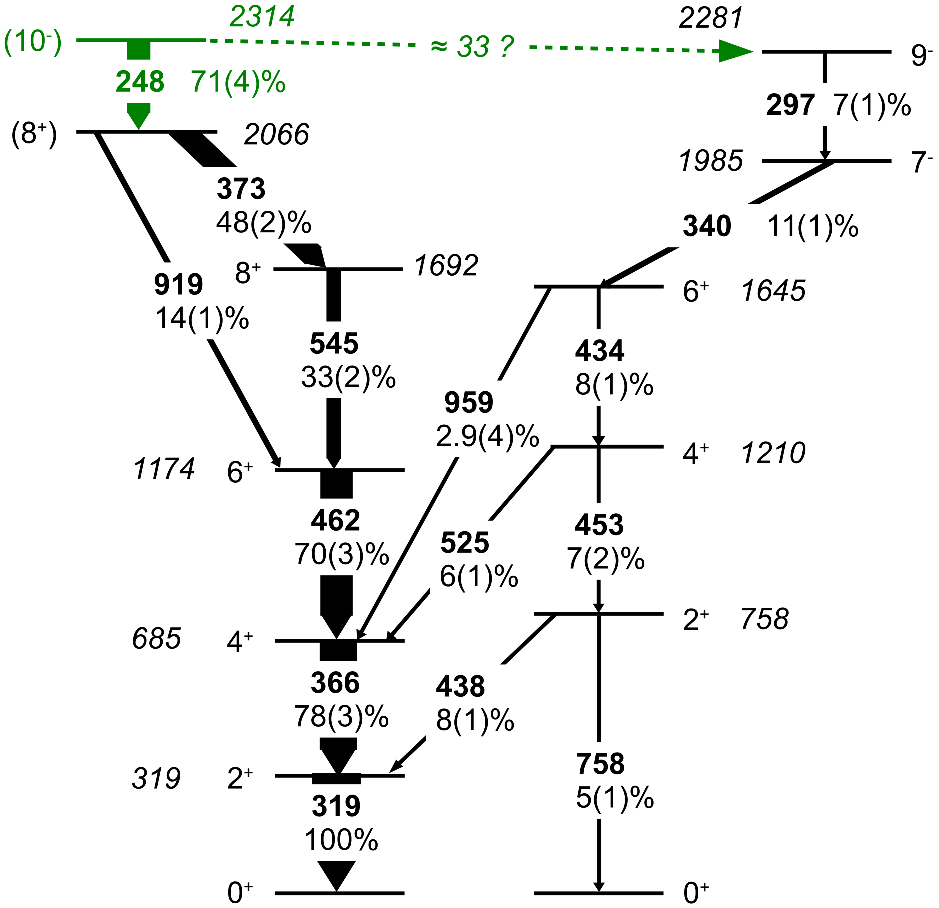

Figure 5.8: Decay scheme of the isomeric state in ^{194}Po. It is a part of the scheme from [Hel99] modified accordingly to our observation. Proposed changes are highlighted by a green color. A transition with energy ≈ 33 keV was not observed, but we discuss its possible existence in the text. Relative intensities were determined from (ER-γ)-α(^{194}Po) correlations (Fig. 5.4). The 453 keV transition was not clearly visible in the resulting spectrum, therefore we determined its relative intensity using ER-(γ-CE)-α(^{194}Po) correlations.

In order to determine multipolarity of the 248 keV transition, we deduced K-conversion coefficient from summed coincidence spectrum ("OR" condition) for gates on 319, 366, 462, 545 and 373 keV transitions (Fig. 5.9) to be 2.3(4). Theoretical K-conversion coefficients are 2.56(4) for the $M2$ multipolarity, 0.271(4) for the $E3$ multipolarity and values for $E1$, $E2$ and $M1$ multipolarities are also below 1 [BrIcc]. Our value is only an upper limit, since we cannot rule out additional sources of Po K x rays, as e.g. significant $E0$ component of $\Delta J = 0$ transitions (373, 525 and 438 keV) or other unobserved highly-converted transitions. However, all theoretical values of K conversion coefficients for possible multipolarities of the 248 keV transition except for $M2$ are well below 1, thus contribution of other sources of

Po K x rays would have to be high. In addition, Po K x rays in coincidence with the 248 keV transition seem to be relatively less abundant than in coincidence with the most of the other transitions (Fig. 5.6). To illustrate this, we can compare number of K x rays to number of the 366 keV transitions directly from the spectra, ratios of these numbers are 0.5(4) for coincidences with the 248 keV transition, 1.1(2) for coincidences with the 319 and 1.4(3) for coincidences with the 373 keV transition. Moreover, when we compare γ spectrum from (ER-γ)-α(^{194}Po) correlations with spectrum from ER-(γ-CE)-α(^{194}Po) correlations (Fig. 5.4 (c) and (d)), we can see that the 248 keV line is suppressed compared to most of the other lines from the isomer in the latter spectrum, which indicates that this transition is highly converted. These observations strongly suggest that the 248 keV transition is of $M2$ multipolarity.

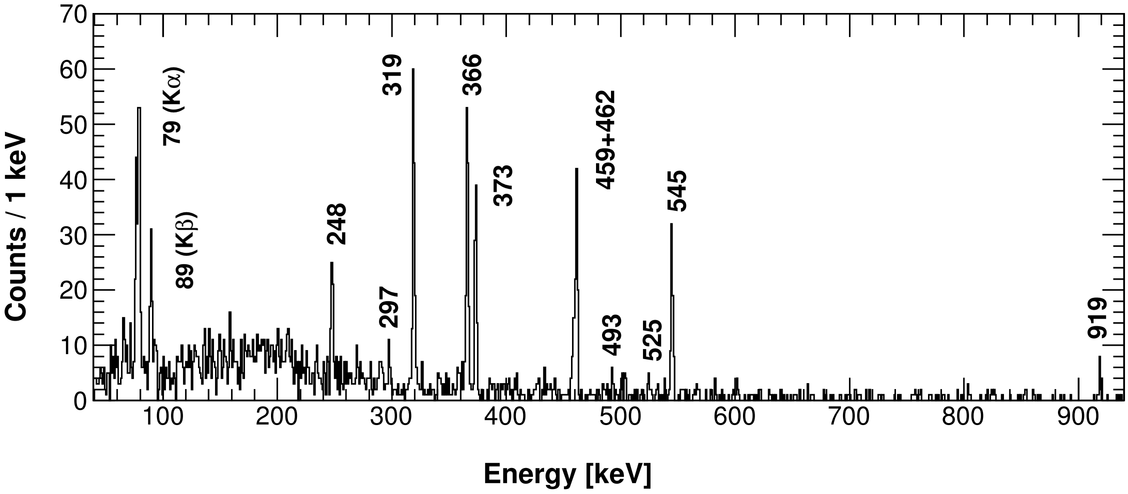

Figure 5.9: Summed coincidence spectrum ("OR" condition) for gates on 319, 366, 462, 545 and 373 keV transitions.

Another approach to assign the multipolarity is to investigate an intensity balance in γ-γ coincidences. Assuming population of the 8^+ level in the ground-state band by the 373 keV transition only, and applying the gate on 373 "OR" 545 keV transition, the intensities of 248 and subsequent 366 and 319 keV transitions should be the same (see the decay scheme in Fig. 5.8). We compare the results in Table 5.5, where the intensity of the 248 keV transition was calculated for several possible multipolarities. The intensity of the 462 keV transition is not included in the table due to possible admixtures of the 459 keV transition. The comparison favours $M2$ character of the 248 keV transition, although uncertainties are large and $E3$ assignment might also be possible.

To sum up, our data show $M2$ as the most probable multipolarity of the 248 keV transition, which leads to an initial isomeric level with $I^\pi = (10^-)$. This assignment is unexpected, as no such isomer has been identified in neighbouring isotopes. The configuration of this state is uncertain, since our measurement cannot provide a direct information on the structure and there is no systematics to compare with. Various configurations can

Table 5.5: Intensity balance of 248, 462, 366 and 319 keV transitions obtained from γ-γ coincidences. Intensity of the 248 keV transition was calculated for several possible multipolarities. Intensities are relative to the intensity of the 319 keV transition. ICC_{tot} stands for total internal conversion coefficient, values were taken from [BrIcc].

Gate: 373 "OR" 545 keV			
Transition energy [keV]	Multipolarity	ICC_{tot}	Intensity [%]
319	$E2$	0.1051(15)	100(20)
366	$E2$	0.0713(10)	105(21)
248	$E1$	0.0489(7)	27(8)
248	$M1$	0.854(12)	48(14)
248	$E2$	0.228(4)	32(9)
248	$M2$	3.50(5)	117(33)
248	$E3$	1.661(24)	69(20)

form a 10^- level in even-A Po isotopes. For example, 10^- states with configurations of $\pi\{13/2^+[606] \otimes 7/2^-[514]\}$ and $\pi\{11/2^+[615] \otimes 9/2^-[505]\}$ were theoretically predicted in ^{194}Po within the framework of Nilsson model [Shi10]. However, the only observed 10^- excited state in Po isotopes with determined configuration is the level with the excitation energy of 3.2 MeV in ^{210}Po. A configuration of $\pi[h_{9/2} \otimes i_{13/2}]$ was attributed to this level [Fan71], which is the same as the configuration of 11^- isomers in Po isotopes [Maj86]. Therefore, it is plausible configuration also for our (10^-) isomeric state. The proton character of the state, especially the latter configuration, is supported by a hindrance of the possible de-excitation via the 33 keV ($M1$) transition to the 9^- level. Since lower-multipolarity transitions are usually preferred, the 33 keV transition would need to be hindered by a significant change of the configuration between the two states. Indeed, the corresponding 9^- levels in Po isotopes are of different, neutron character [Fan90; Maj90]. Parallel ($M2$) and ($M1$) transitions in ^{194}Po would then connect states with the same configurations as the parallel $E3$ and $E2$ decays of 11^- isomers to the 8^+ and 9^- states in $^{198-202}$Po, where $E3$ transitions are more intense than $E2$ [Maj90; Fan90]. For transitions with respective energies, ratios of Weisskopf half-life estimates corrected for internal conversion are $t_{1/2}(E3)/t_{1/2}(E2) \approx 700 - 1000$ for $^{198-202}$Po and $t_{1/2}(M2)/t_{1/2}(M1) \approx 100$ for the (10^-) state in ^{194}Po. Based on Weisskopf estimates, these lower-multipolarity transitions should then be even more preferred in case of $^{198-202}$Po than in ^{194}Po.

The overall intensity balance in the decay scheme (Fig. 5.8) is adequate, especially considering possibility of small unobserved side feedings. The exceptions are the subsequent 373 and 545 keV transitions with intensities of 48(2) % and 33(2) %, respectively. The intensity of the 373 keV transition was calculated using conversion coefficient for $M1$ multipolarity. However, admixtures of electric multipoles are possible, which would affect the intensity. Admixtures of $E0$ would increase while admixtures of $E2$ would decrease the transition intensity. Similarly, the intensity of the 248 keV transition preceding the 373 keV transition may be affected (decreased) by $E3$ admixtures. Nevertheless, since the ground-state band was firmly established by in-beam studies [Hel99], our γ-γ coincidences strongly place the 373 keV transition above the 8^+_1 level. Therefore, the intensity balance cannot be improved by moving the 373 keV transition to another place.

Transitions at the right part of the scheme (side band), originating at 9^- level with an energy of 2281 keV, were previously observed only in in-beam measurement at RITU [Hel99]. In our study, we observed these transitions in delayed γ-ray spectroscopic data, which means these levels are populated by the decay of an isomeric state. Possible explanation may be 33 keV transition (unobserved in our measurement) from (10^-) isomeric level to 9^- level or another isomeric state above 9^- level. The 9^- level itself cannot have half-life long enough to be the isomer populating side-band transitions, because its decay was observed in-beam.

Possible $E0$ components of $\Delta J = 0$ transitions between side-band and ground-state band (438 and 525 keV) were discussed in previous studies based on missing intensities [Hel99; Ber95; Alb91]. However, our statistics was not sufficient to create coincidence gate on side-band transitions to investigate intensity balance in detail.

One could expect presence of a 421 keV ($E2$) transition between (8^+) 2066 keV level and 6^+ 1645 keV level as well as a 622 keV ($M2$) transition between (10^-) 2314 keV and 8^+ 1692 keV level. However, we did not observe evidence of either transition. Based on the amount of the background, we estimated upper limits of relative intensities to be $\lesssim 2.4\,\%$ for the 421 keV and $\lesssim 2.2\,\%$ for the 622 keV transition.

5.2 Gamma Spectroscopy of Isomeric State in ^{192}Po

5.2.1 Previous Studies of Isomer in ^{192}Po

Previous studies of ^{192}Po ($T_{1/2} = 33.2(14)$ ms [Bij96]) were also carried out at RITU at JYFL [Hel99]. The ground-state band up to (10^+) level was established based on in-beam measurements with reaction $^{36}Ar + {}^{160}Dy \longrightarrow {}^{192}Po + 4n$. Moreover, three transitions from the band (262, 343 and 518 keV) were registered also in delayed γ-ray measurements (employing the same reaction) at the focal plane, which was the first observation of the isomer in ^{192}Po. Half-life was estimated to be of the order of 1 μs and an isomeric level was inferred to be above (8^+) state.

A more recent study of delayed γ rays from ^{192}Po was performed at the velocity filter SHIP at GSI in Darmstadt (Germany) using fusion evaporation reaction $^{52}Cr + {}^{142}Nd \longrightarrow {}^{192}Po + 2n$ [Vel03]. All transitions from the known part of the ground-state band were observed and in addition, new transitions were attributed to the isomer. Gamma-ray spectrum and supposed level scheme are shown in Fig. 5.10. It was suggested, that above the (10^+) state, there is a state with $I^\pi = 11^-$, which de-excites via 154 keV transition to the (10^+) state.

Half-life of the isomer was deduced to be 580(100) ns. No γ-γ coincidences were registered.

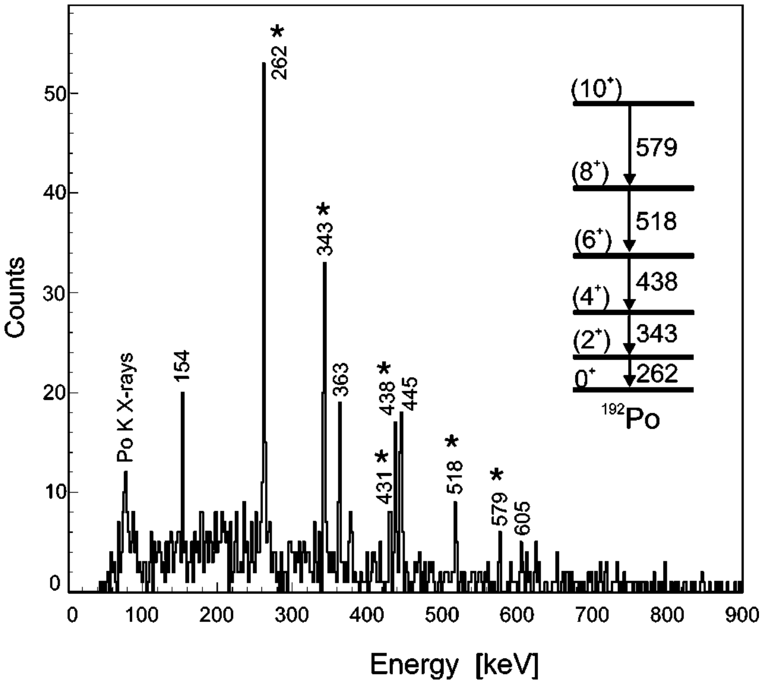

Figure 5.10: Spectrum of γ rays from the isomeric state in ^{192}Po reprinted from [Vel03]. Deduced level scheme is placed as an inset.

5.2.2 Experiment

This work presents data from later experiment performed at the velocity filter SHIP. In this measurement,^{192}Po was produced in the reaction $^{51}V + {}^{144}Sm \longrightarrow {}^{192}Po + p2n$. Also isotope ^{192}At was studied during the experiment, it was produced via $3n$ channel of the same reaction [And06].

The targets were produced from ^{144}SmF$_3$ with 96.47 % isotopic enrichment. Two targets of different thickness were used during the measurement, one with layer of 546 μg/cm^2 and the second with layer of 301 μg/cm^2 of the target material. These layers correspond to 392 μg/cm^2 and 215 μg/cm^2 of pure Sm, respectively. In both cases, the material was evaporated on the 40 μg/cm^2 carbon backing and covered by a 10 μg/cm^2 carbon layer.

For α calibration of the PSSD, energies of ^{192}Po and products of reactions with heavier Sm isotope admixtures in the target were used. Nuclides and their energies are summarised in Table 5.6. Energy resolution of the PSSD was 35 keV (FWHM) for the ^{192}Po peak (7167 keV).

Ge-clover detector was calibrated using γ rays of ^{152}Eu. To achieve higher precision of calibration, we made separate calibration for lower energies (up to $\approx$ 700 keV) and separate calibration for higher energies (over $\approx$ 700 keV). Energy resolution of lower-energy part was 2.5 keV (FWHM) for the 344 keV line of ^{152}Eu. In higher-energy part, resolution was 2.7 keV (FWHM) for the 964 keV line.

5.2.3 Results for ^{192}Po

Spectra of α decays from our experiment are presented in Fig. 5.11. Alpha decays from pauses between beam pulses are in the top panel, while α-decay events from time and position correlations with implantation signals of ERs are in the bottom panel. Upper limit for position difference of two correlated events was set to be ≤ 0.7 mm. Correlation time was 132.8 ms, which is equal to 4 half-lives of ^{192}Po ($T_{1/2}$ = 33.2 ms [Bij96]). Due to short correlation time, α peaks of other isotopes than ^{192}Po are highly suppressed in ER-α spectrum. In total, we registered approximately 110 000 ER-α(^{192}Po) correlations using PSSD + BOX detectors, out of which 83 000 correlations involved α particles fully stopped in the PSSD. Produced isotopes, measured α-decay energies and reference energies are listed in Table 5.6. As for the analysis of ^{194}Po, only calibration uncertainty is significant.

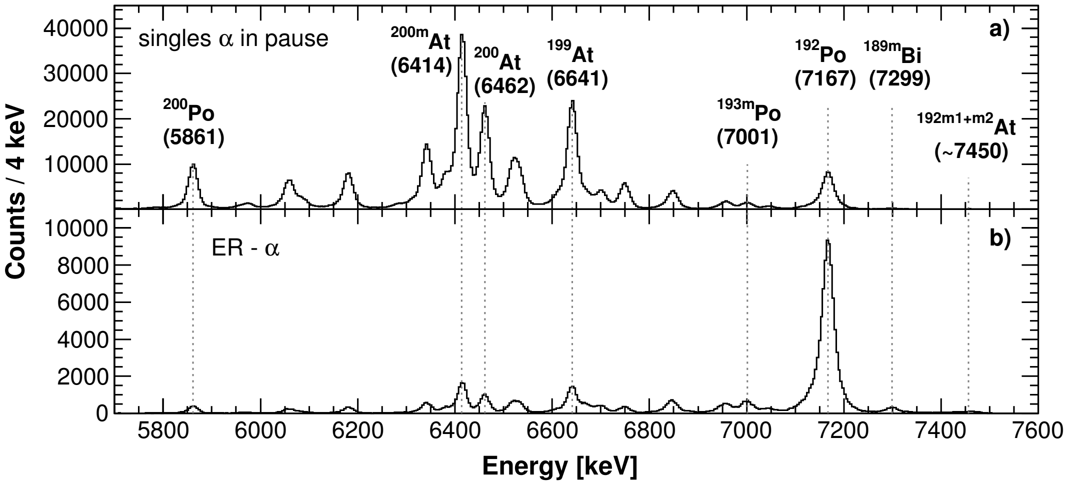

Figure 5.11: Top panel: singles α spectrum from pauses between beam pulses. Bottom panel: α events (registered during pulse or pause) from ER-α correlations within 132.8 ms time window and position difference up to 0.7 mm.

Table 5.6: List of isotopes and their α energies identified in spectra in Fig. 5.11. Reference energies used for calibration of the PSSD are denoted by an asterisk.

Isotope	E$_\alpha$ [keV]	E$_{\alpha\ \mathrm{ref}}$ [keV]	Reference
^{200}Po	5861(4)	5862(2)*	[Tay96]
^{200m}At	6414(4)	6412.0(18)*	[Ryt91]
^{200}At	6462(4)	6464(2)	[Huy92]
^{199}At	6641(4)	6643(3)*	[NNDC]
^{193m}Po	7001(4)	7004(5)	[Wau93]
^{192}Po	7167(4)	7167(4)*	[Vel03]
^{189}Bi	7299(4)	7295(5)	[Ket03]

To search for ^{192}Po γ rays, we used (ER-γ)-α(^{192}Po) correlations, similarly as in the case of ^{194}Po. Correlation time was 132.8 ms as for ER-α correlations mentioned above. Large suppression of unwanted events is shown in Fig. 5.12 (the lower energy part of the spectrum) and Fig. 5.13 (the higher energy part of the spectrum). Both figures compare a spectrum of all registered γ rays (top panel), a spectrum of γ rays in coincidence with any evaporation residue (middle panel) and the spectrum of γ rays from (ER-γ)-α(^{192}Po) correlations. In the peak of the most intensive (262 keV) transition, we registered 177 counts. In previous experiment [Vel03], number of counts in corresponding peak was ≈ 80 (Fig. 5.10).

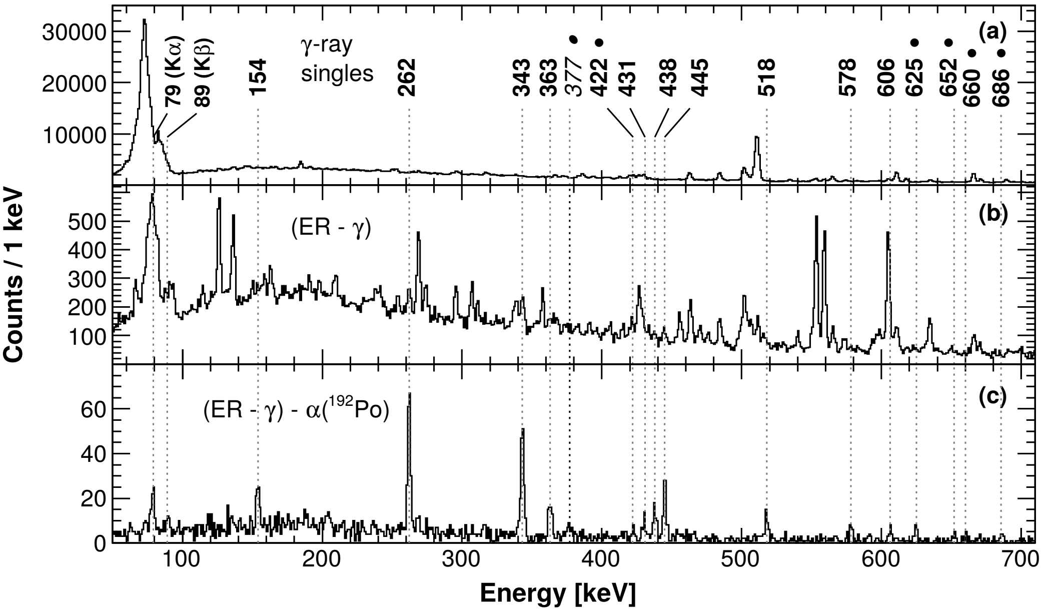

Figure 5.12: Lower-energy parts of γ-ray spectra: (a) all γ rays collected during measurement with production of ^{192}Po; (b) γ rays registered in coincidence with ERs; (c) γ rays in coincidence with ERs correlated to α decays of ^{192}Po. New transitions are denoted by full circles, the γ line with label written in italic is tentative.

On the basis of comparison of spectra in Fig. 5.12 and 5.13, we are confident to assign γ-ray peaks, that emerged in (ER-γ)-α(^{192}Po) correlations and were invisible or very weak in ER-γ coincidences only, to the isomer in ^{192}Po. We confirmed all previously-known transitions, including ground-state band transitions down from (10^+) level with energies 578, 518, 438, 343 and 262 keV. Moreover, we attributed 14 new γ transitions to the isomer, however, 6 of them are only tentative. All γ-ray peaks assigned to the ^{192}Po are summarised in Table 5.7.

We also re-analysed data from [Vel03], which were taken during the experiment R199. To compare production of ^{192}Po, in R224 around 74 000 α decays of ^{192}Po were registered in pauses between macropulses and in R199 it was around 115 000 α decays. We used the same time window as for R224 and a broader position window due to worse position resolution, the difference in position had to be ≤ 1.0 mm. The peak of 262 keV line had $\approx$ 120 counts for R199 compared to $\approx$ 180 counts for R224. More strict correlation conditions resulting in significant data reduction were probably used in previous analysis of R199, since only ≈ 80 counts were present in the peak of the 262 keV line in [Vel03]. Based on the numbers of α

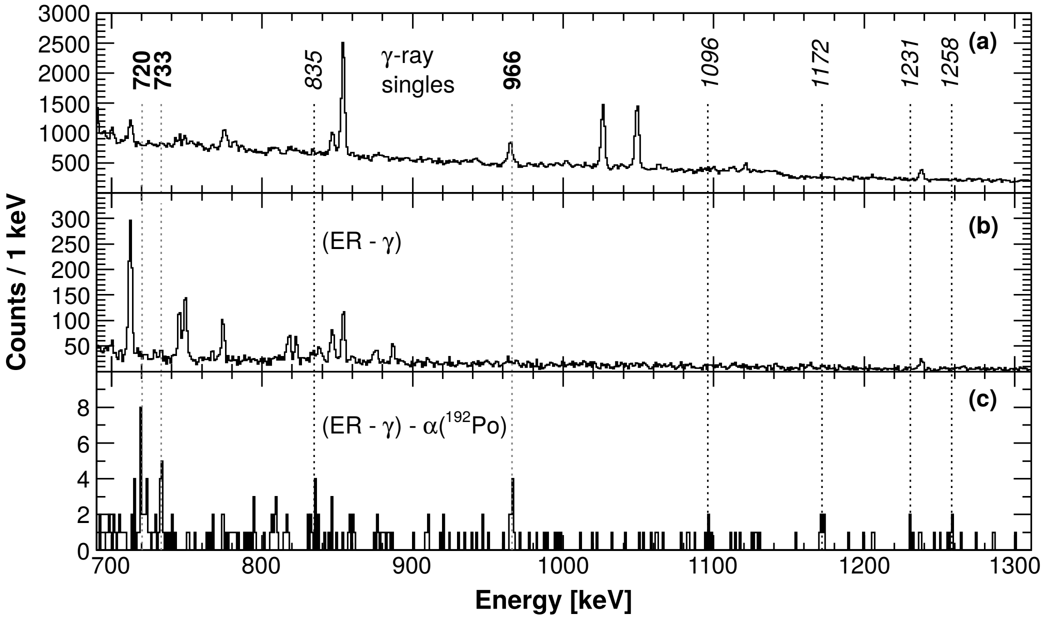

Figure 5.13: Higher-energy parts of γ-ray spectra: (a) all γ rays collected during measurement with production of ^{192}Po; (b) γ rays registered in coincidence with ERs; (c) γ rays in coincidence with ERs correlated to α decays of ^{192}Po. All transitions are new. Gamma lines with labels written in italic are tentative.

Table 5.7: Gamma rays attributed to the isomer in ^{192}Po from (ER-γ)-α(^{192}Po) correlations. Reference energies were taken from [Vel03]. Gamma transitions without reference energies were observed for the first time, tentative lines are written in italic. Intensities are relative to the intensity of the 262 keV line. Multipolarities of transitions from ground-state band are based on decay scheme from [Hel99], multipolarities of 154, 363, 445 and 733 keV transitions are discussed in text. For the rest of listed transitions, we evaluated lower limits of their relative intensities using conversion coefficients for $E1$ multipolarities.

E_γ [keV]	$E_{\gamma\,\mathrm{ref}}$ [keV]	I_γ [%]	Multipolarity	E_γ [keV]	I_γ [%]	Multipol.
153.9(3)	154	27(5)	($E1$)	624.6(4)	≥ 12(4)	
262.1(1)	262	100	($E2$)	651.8(7)	≥ 6(3)	
343.1(2)	343	90(10)	($E2$)	659.6(10)	≥ 7(3)	
362.8(3)	363	32(5)	($E2$)	685.7(6)	≥ 7(3)	
376.8(10)		≥ 18(4)		720.4(10)	≥ 14(4)	
422.4(5)		≥ 6(3)		733.1(4)	7(3)	($E3$)
430.7(5)	431	≥ 14(4)		*834.6(10)*	≥ 6(3)	
437.9(3)	438	26(5)	($E2$)	965.7(10)	≥ 8(3)	
445.0(2)	445	52(8)	($M1$)	*1096(1)*		
517.8(4)	518	22(5)	($E2$)	*1172(1)*		
578.4(4)	578	13(4)	($E2$)	*1231(1)*		
606.3(4)	605	≥ 12(4)		*1258(1)*		

decays and γ rays in R224 and R199, absolute detection efficiency for γ rays was higher in R224.

Summed γ-ray spectrum from (ER-γ)-α(^{192}Po) from these experimental runs is presented in bottom panel of Fig. 5.14. It has significantly higher background than spectrum from R224 alone, especially in region of higher γ-ray energies, therefore we did not use it for singles γ spectrum analysis.

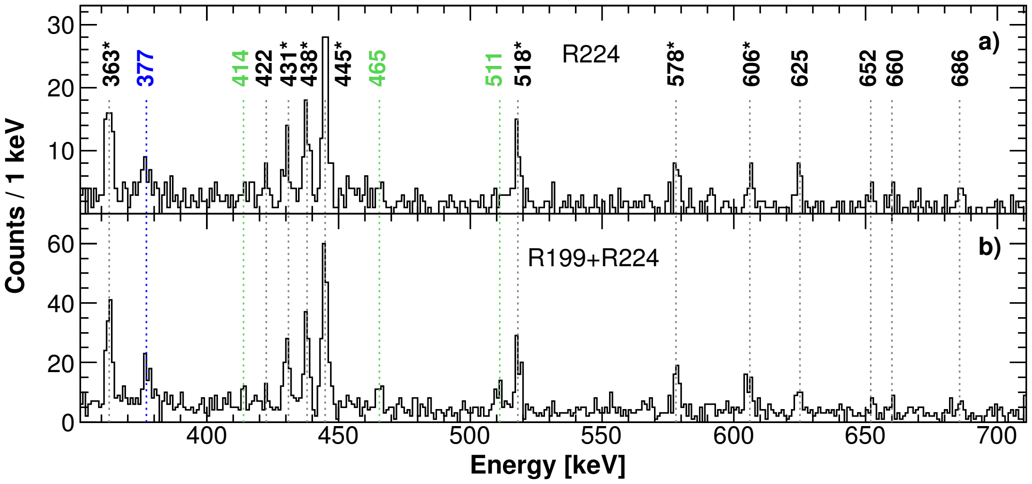

Figure 5.14: Comparison of lower energy parts of γ-ray spectra from (ER-γ)-α(^{192}Po) from experiments a) R224; b) R224 + R199. Previously observed lines are denoted by asterisk, line with blue label is only tentative. In bottom panel, lines 422, 518, 606, 625 and 686 keV have worse resolution or became less visible. On the other hand, new lines at 414, 465 and 511 keV (with green label) appeared there.

Although summing all experimental data was not beneficial for single spectrum, in case of γ-γ coincidences, we used all available statistics to gain first coincidences of γ rays emitted in decay of the isomer in ^{192}Po. Gamma-gamma coincidences from (ER-γ-γ)-α(^{192}Po) are shown in Fig. 5.15 and listed in Table 5.8.

Table 5.8: List of γ-γ coincidences for de-excitation of the isomeric state in ^{192}Po (from Fig. 5.15). Tentative lines are written in italic. Energies are given in keV.

Gate	Coinciding transitions
154	*Po K x rays*, 262, 343, 438, 518, 578
262	*Po K x rays*, *154*, 343, 363, 430, *438*, 445
343	Po *K* x rays, *154*, 262, 438, 445, *518*, *578*
363	262, 445
430	262, *343*
438	154, 343
445	262, *343*, *363*
518	*154*, *343*

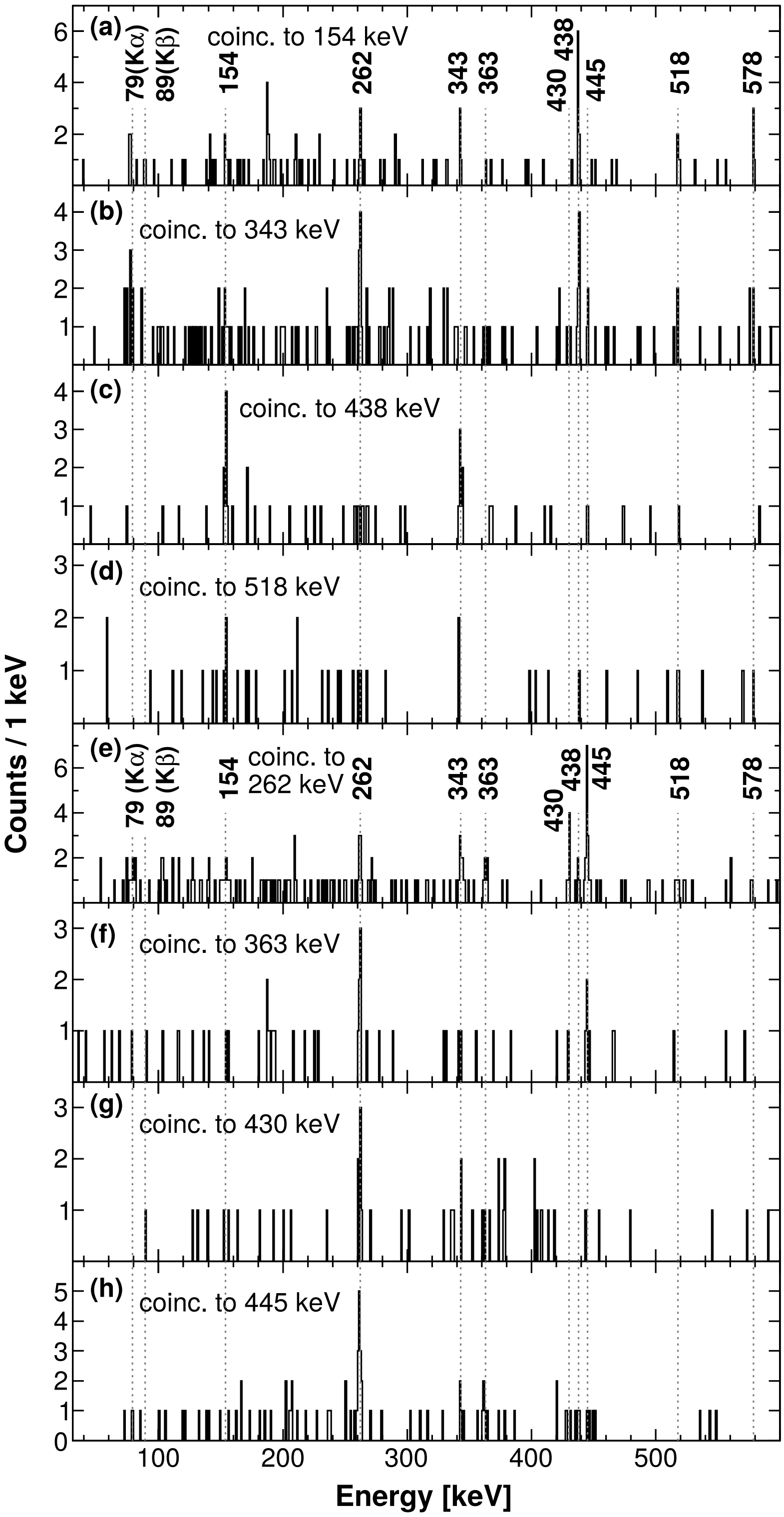

Figure 5.15: Gamma-gamma coincidences for de-excitation of the isomer in ^{192}Po from (ER-γ-γ)-α(^{192}Po) correlations: γ rays in coincidence with (a) 154 keV, (b) 343 keV, (c) 438 keV, (d) 518 keV, (e) 262 keV, (f) 363 keV, (g) 430 keV and (h) 445 keV transition.

5.2.4 Discussion for ^{192}Po

It was suggested already in [Vel03] that the 154 keV transition may de-excite (11^-) isomer above the (10^+) level of the ground-state band. The suggestion was based on supposed $E1$ multipolarity of the transition, which was deduced from the low number of observed K x rays. Firm placement into the decay scheme was not possible due to lack of γ-γ coincidences, but our γ-γ coincidence data support the suggestion (Fig. 5.15). An $E1$ character of this transition is indicated by relative intensities of subsequent transitions. If we assumed another possible character for the 154 keV transition, it would result in higher internal conversion coefficient and the relative intensity would be significantly higher (Table 5.9). In addition, any magnetic multipole can be excluded based on the low number of K x rays also in our measurement.

Table 5.9: Intensities of 154, 363 and 445 keV transitions for various possible multipolarities. Intensities are relative to the intensity of the 262 keV transition.

Multipolarity	Relative intensity [%]		
	154 keV	363 keV	445 keV
$E1$	27(4)	31(5)	45(6)
$M1$	98(15)	40(6)	52(7)
$E2$	51(8)	32(5)	47(7)
$M2$	449(67)	60(9)	68(10)
$E3$	430(64)	40(6)	52(7)

Based on the γ-γ coincidence analysis, we suggest a side-feeding of the ground-state band on top of the (4_1^+) level by the 445 keV transition. This transition is clearly in coincidence with the 262 keV transition and most likely with the 343 keV transition as well (Fig. 5.15). The side-feeding is also supported by the balance of relative intensities. The (4_1^+) level is populated by the 438 keV transition with the relative intensity of only 26(5) % while the subsequent 343 keV transition has the relative intensity of 90(10) % (Fig. 5.16). Connecting the 445 keV transition to the (4_1^+) level adds the relative intensity of 52(7) % to the feeding of the level (if we assume $M1$ multipolarity of the transition, see discussion below).

We also tentatively placed the less intensive 363 keV transition into the cascade with the 445 keV transition, because of mutual coincidences (see Fig. 5.15). However, concerning the ground-state band, the 363 keV transition has clear coincidences with only the 262 keV transition. Coincidences with the 343 keV transition are uncertain. It has to be noted, that also the 445 keV line has significantly stronger coincidences with the 262 keV than with the 343 keV transition. This may be a hint, that the 262 keV line is in fact a doublet, which is supported also by the activity with the same energy in coincidence spectrum of the 262 keV line (Fig. 5.15 (e)). To resolve this situation and the connection of the side band up to the

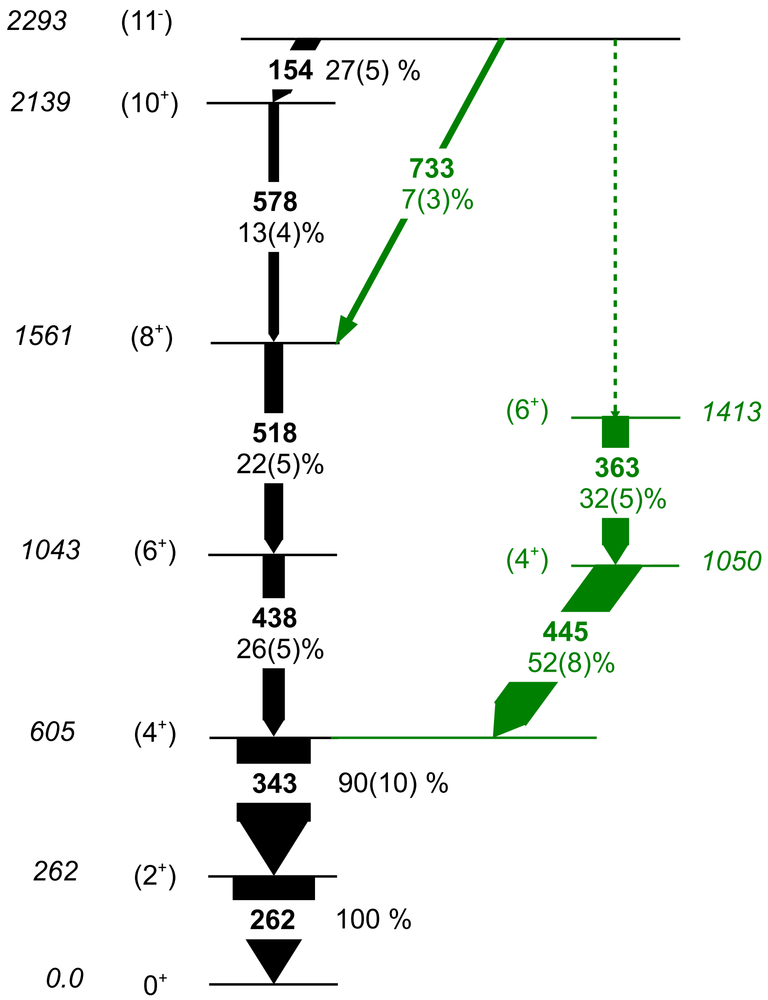

Figure 5.16: Decay scheme of the (11^-) isomeric state in ^{192}Po. Ground-state band up to (10^+) level is taken from [Hel99], placement of the 154 keV transition was proposed in a previous study [Vel03]. Our changes to the decay scheme are highlighted by green color.

(11^-) level, data of enhanced quality are needed.

In this way, we suggested two additional levels, (4^+_2) and (6^+_2). Their spins and parities were tentatively assigned based on analogous levels present in ^{194}Po [Hel99], where pairs of levels 6^+_1 and 4^+_2, 8^+_1 and 6^+_2, lie at similar excitation energies. The same situation is also in ^{196}Po for (6^+_1) and (4^+_2) levels [Alb91]. The assignments yield $(M1)$ multipolarity as the most probable based on Weisskopf estimates [Fir96] for the 445 keV and $(E2)$ for the 363 keV transition. These multipolarities were used to evaluate relative intensities of the transitions. However, if we assumed other possible multipolarities (Table 5.9), relative intensities would change only moderately (with the exception of $M2$ multipolarities). Based on intensity balance of feeding and depopulation of the (4^+_1) level, there should be no strong $E0$ component in the 445 keV transition. However, coincidences with the 363 keV transition are too weak to be employed for more precise determination of possibly missing intensity of the 445 keV transition.

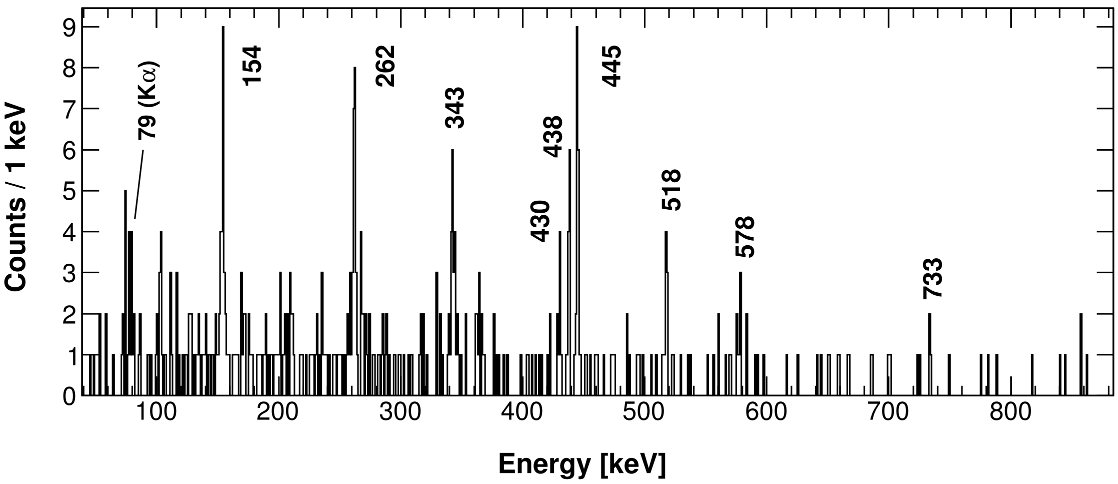

Figure 5.17: Coincident γ rays with "OR" gate on the 262, 343, 438 and 518 keV transitions of the ground-state band.

Moreover, we tentatively suggested to place the 733 keV transition between (11^-) and (8^+) levels, which gives an ($E3$) character to this transition. The placement is based mainly on energy balance and systematic presence of $E3$ transitions in decay paths of 11^- isomers in Po isotopes. Nevertheless, we also observed a hint (3 counts) of this transition in γ-γ coincidences (Fig. 5.17), while gating with "OR" condition on all subsequent transitions (262, 343, 438 and 518 keV). Adding the 154 or 578 keV transitions to the gate did not increase the number of counts for the 733 keV transition.

5.3 11^- isomeric states in even-A Po and Pb isotopes

In all even-A neutron deficient polonium isotopes from ^{210}Po to ^{196}Po and lead isotopes from ^{196}Pb to ^{190}Pb, 11^- isomeric states with dominant configuration of $\pi\{(h_{9/2})\otimes(i_{13/2})\}$ are present (Fig. 5.19) [Alb91; Maj90; Fan90; Bax90; Pol97; Man88; Dra05; Dra01]. Isomers were identified also in ^{194}Po and ^{192}Po with the same supposed spin and parity [Hel99; Vel03]. The 11^- isomers de-excite via $E2$ transitions to 9^- levels ($^{202\text{-}198}$Po [Fan90; Maj90] and ^{196,194}Pb [Dra05]), via $E1$ transitions to 10^+ levels ($^{208\text{-}204}$Po [Pol97; Bax90; Fan90] and $^{196\text{-}190}$Pb [Dra05; Dra01]) or, as in most cases, via $E3$ transitions to 8^+ levels ($^{210,208,202-196}$Po [Man88; Pol97; Fan90; Maj86; Alb91] and $^{196-190}$Pb [Dra01; Dra05]).

Concerning $E3$ transitions in this region, there is an established systematics [Ber85], which sorted out these transitions to five groups from A to E according to their strength and associated configuration change. The systematics is summarised in Table 5.10. Group A and B transitions have average $B(E3)$ value of 22 W.u. Group A is characterised by a single-particle transition $\pi i_{13/2} \rightarrow \pi f_{7/2}$, while group B by a transition $\nu j_{15/2} \rightarrow \nu g_{9/2}$. These transitions are fast due to admixtures of core states resulting in involvement of a fast core transition $3^- \rightarrow 0^+$. The latter transition belongs to group C along with transitions involving several group A and B transitions due to configuration mixing. Group C has average strength of 35 W.u. Transitions from group D are characterised by a spin-flip transition $\pi i_{13/2} \to \pi h_{9/2}$, which causes low average $B(E3)$ value of 3 W.u. Group E transitions are associated with the same orbital change as group D, but transition strengths are increased up to average value of 15 W.u. due to configuration mixing.

Table 5.10: Systematics of $E3$ transition strengths in the trans-lead region according to [Ber85]. Av. stands for average. S.-p. transition stands for the single-particle transition characteristic for the group.

Group	Av. $B(E3)$ [W.u.]	S. p. transition	Note
A	22	$\pi i_{13/2} \to \pi f_{7/2}$	admixture of $3^- \to 0^+$
B	22	$\nu j_{15/2} \to \nu g_{9/2}$	admixture of $3^- \to 0^+$
C	35		mixture of A and B
D	3	$\pi i_{13/2} \to \pi h_{9/2}$	spin-flip
E	15	$\pi i_{13/2} \to \pi h_{9/2}$	configuration mixing

The isomer in ^{210}Po de-excites via two $E3$ transitions [Man88]. One of them leads to $\pi\{(h_{9/2})\otimes(f_{7/2})\}_{8^+}$ state with strength of 19(3) W.u., which corresponds to group A transition. The second one and all other $E3$ transitions (for which the configuration of the final state is known) de-exciting 11^- isomers in Po and Pb isotopes lead to $\pi(1h^2_{9/2})_{8^+}$ states, which corresponds to group D transitions. However, for $^{202\text{-}196}$Po and $^{196\text{-}190}$Pb, $B(E3)$ values are gradually increasing with decreasing neutron number up to 25(3) and 24(4) W.u. in ^{198}Po and ^{196}Po, respectively [Maj90; Alb91]. The values are too high for group D and in case of ^{198,196}Po they are even higher than for group E transitions. Fig. 5.18 shows systematics of $E3$ strengths for transitions de-exiting 11^- isomers in even-A Po and Pb isotopes, with our new value for ^{192}Po included. Transition strengths, energies and branching ratios are summarised in Table 5.11.

It was discussed in earlier works [Alb91; Maj86], that higher $B(E3)$ values for $^{196-200}$Po might be caused by admixture of 3^- octupole collective state into the initial state, i.e. mixing of the initial state with the $\{(3^-)\otimes(8^+)\}_{11^-}$ state, and/or admixtures to the final state from either $\pi\{(h_{9/2})\otimes(f_{7/2})\}_{8^+}$ or $\{(11^-)\otimes(3^-)\}_{8^+}$ state. However, g-factor measurements limit admixtures to both initial and final states to be small and no candidates for low lying 3^- octupole states have been found for these isotopes [Alb91; Maj86]. Later, it was argued that mixing of the $\pi(1h^2_{9/2})_{8^+}$ state with the higher lying $\pi\{(h_{9/2})\otimes(f_{7/2})\}_{8^+}$ state is expected to be too small and extensive calculations do not predict increased octupole collectivity [Dra05]. Another explanation was proposed, that high $B(E3)$ values are caused by an oblate deformation, which results in an admixture of the 8^+ state with $f_{7/2}$ orbital into the lower 8^+ state. In this approach, the deformed $7/2^-[503]$ orbital, which originates in the spherical $f_{7/2}$ orbital, exchanges character with the lower lying $7/2^-[514]$ orbital stemming from the spherical $h_{9/2}$ orbital. Thus, the deformed 8^+ state causing an admixture of the $f_{7/2}$ orbital has Nilsson

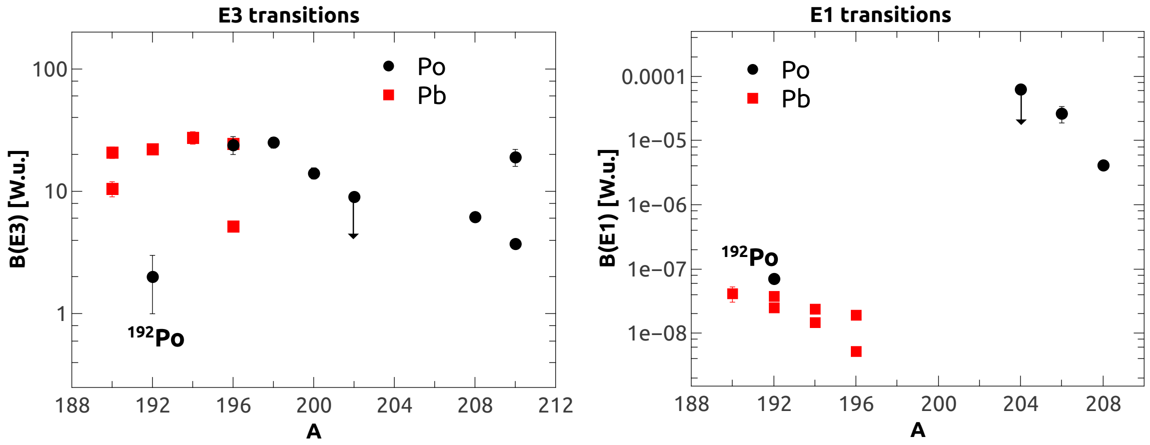

Figure 5.18: Strengths of $E3$ and $E1$ transitions de-exciting 11^- isomers in even-A Po and Pb isotopes, values and references are in Table 5.11 and Table 5.12. In case of $E3$ strength in ^{202}Po, higher of the two values was taken as an upper limit.

configuration of $\pi\{7/2^-[514] \otimes 9/2^-[505]\}$ and the configuration of the deformed 11^- state is $\pi\{13/2^+[606] \otimes 9/2^-[505]\}$. Resulting strength of an $E3$ transition between such states is ≈ 20 W.u. [Dra01; Dra05].

Table 5.11: Strengths of $E3$ transitions de-exciting 11^- isomers in Po and Pb isotopes. Values were calculated based on half-lives, energies and branching ratios taken from references. There are two values for the same transition in ^{202}Po, one with all information from [Fan90] and the other with different value of half-life published in [Beu76].

Isotope	E_γ [keV]	Branching ratio [%]	$B(E3)$ [$e^2fm^{2\lambda}$]	$B(E3)$ [W.u.]	Ref.
^{192}Po	733	21(14)	4(3)x10^3	2(1)	This work
^{196}Po	552	66(7)	6(1)x10^4	24(4)	[Alb91]
^{198}Po	712	93(1)	5.8(6)x10^4	25(3)	[Maj90]
^{200}Po	823	72(2)	3.3(3)x10^4	14(1)	[Maj90]
^{202}Po	913	69	$\leq$ 7.8(4)x10^3	$\leq$ 3.2(2)	[Fan90]
^{202}Po	913	69	1.6(8)x10^4	6(3)	[Fan90; Beu76]
^{208}Po	1175	33(2)	1.6(1)x10^4	6.2(4)	[Pol97]
^{210}Po	1292	95.3(3)	9.7(2)x10^3	3.7(1)	[Man88]
^{210}Po	661	4.7(7)	5.0(3)x10^4	19(3)	[Man88]
^{190}Pb	382	19.8(22)	2.3(3)x10^4	11(1)	[Dra01]
^{190}Pb	407	58.0(36)	4.5(5)x10^4	21(2)	[Dra01]
^{192}Pb	440	11.1(10)	4.9(5)x10^4	22(2)	[Dra01]
^{194}Pb	496	5.7(6)	6.1(7)x10^4	28(3)	[Dra05]
^{196}Pb	562	5.0(4)	5.7(5)x10^4	25(2)	[Dra05]
^{196}Pb	601	< 1.6	< 1.1(1)x10^4	< 5.0(2)	[Dra05]

We determined the 248 keV transition in ^{194}Po to have most likely $M2$ character. However, we calculated what would be its $B(E3)$ if it had $E3$ multipolarity. Resulting value is 290 W.u., deduced as an upper limit for 100 % branching ratio. If we used the relative

Table 5.12: Strengths of $E1$ transitions de-exciting 11^- isomers in Po and Pb isotopes. Values were calculated based on half-lives, energies and branching ratios taken from references.

Isotope	E_γ [keV]	Branching ratio [%]	$B(E1)$ [$e^2 fm^{2\lambda}$]	$B(E1)$ [W.u.]	Ref.
^{192}Po	154	79(12)	1.4(3)x10^{-7}	7(1)x10^{-8}	This work
^{204}Po	93	≤ 100	$\leq$ 1.3(1)x10^{-4}	$\leq$ 6.0(3)x10^{-5}	[Fan90]
^{206}Po	238	93(1)	6(2)x10^{-5}	2.6(8)x10^{-5}	[Bax90]
^{208}Po	149	67(2)	9.5(3)x10^{-6}	4.2(1)x10^{-6}	[Pol97]
^{190}Pb	43	22.2(56)	9(2)x10^{-8}	4.2(11)x10^{-8}	[Dra01]
^{192}Pb	121	20.8(8)	5.4(3)x10^{-8}	2.5(1)x10^{-8}	[Dra01]
^{192}Pb	162	68.1(14)	8.1(3)x10^{-8}	3.8(1)x10^{-8}	[Dra01]
^{194}Pb	305	48.2(14)	5.2(3)x10^{-8}	2.4(1)x10^{-8}	[Dra05]
^{194}Pb	352	45.1(14)	3.2(2)x10^{-8}	1.5(1)x10^{-8}	[Dra05]
^{196}Pb	498	68.5(11)	4.2(2)x10^{-8}	1.9(1)x10^{-8}	[Dra05]
^{196}Pb	547	24.5(8)	1.1(1)x10^{-8}	5.2(3)x10^{-9}	[Dra05]

intensity instead (with value of 42(2) % for the $E3$ multipolarity) we would have obtained transition strength of 115(7) W.u. The transition strength is too high in both cases. As can be seen in Table 5.11, even transitions with enhanced strengths have values only up to 30 W.u. Highest value in systematics of $E3$ strengths in [Ber85] is 49(10) W.u. for 372 keV transition in ^{210}At. Moreover, recommended upper limit for $E3$ strengths is 100 W.u. [Fir96].

The 733 keV transition in ^{192}Po with tentative ($E3$) character populates the (8^+) level, for which configuration different alternatives exist. The first alternative is $\pi[h^2_{9/2}]$ configuration, which follows assignments of 8^+ levels from ground-state bands in heavier Po isotopes. The second possible character of this level is $4p-2h$ oblate intruder state deduced from level-energy systematics [Jul01]. This possibility is supported by laser-spectroscopy studies [Coc11]. In the case of the first configuration, a spin-flip transition $\pi i_{13/2} \rightarrow \pi h_{9/2}$ is required for de-excitation of the (11^-) isomer. One could expect $B(E3)$ value of around 3 W.u. [Ber85] or the increased value based on systematics in heavier neighbouring isotopes. The second possible configuration (oblate $4p-2h$ intruder) would mean a change compared to heavier isotopes, where $\pi[h^2_{9/2}]$ 8^+ states are populated by $E3$ transitions. However, we may still anticipate the increased B($E3$) value due to suggestion that the $E3$ strength enhancement in Pb and Po isotopes is caused by an oblate deformation [Dra05; Dra01]. In contrast, our value of 2(1) W.u. (or 0.6(3) W.u. when branching ratio equal to relative intensity from Table 5.7 is considered) corresponds to values of standard spin-flip $E3$ transitions in [Ber85]. Therefore it does not follow the interpretation from [Dra05; Dra01] and changes the trend compared to $^{200-196}$Po.

The 154 keV ($E1$) transition in ^{192}Po has very low strength compared to heavier isotopes $^{208-204}$Po. However, $B(E1)$ values for more neutron deficient Po nuclei are not known and there is no established systematics. $E1$ transition strengths for neighbouring nuclides are known only in Pb isotopes, and our value for ^{192}Po is within the same order of magnitude (Fig. 5.18, Table 5.12).

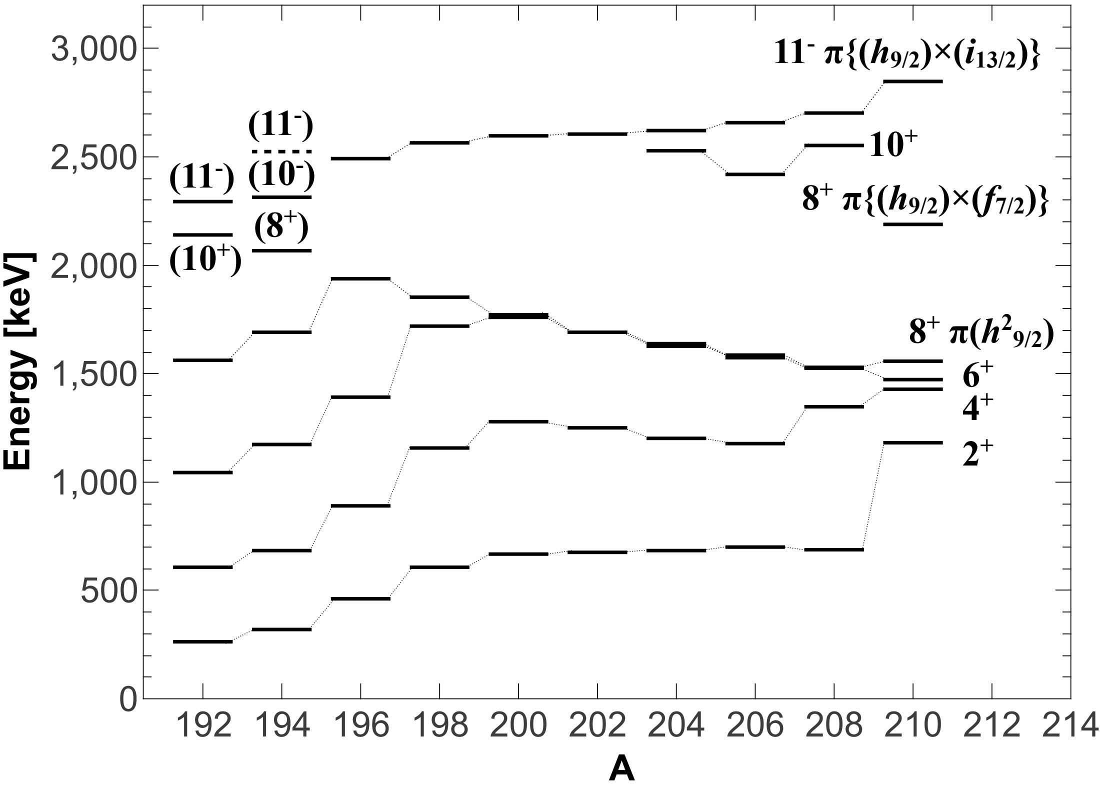

Figure 5.19: Systematics of 11^{-} isomeric levels and lower lying 8^{+}, 6^{+}, 4^{+} and 2^{+} levels in even-A Po isotopes. 10^{+} states are plotted too, if they are in decay path of the isomer. The (10^{-}) isomeric level in ^{194}Po is shown as well. For simplicity, only yrast levels are plotted for $I^{\pi} \leq 6^{+}$. Values for ^{192}Po and ^{194}Po are from this work. Dashed level denotes value of energy for (11^{-}) level in ^{194}Po from previous study [Hel99]. Remaining data are from references in Table 5.11.

Systematics of excitation energies of 11^{-} isomers alongside with 8^{+} and lower lying yrast levels in even-A neutron deficient Po isotopes is shown in Fig. 5.19. Energies of 11^{-} levels have a decreasing trend with decreasing neutron number. Only exception was the value for ^{194}Po from a previous study [Hel99], where de-excitation of the isomer via the 459 keV transition was proposed, yielding the excitation energy of 2525 keV. This was higher than the excitation energy of 2491 keV in ^{196}Po [Alb91] but we did not observe evidence for this or another 11^{-} isomeric level in ^{194}Po. We confirmed excitation energy of the isomer in ^{192}Po, therefore energies of remaining 11^{-} levels are decreasing monotonously.

5.4 Fine structure in the α decay of ^{192}Po and ^{194}Po

Fine structure in the α decay of ^{192}Po and ^{194}Po was already investigated in the past as a method for identification of low lying excited 0^+ states in ^{188}Pb and ^{190}Pb and thus study shape coexistence in these isotopes. One fine α-decay line of ^{192}Po with the energy of 6610(30) keV was identified in study at FMA (ANL) and assigned as a decay to an oblate 0^+ state [Bij96]. This line was confirmed in an experiment at the gas-filled separator RITU (JYFL) with more precise energy of 6613(7) keV [All98]. Moreover, another α-decay line with 6418(13) keV was identified and suggested to decay to prolate 0^+ state in ^{188}Pb. However, more recent study performed at SHIP deduced that the 6418(13) keV peak stems from α decay of ^{193}Po [Vel03]. The ~ 6.6 MeV α-decay line was confirmed with measured energy of 6591(8) keV and intensity of 1.5(3) %.

The α decay of ^{194}Po with the energy of 6191(7) keV to the excited 0^+ state in ^{190}Pb was established in measurement performed at the LISOL facility (Leuven Isotope Separator On-Line) [Dup85]. The energy of this line was more recently measured at the same facility to be 6194 keV and its intensity was determined to be 0.22 % [Wau94].

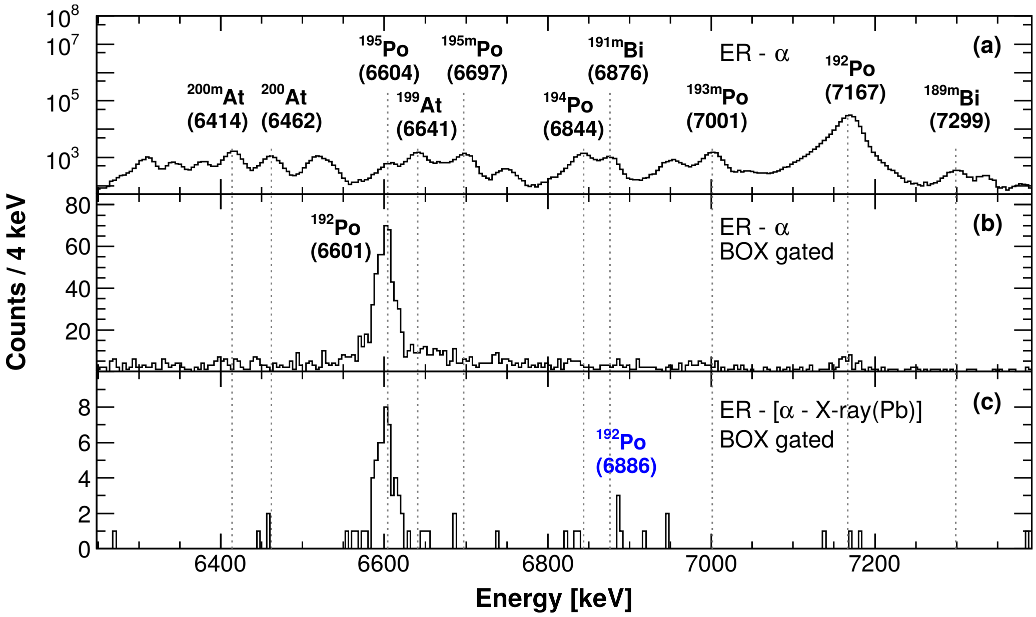

Figure 5.20: Fine structure in α decay of ^{192}Po. Panel a): α spectrum from ER-α correlations; panel b): α spectrum from ER-α correlations, with required coincidence between α and CE registered in BOX detectors; panel c): α spectrum from ER-[α-x ray(Pb)] correlations, with required coincidence between α and CE registered in BOX detectors.

To search for another transition in the fine structure of ^{192}Po α decay, we used combined data from R199 and R224. Since fine structure α decays lead to daughter nucleus in an excited state, de-excitation via internal conversion may take place, which is accompanied by emission of conversion electrons (CE) and x rays. In the case the state in daughter nucleus is the lowest excited state and it has $I^\pi = 0^+$, it may de-excite only by emission of CE. When

CE is emitted in coincidence with α particle, depending on CE direction, its energy can be absorbed in the PSSD and summed with energy signal of α particle or it may escape from the PSSD and be registered in BOX detectors. Therefore, BOX detectors can be used for gating of ER-α correlations in search for fine structure in α decay. Moreover, a coincidence with x ray from daughter atom may be also required as a more strict condition.

The results of our investigation are presented in Fig. 5.20. In the top panel, all ER-α correlations from R199 + R224 are shown, time and position windows were the same as for γ-ray analysis. In the middle panel, there are ER-α correlations gated by BOX detectors, which means, that the signal from BOX detectors (presumed CE) was required in coincidence with α particle. The last panel presents ER-[α-x ray(Pb)] correlations gated by BOX detectors. The transition with energy of 6601 keV is present in both BOX gated spectra as expected. It has to be noted, that even if CE escapes the PSSD, part of its energy will be summed with energy of α particle. Thus we have to correct measured energy. In [Vel03], they determined minimum energy left in the PSSD by escaping CE to be 10 keV. Since we used the same detection set up and even added their data (R199) to ours (R224), we used this value as a correction to measured energy. For the same reasons, we used two other corrections from [Vel03]: CE detection efficiency of 35(5) % and the fact that the fine α-decay peak contains only 50(5) % of the intensity of that α transition. The rest of the intensity is hidden in the tail to higher energies, which is formed by α-CE summing. Taking all this into account, the energy of the line was deduced to be 6591(5) keV and the intensity relative to main α transition from ^{192}Po is 1.2(2) %, which is consistent with values from [Vel03]. With the given level of the background, upper limit of the intensity of unobserved another α transition is 0.06 % of the main α transition.

A weak line at energy 6886 keV appeared in the last panel, where the most strict conditions were applied. It may be an indication of a new transition in α decay of ^{192}Po. After correction for summing with CE energy, the energy of the new line would be 6876(7) keV. Background in this region is probably caused mostly by summing of α-particle energy and part of CE energy. If we take the range $(6650-7000)$ keV and assume that the background is distributed randomly, formation of such line as the one at 6886 keV will have the probability of ≈ 0.2 %. Intensity of this tentative line is 0.11(6) %, which is slightly above the detection limit for ER-(α-CE) correlations, but there is no clear indication of this line in corresponding spectrum (Fig. 5.20, panel (b)). Moreover, detection limit for ER-[α-CE-x ray(Pb)] correlations (panel (c)) is even higher and with a value of 0.18 % it is slightly above the intensity of the 6876(7) keV line (labelled 6886 keV in the figure), which makes the line rather speculative. The detection limit also shows, that this more strict condition is not suitable for search for new weak α transitions, although it clears up the spectrum. It has to be noted, that energy 6876 keV is the same as for the decay of ^{191m}Bi. However, this decay leads directly to the ground state of ^{187}Tl [Fir96], thus it has no simultaneous CEs or X-rays.

In the same way as in the case of ^{192}Po, we investigated also fine structure in the α decay

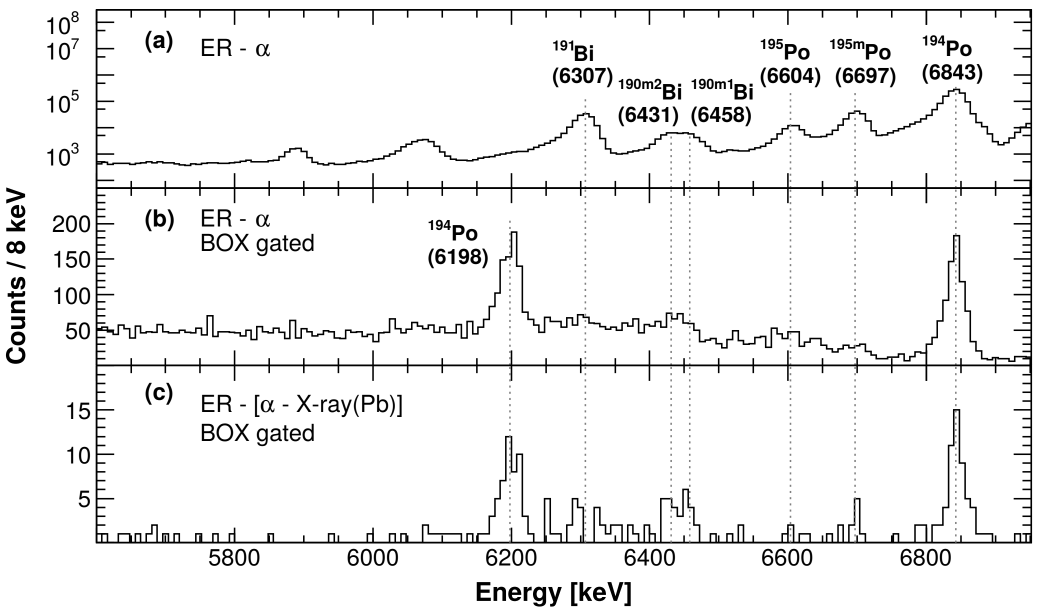

Figure 5.21: Fine structure in α decay of ^{194}Po. Panel a): α spectrum from ER-α correlations; panel b): α spectrum from ER-α correlations, with required coincidence between α and CE registered in BOX detectors; panel c): α spectrum from ER-[α-x ray(Pb)] correlations, with required coincidence between α and CE registered in BOX detectors.

of ^{194}Po. Resulting spectra are shown in Fig. 5.21. The known fine α decay is clearly visible both in panel (b) and (c) with measured energy of 6198 keV, which after correction for summing with CEs would be 6188(5) keV. The intensity of 6188(5) keV line deduced from ER-(α-CE) correlations is 0.24(4) % of the main α transition in ^{194}Po, which is consistent with value 0.22 % from [Wau94]. Upper limit of the intensity of another unobserved α transition is 0.03 % of the main α transition. In panel (c), there are a few counts from relatively strong α lines of ^{195}Po, ^{195m}Po, ^{190m1}Bi and ^{190m2}Bi still present. The activity closer to fine α peak of ^{194}Po most likely includes summations of α decays from this line with CEs and background from ^{191}Bi. There is no indication of another fine α-decay transition of ^{194}Po.

5.5 Production Cross-Sections

Several beam energies (236, 242, 250, 259 and 273 MeV) were used for the measurement with production reaction $^{56}Fe + ^{141}Pr \longrightarrow ^{197}At^{*}$, which allowed us to evaluate dependences of cross-sections on the excitation energy of compound nucleus (CN) - excitation functions. For planning of new experiments, it is crucial to know the excitation function, so that optimal reaction and beam energy can be chosen to achieve sufficient production of studied nuclei. If no experimental data for the specific reaction are available, the excitation function can be estimated using for example statistical model code calculations. To improve the accuracy of such calculations, experimental data for similar reactions are important.

We determined cross-sections for the respective products in *xn* and *pxn* channels for reac-

Table 5.13: Production cross-sections via *xn* channels for several excitation energies of CN in reaction $^{56}Fe + {}^{141}Pr \longrightarrow {}^{197}At^*$. Excitation energies were calculated for the beam energy in the middle of the target.

E^*_{CN} [MeV]	$\sigma(^{194m1}\mathrm{At})$ [nb]	$\sigma(^{194m2}\mathrm{At})$ [nb]	$\sigma(^{194m1,m2}\mathrm{At})$ [nb]	$\sigma(^{195g}\mathrm{At})$ [nb]	$\sigma(^{195m}\mathrm{At})$ [nb]	$\sigma(^{195m,g}\mathrm{At})$ [nb]
24	-	-	-	36(15)	91(42)	130(50)
28	12(7)	7(5)	19(9)	86(25)	180(60)	260(80)
34	79(23)	100(40)	180(50)	48(13)	81(23)	130(30)
40	360(100)	440(160)	800(240)	12(3)	26(7)	38(10)
50	91(23)	90(23)	180(50)	-	2.7(13)	2.7(13)

Table 5.14: Production cross-sections via *pxn* channels for several excitation energies of CN in reaction $^{56}Fe + {}^{141}Pr \longrightarrow {}^{197}At^*$. Excitation energies were calculated for the beam energy in the middle of the target.

E^*_{CN} [MeV]	$\sigma(^{193g}\mathrm{Po})$ [μb]	$\sigma(^{193m}\mathrm{Po})$ [μb]	$\sigma(^{193m,g}\mathrm{Po})$ [μb]	$\sigma(^{194}\mathrm{Po})$ [μb]	$\sigma(^{195g}\mathrm{Po})$ [μb]	$\sigma(^{195m}\mathrm{Po})$ [μb]	$\sigma(^{195m,g}\mathrm{Po})$ [μb]
24	-	-	-	0.35(9)	0.34(9)	0.71(18)	1.1(3)
28	-	-	-	0.54(14)	1.7(4)	2.7(7)	4.4(11)
34	0.027(11)	0.15(4)	0.18(5)	5.6(15)	6.8(17)	9.8(25)	17(4)
40	0.24(6)	0.42(11)	0.66(17)	20(5)	2.7(7)	4.1(10)	6.9(17)
50	1.8(5)	3.2(8)	5.0(13)	6.6(17)	0.10(2)	0.10(2)	0.19(5)

tion mentioned above, using ER-α or ER-α-α correlations corrected for detection efficiency, branching ratios, half-lives and transmission through the separator. The latter one was estimated to be 40(10) % for this projectile-target mass ratio [Maz08]. For ^{194}At, ^{195}At, ^{193}Po and ^{195}Po, separate cross-sections of ground states and isomeric states or of two isomeric states were determined as well as total cross-sections of the isotopes. All resulting cross-sections are listed in Table 5.13 (*xn* channels) and Table 5.14 (*pxn* channels). Excitation energies of compound nuclei were calculated for the beam energy in the middle of the target. Energy losses of the beam in the target were determined using kinematics calculator included in the program LISE++ [LISE]. Due to vicinity of the proton drip-line and thus low proton separation energies, *pxn* evaporation channels are significantly stronger than corresponding (x + 1) neutron channels. The cross-sections for isotopes with two states are shown in Fig. 5.22, where excitation functions are plotted separately for each state and also total cross-sections for both states are plotted. No significant changes in relative production of these states are visible along respective excitation functions.

We compared experimental values with calculations performed with the statistical model code HIVAP [Rei92; Rei81]. We used two different modes. The first mode involves fusion barrier approximated by a truncated Gaussian and employs fluctuations of the barrier, which enables to estimate sub-barrier fusion. The second mode involves simple fusion barrier approximated by an inverted parabola without barrier fluctuations and strongly suppresses sub-

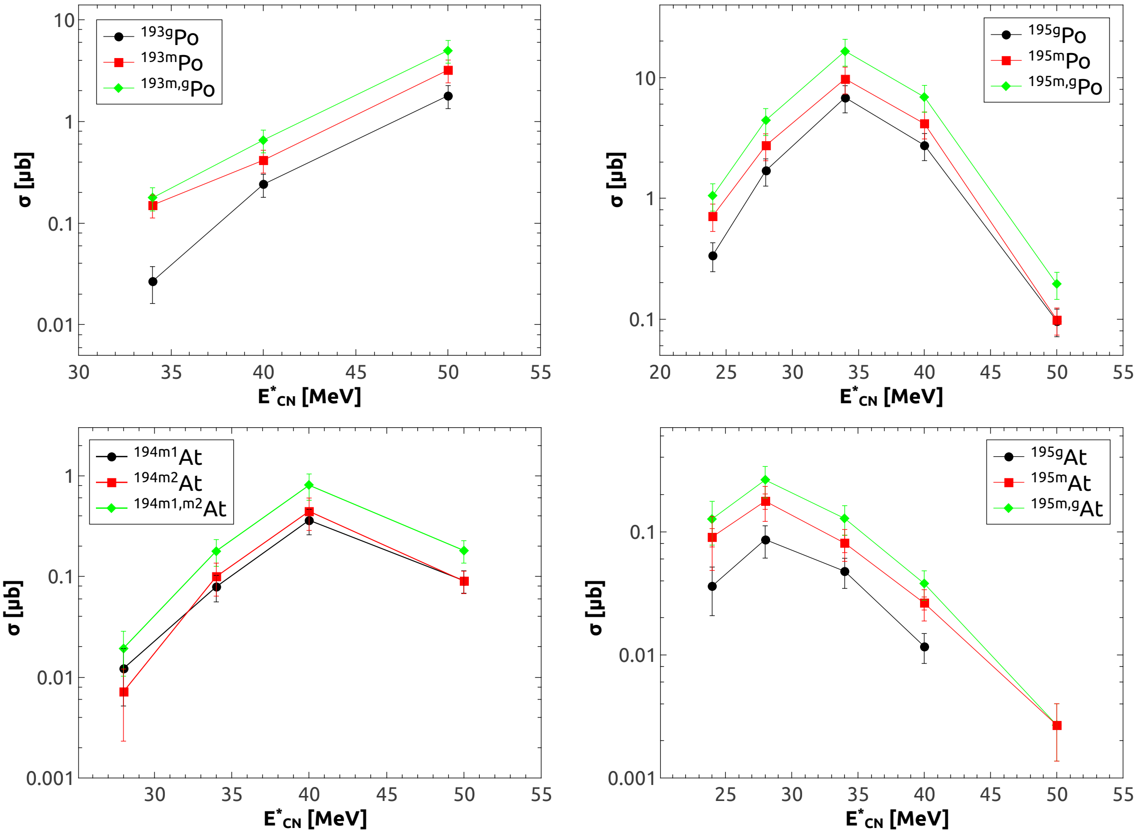

Figure 5.22: Production cross-sections via *xn* and *pxn* channels for several excitation energies of CN in reaction $^{56}Fe + {}^{141}Pr \longrightarrow {}^{197}At^{*}$ for isotopes with two states. Separate excitation functions for each state and for total production are plotted.

barrier fusion. The ratio of fission to neutron-emission reaction channels was set to $a_f/a_n = 1$ and similarly to study [And05] we controlled the strength of the fission channel only by scaling parameter C_f for theoretical fission barrier of CN (see Eq. (2.19)). Deformation of the target nucleus was taken from [Mol95] and other parameters were set to usual values tested in similar reactions [Ant].

To determine the proper value of C_f, we compared experimental values with HIVAP calculations using several different values of C_f (Fig. 5.23). Calculations were performed in the mode with fusion barrier fluctuations. We chose $C_f = 0.69$ as the best option based on the comparison, which also agrees with systematics from [And05]. The systematics was established in a study of Po and Bi cross-sections. For Bi or Po compound nuclei with $A = 197$ it requires $C_f \approx 0.70$, which is close to our value for the compound nucleus ^{197}At.

With the value of $C_f = 0.69$, we also performed HIVAP calculations for the mode with simple fusion barrier approximated by inverted parabola. Comparison of both types of calculations with experimental values for *xn* and *pxn* channels separately is shown in Fig. 5.24. We can see that $2n$ channel is only partially suppressed by the fusion barrier, since experimental points are closer to calculation with barrier fluctuations. The suppression of $3n$ channel is even weaker. In the case of *pxn* channels, suppression by the fusion barrier is weak

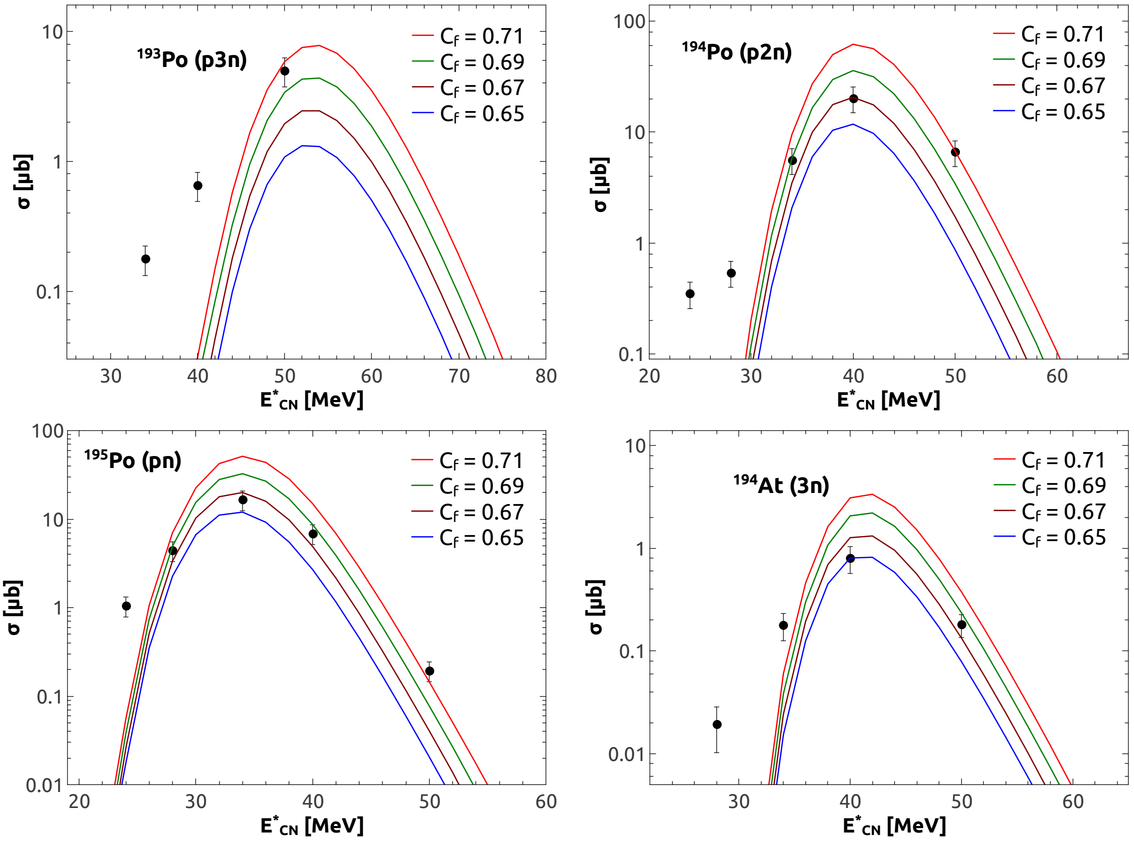

Figure 5.23: Comparison of experimental cross-sections (points) and HIVAP calculations using fusion barrier fluctuations for different values of theoretical fission barrier scaling parameter C_f (lines).

for both *pn* and *p*2*n* channels. Experimental excitation functions are broader than calculated functions, which may be affected by non-zero target thickness and beam energy distribution around set value.

For the reaction $^{51}V + {}^{144}Sm \longrightarrow {}^{195}At^{*}$, in which ^{192}Po was produced, only one beam energy of 235 MeV was used. Moreover, two targets of different thickness were employed, yielding different production cross-sections for ^{192}Po. The cross-sections were 1.6(4) μb and 0.5(1) μb for the target thickness 301 μg/cm^2 and 546 μg/cm^2, respectively. The values correspond to somewhat different excitation energies due to unequal target thickness and thus different beam energy in the middle of the target. For the thicker target, it was 40.0 MeV while for the thinner target it was 41.3 MeV. Comparison of experimental points with HIVAP calculations using barrier fluctuations for several values of C_f is shown in left panel of Fig. 5.25. It seems that there were problems with the quality of the thicker target or with settings of the experiment during measurement with this target, because the excitation energy is closer to optimum, but cross-section is lower than in the case of the thinner target. Since we had only one reliable experimental point, we took a value of $C_f = 0.68$ deduced from systematics [And05] for comparison in right panel of Fig 5.25. It shows experimental points and HIVAP calculations with the fusion barrier fluctuations mode and with the mode for fusion

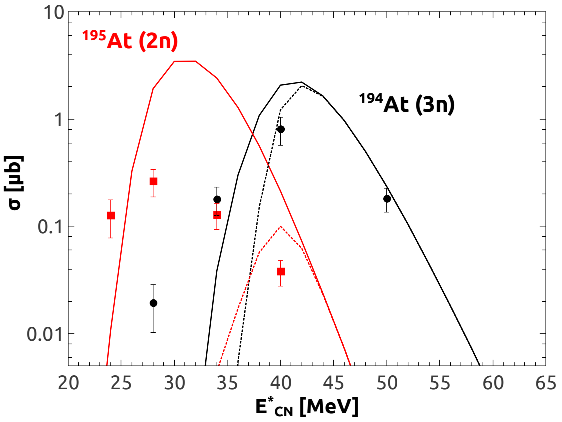

Figure 5.24: Cross sections of *xn* and *pxn* channels of the reaction $^{56}Fe + ^{141}Pr \longrightarrow {}^{197}At^{*}$ as functions of excitation energy of the compound nucleus. Experimental values are denoted by points. Lines represent HIVAP calculations of excitation functions using $C_f = 0.69$. Solid lines are for the mode with barrier fluctuations, dashed lines are for the mode with simple fusion barrier approximated by an inverted parabola.

barrier approximated by inverted parabola, as in the case of the former reaction. The experimental point for the thinner target is roughly a factor of two lower than HIVAP calculation, which is still reasonably close for cross-section estimates. The point for the thicker target is almost a factor of 6 lower than the calculation. Therefore also based on this comparison, we regard only point for the thinner target as reliable.

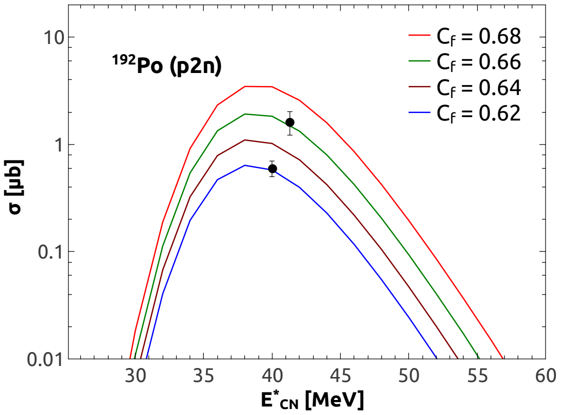

Figure 5.25: Cross sections of ^{192}Po in the reaction $^{51}V + {}^{144}Sm \longrightarrow {}^{195}At^{*}$ for two targets of different thickness, the point with higher excitation energy is for the thinner target. Left figure shows HIVAP calculations with the fusion barrier fluctuation mode for different values of C_f, right figure shows comparison of the two modes of HIVAP calculations for $C_f = 0.68$. Experimental values are denoted by points. Solid lines represent calculations for the mode with barrier fluctuations, dashed lines are for the mode with simple fusion barrier approximated by an inverted parabola.

Summary

In this thesis, we present decay-spectroscopy studies of neutron-deficient polonium isotopes ^{192}Po and ^{194}Po and cross-sections evaluation including neighbouring astatine and polonium isotopes. Investigated nuclei are from the region of neutron-deficient isotopes near proton closed shell $Z = 82$, where various interesting phenomena can be studied as for example β-delayed fission, shape coexistence or nuclear isomers.

Main objective of the thesis was γ-ray spectroscopy of short-lived isomers reported in ^{192,194}Po. Only limited information on these isomers was available before. However, they were expected to be members of long chain of 11^- isomeric states present in even-A Po isotopes from ^{210}Po to ^{196}Po. These 11^- isomers have dominant configuration of $\pi\{(h_{9/2}) \otimes (i_{13/2})\}$ and decay mostly via $E3$ transitions to 8^+ states. Transition strengths of these decays exhibit unexpected increase with decreasing neutron number. Additional objective was to investigate fine structure in α decay of studied isotopes.

Second objective was cross-sections evaluation for Po and At isotopes produced in our measurements and comparison of these experimental cross-sections with calculations performed using statistical model code HIVAP. Cross-sections systematics is important for planning of new experiments in this region, since as we are getting closer to proton drip-line, production cross-sections are decreasing rapidly.

The isotopes were studied at the velocity filter SHIP in GSI, Darmstadt (Germany). They were produced in fusion-evaporation reactions $^{56}Fe + ^{141}Pr$ and $^{51}V + ^{144}Sm$. Targets were mounted on a rotating wheel, which rotated with frequency synchronized to pulsed structure of the projectile beam provided by the accelerator UNILAC. Evaporation residues (ERs) were separated from the primary beam by the SHIP and implanted into the system of silicon detectors combined with the germanium clover detector.

We employed time and position correlation method to identify events of interest. We registered approximately 1.6 million of ^{194}Po α decays correlated to implantations of ERs using PSSD + BOX detectors. To select γ rays from the isomer, we required coincidences between these ERs and γ rays within $\approx 5\,\mu$s, which is the time interval of hardware coincidences of the detection system. Our statistics of γ rays originating in decays of the isomer was approximately $10\times$ higher than in previous measurements [Hel99]. We observed all γ transitions previously reported for the isomer and attributed four new γ transitions with energies 209, 248, 362 and 494 keV to its decay. We deduced the half-life of the isomer to be 12.9(5) μs, which is consistent with previous value of 15(2) μs [Hel99], but more precise.

Due to the collected statistics, we were able to study γ-γ coincidences for this isomer for the first time. We confirmed previous decay scheme with the exception of the 459 keV ($E3$) transition de-exciting the isomeric level with tentative (11^-) assignment [Hel99]. We replaced this transition by the new 248 keV transition. Moreover, we determined upper limit of K-conversion coefficient of the 248 keV transition to be 2.3(4) while gating with an "OR" condition on the 319, 366, 462, 545 and 373 keV transitions in γ-γ coincidence analysis. Comparison with theoretical K-conversion coefficients reveals $M2$ multipolarity of the transition, which yields unexpected $I^\pi = (10^-)$ for the isomeric level instead of $I^\pi = (11^-)$. This assignment is in contrast with known systematics and require further detailed investigation in future measurements. However, the results presented in this Thesis represent the limit of currently achievable experimental data.

In addition, we observed also transitions from the side-band up to 9^- level, which were previously registered only in in-beam studies [Hel99]. Their presence in our focal-plane detection system means that the levels from the side band have to be populated by the decay of an isomeric state. Possible explanations may be unobserved ≈ 33 keV transition from isomeric (10^-) state to 9^- level or another isomer above the 9^- state.

We analysed the data for ^{192}Po in the same way. In total, approximately 110 000 ER-α(^{192}Po) time and position correlations were registered with the PSSD + BOX detectors. Again, we selected γ rays from the isomer by requiring coincidences within ≈ 5 μs with ERs correlated to ^{192}Po α decays. Collected statistics was roughly two times higher than in previous measurement [Vel03]. We observed all previously reported transitions from the isomer and attributed 14 more γ transitions to its decay, namely the *377*, 422, 625, 652, 660, 686, 720, 733, *835*, 966, *1096*, *1172*, *1231* and *1258* keV transitions. Tentative transitions are written in italic.

In order to perform γ-γ coincidence analysis, we combined our new data with data from previous study [Vel03], which was also performed at the SHIP. As a result, observed γ-γ coincidences also for this isomer for the first time. We confirmed formerly established ground-state band [Hel99] up to the (10^+) level and the suggestion from [Vel03] that the 154 keV transition de-excites the (11^-) isomeric level to the (10^+) state. We suggested also a parallel de-excitation by the new 733 keV ($E3$) transition to the (8^+) level (mainly based on energy balance, however, there was also a hint in γ-γ coincidences while gating on subsequent transitions).

Supported by intensity balance and γ-γ coincidences, we proposed a side feeding of the (4^+) level by the 445 keV transition and tentatively placed also the 363 keV transition into a cascade with it. Thus we established two levels from the side band with tentative assignments (4^+_2) and (6^+_2) based on analogous (4^+_2) and (6^+_2) levels present in ^{194}Po [Hel99] and (4^+_2) level in ^{196}Po [Alb91].

Concerning the systematics of 11^- isomers in even-A polonium isotopes, we observed only (10^-) isomer in ^{194}Po mentioned above and no evidence of another isomer with I^π = 11^-. Nevertheless, we evaluated what would be the $B(E3)$ value if the isomer had an assignment of 11^- and the de-exciting 248 keV transition had $E3$ multipolarity. The result was unrealistic value above 100 W.u. However, we cannot argue that the 11^- isomer systematics ends here, because our measurement supported the (11^-) assignment for the short-lived isomer in ^{192}Po. The newly identified 733 keV ($E3$) transition de-exciting the isomer in ^{192}Po yields $B(E3) = 2(1)$ W.u. Therefore it exhibits a significant drop of transition strength compared to $^{196-200}$Po, where increasing transition strengths were observed with decreasing neutron number up to 25(3) and 24(4) W.u. in ^{198}Po and ^{196}Po, respectively [Maj90; Alb91]. This might a hint of change in the configuration of the (8^+) state populated by the de-excitation of the isomer or the change of the nuclear shape.

For both isotopes ^{192}Po and ^{194}Po we investigated also a fine structure in the α decay. We employed ER-α correlations with α particles registered only in the PSSD and gated by conversion electrons (low energy events up to 1 MeV) registered in BOX detectors. Also a more strict condition was examined, where additional coincidences with x rays from daughter atom (Pb) were required. However, this condition proved to be less sensitive due to relatively low efficiency of γ ray detection. Previously-known fine α line of ^{194}Po [Wau94] was observed with the energy of 6188(5) keV and an upper limit for another unobserved fine α line was determined to be 0.03 % of the intensity of the main $\alpha(^{194}\text{Po})$ transition. For ^{192}Po also a known fine α transition [Vel03] was identified with the energy of 6591(5) keV and a hint of a new fine α transition with the energy of 6876(7) keV was observed. However, it was visible only with the more strict condition requiring x rays, where the detection limit was 0.18 % of the main $\alpha(^{192}\text{Po})$ transition and the intensity of the tentative line was only 0.11(6) %. It was not observed in ER-(α-conversion electron) correlations, where the detection limit was lower with the value of 0.06 %.

We evaluated excitation functions of isotopes $^{193-195}$Po and ^{194,195}At produced in reaction $^{56}Fe + ^{141}Pr \longrightarrow ^{197}At^*$. Results were compared with calculations performed using statistical model code HIVAP. Reduction of theoretical fission barrier of compound nucleus needed in HIVAP calculation was consistent with systematics established in [And05] for Po and Bi compound nuclei in this mass region. For the reaction ^{51}V + ^{144}Sm, we used only one beam energy and thus we could not determine excitation functions. Nevertheless, we evaluated cross-section for ^{192}Po and again compared the result with HIVAP calculations.

Zhrnutie

V tejto práci prezentujeme štúdium neutrónovo deficitných izotopov polónia ^{192}Po a ^{194}Po metódami rozpadovej spektroskopie, a vyhodnotenie ich účinných prierezov produkcie ako aj účinných prierezov pre susedné izotopy polónia a astátu. Skúmané jadrá patria do oblasti neutrónovo deficitných izotopov z blízkosti uzavretej protónovej vrstvy $Z = 82$, kde je možné študovať viaceré zaujímavé javy, ako napríklad oneskorené štiepenie po β premene, tvarovú koexistenciu alebo jadrové izoméry.

Hlavným cieľom práce bola γ spektroskopia krátkožijúcich izomérov v ^{192,194}Po, o ktorých boli doposiaľ známe iba obmedzené informácie. Predpokladalo sa však, že patria do dlhého radu 11^- izomérov nachádzajúcich sa v izotopoch Po s párnym A od ^{210}Po po ^{196}Po. Tieto 11^- izoméry majú dominantnú konfiguráciu $\pi\{(h_{9/2}) \otimes (i_{13/2})\}$ [Hel99] a de-excitujú prevažne $E3$ prechodmi na 8^+ stavy. Sily týchto prechodov vykazujú nečakaný nárast s klesajúcim neutrónovým číslom [Maj90; Alb91]. Doplnkovým cieľom bolo štúdium jemnej štruktúry α premeny skúmaných izotopov.

Druhým cieľom bolo vyhodnotenie účinných prierezov produkcie izotopov Po a At, ktoré boli produkované v našich meraniach a porovnanie týchto hodnôt s výpočtami uskutočnenými v kóde HIVAP založenom na štatistickom modeli. Systematika účinných prierezov je dôležitá pre plánovanie budúcich experimentov v tejto oblasti, obzvlášť kvôli rapídnemu poklesu účinných prierezov s približovaním sa k protónovému driplinu.

Experiment bol uskutočnený na rýchlostnom filtri SHIP v GSI, Darmstadt (Nemecko). Študované izotopy boli produkované vo fúzno výparných reakciách $^{56}Fe + {}^{141}Pr$ a $^{51}V + {}^{144}Sm$. Terče boli umiestené na rotačnom kolese, ktoré sa otáčalo synchronizovane s pulznou štruktúrou zväzku projektilov poskytovaných urýchľovačom UNILAC. Produkty fúznych reakcií (PR) boli oddelené od primárneho zväzku separátorom SHIP a implantované do polohovo citlivého 16 stripového kremíkového detektora PSSD. Okolo tohto detektora bolo paralelne so smerom zväzku umiestnených ďalších 6 stripových kremíkových detektorov, ktoré tvorili tzv. BOX detektor. Jeho úlohou bolo registrovať častice uniknuté z PSSD ako sú α častce, konverzné elektróny alebo štiepne fragmenty. Na detekciu γ alebo roňtgenovských kvánt bol tesne za PSSD umiestnený germániový detektor pozostávajúci zo 4 samostatných kryštálov.

Na identifikáciu želaných eventov sme využili časovú a polohovú korelačnú metódu. Pomocou zostavy PSSD a BOX detektorov sme identifikovali približne 1.6 milióna α premien

^{194}Po, ktoré boli korelované s implantáciou PR do PSSD. Časové okno bolo približne tri doby polpremeny ^{194}Po a poloha korelovaných signálov sa mohla líšiť nanajvýš o 0.6 mm. Na vyselektovanie γ kvánt pochádzajúcich z izoméru v ^{194}Po sme vyžadovali koincidencie medzi korelovanými PR a γ kvantami vrámci intervalu $\approx 5\,\mu$s, pričom tento interval predstavuje hardvérové koincidencie detekčného systému. Počet zaregistrovaných γ kvánt z tohto izoméru bol približne 10 krát vyšší než v predošlom meraní [Hel99]. Pozorovali sme všetky γ prechody známe pre jeho de-excitáciu a priradili mu štyri nové γ prechody s energiami 209, 248, 362 a 494 keV. Určili sme polčas rozpadu izoméru $T_{1/2} = 12.9(5)\,\mu$s, čo je konzistentné s hodnotou z predošlej štúdie $T_{1/2} = 15(2)\,\mu$s [Hel99], ale zároveň presnejšie.

Vďaka štatistike nahromadenej počas merania sme mohli po prvý krát pre tento izomér študovať γ-γ koincidencie. Potvrdili sme predošlú rozpadovú schému s výnimkou ($E3$) prechodu s energiou 459 keV, ktorý bol navrhnutý v [Hel99] ako prechod de-excitujúci izomér s predbežne priradeným spinom a paritou (11^-). Tento prechod sme nahradili novým prechodom s energiou 248 keV. Pomocou γ-γ koincidenčnej analýzy, kde sme použitím "ALEBO" podmienky získali koincidencie s prechodmi s energiami 319, 366, 462, 545 a 373 keV, sme určili horný limit K konverzného koeficientu pre prechod s energiou 248 keV. Porovnanie s teoretickými K konverznými koeficientami určuje pre 248 keV prechod multipolaritu $M2$, čo znamená nečakanú zmenu spinu izoméru na $I^\pi = (10^-)$ namiesto $I^\pi = (11^-)$. Toto priradenie spinu je v kontraste so známou systematikou izomérov v izotopoch Po a vyžaduje detailné štúdium v budúcich experimentoch. Výsledky prezentované v tejto práci sú však získané z experimentálnych dát, ktoré sú na hranici toho čo je možné v súčasnosti dosiahnuť.

Zároveň sme pozorovali γ prechody z bočného pásu až po 9^- level, ktoré boli predtým registrované iba v in-beam meraní [Hel99]. To, že ich bolo možné pozorovať v koncových detektoroch za separátorom znamená, že bočný pás musí byť napájaný rozpadom izoméru. Možným vysvetlením je prechod s energiou ≈ 33 keV z (10^-) izoméru na 9^- stav alebo ďalší, nepozorovaný izomér, nachádzajúci sa nad 9^- stavom.

Rovnakým spôsobom ako v prípade ^{194}Po sme analyzovali aj dáta pre ^{192}Po. Celkovo sme pomocou PSSD a BOX detektorov zaznamenali približne 110 000 PR-α(^{192}Po) časových a polohových korelácií, kde časové okno bolo 4 doby polpremeny ^{192}Po a maximálny rozdiel v polohe 0.7 mm. Pre γ kvantá z izoméru sme opäť vyžadovali koincidencie s korelovanými PR vrámci $\approx 5\,\mu$s. Nahromadená štatistika bola približne dvakrát väčšia ako v predošlom meraní [Vel03]. Pozorovali sme všetky známe γ prechody pre daný izomér a priradili sme mu 14 nových prechodov s energiami *377*, 422, 625, 652, 660, 686, 720, 733, *835*, 966, *1096*, *1172*, *1231* a *1258* keV. Kurzívou sú napísané γ prechody, ktoré sú priradené predbežne.

Pre účely γ-γ koincidenčnej analýzy sme spojili naše nové dáta s dátami z predošlého merania, ktoré bolo tiež uskutočnené na seprátore SHIP [Vel03]. Aj pre tento izomér sme tak po prvý krát pozorovali γ-γ koincidencie. Potvrdili sme známu schému pre pás základného stavu [Hel99] až po (10^+) ako aj návrh z [Vel03], že prechod s energiou 154 keV de-excituje izomérny stav (11^-) na (10^+) hladinu. Navyše sme navrhli paralelnú de-excitáciu izoméru pomocou 733 keV prechodu na (8^+) stav (najmä na základe súladu energií, avšak aj v γ-γ koincidenciách sme pozorovali náznak v spoločnom spektre pre nadväzujúce prechody).

Na základe γ-γ koincidencií a súladu relatívnych intenzít sme navrhli bočné napájanie pásu základného stavu na (4^+) hladinu prechodom s energiou 445 keV. Predbežne sme do kaskády s ním priradili aj prechod s energiou 363 keV. Týmto boli vytvorené dve hladiny bočného pásu, ktorým sme dali predbežné priradenia spinov a parít (4^+_2) a (6^+_2) na základe analogických stavov (4^+_2) a (6^+_2) v ^{194}Po [Hel99] a (4^+_2) stavu v ^{196}Po [Alb91].

V spojitosti so systematikou 11^- izomérov v izotopoch Po s párnym A, pre ^{194}Po sme pozorovali iba vyššie diskutovaný (10^-) izomérny stav a nezaregistrovali sme žiadny dôkaz pre prípadný ďalší izomér s $I^\pi = 11^-$. Vyhodnotili sme však silu prechodu $B(E3)$ pre 248 keV prechod, ako keby pozorovaný izomér mal $I^\pi = 11^-$. Výsledkom bola nerealistická hodnota nad 100 W.u. Nie je však možné tvrdiť, že by tým končila séria 11^- izomérov, pretože pre krátkožijúci izomér v ^{192}Po naše meranie podporuje priradenie (11^-). Nový prechod s energiou 733 keV, ktorý de-excituje izomér v ^{192}Po má $B(E3) = 2(1)$ W.u. To predstavuje nečakaný pokles oproti silám $E3$ prechodov v $^{196-200}$Po, kde boli pozorované stúpajúce $B(E3)$ hodnoty s klesajúcim netrónovým číslom izotopu až po 25(3) a 24(4) W.u. v ^{198}Po a ^{196}Po [Maj90; Alb91]. Tento pokles môže naznačovať zmenu konfigurácie (8^+) stavu, ktorý je napájaný daným ($E3$) prechodom alebo zmenu tvaru jadra.

Pre oba izotopy, ^{192}Po a ^{194}Po, sme študovali aj jemnú štruktúru α premeny. Využili sme PR-α korelácie, kde α častica bola registrovaná s plnou energiou v PSSD a zároveň bola vyžadovaná koincidencia (vrámci $\approx 5\,\mu$s) s konverzným elektrónom (event s energiou do 1 MeV) zaregistrovaným v BOX detektore. Testované bolo aj využitie prísnejšej podmienky, kde α častica musela byť zároveň v koincidencii aj s röntgenovským kvantom z dcérskeho atómu (Pb). Vzhľadom na relatívne malú účinnosť detekcie γ kvánt v porovnaní s elektrónmi sa však táto metóda ukázala ako menej citlivá. Známy α prechod z jemnej štruktúry α premeny v ^{194}Po [Wau94] sme potvrdili a pozorovali s energiou 6188(5) keV. Pre potenciálny ďalší α prechod sme určili horný limit 0.03 % z intenzity hlavného α prechodu v ^{194}Po. Pre ^{192}Po sme tiež potvrdili známy α prechod z jemnej štruktúry [Vel03] a namerali sme preň energiu 6591(5) keV. Zároveň sme pozorovali náznak ďalšej jemnej α čiary s energiou 6876(7) keV. Avšak viditeľný bol iba pri použití koincidencií s röntgenovskými kvantami, kde bol detekčný limit 0.18 % hlavného α prechodu v ^{192}Po a pozorovaný náznak mal intenzitu iba 0.11(6) %. V prípade korelačnej podmienky PR-(α-konverzný elektrón) tento prechod pozorovaný nebol, hoci detekčný limit bol nižší, s hodnotou 0.06 %.

Vyhodnotili sme excitačné funkcie pre izotopy $^{193-195}$Po a ^{194,195}At produkované v reakcii $^{56}Fe + {}^{141}Pr \longrightarrow {}^{197}At^*$. Výsledky sme porovnali s výpočtami s použitím kódu HIVAP vychádzajúceho zo štatistického modelu. Na správnu reprodukciu excitačných funkcií bola potrebná redukcia teoretickej štiepnej bariéry v HIVAPe, pričom toto zníženie bolo konzistentné so systematikou zostavenou pre reakcie vedúce na zložené jadrá Po a Bi s podobným hmotnostným číslom [And05]. Pre reakciu $^{51}V+^{144}Sm$ bola použitá iba jedna energia zväzku, preto nebolo možné zostaviť excitačné funkcie. Vyhodnotili sme však účinný prierez produkcie ^{192}Po a opäť porovnali s výpočtami v HIVAPe.

Appendix A

Analysis Code for the New Detection System at SHIP

Testing of the new detection system MoDSS (Mobile Decay Spectroscopy Set-up) was one of other projects in which I was involved during my PhD study. The system is primarily developed as a replacement of the old detection system at SHIP (GSI). However, it is designed as a compact and mobile system and it can be used also at experiments in other institutes. I joined several test measurements performed in GANIL at separator LISE and at SHIP. During these measurements, only rather preliminary analysis code was available. Missing implementation of correlation procedure, which could run "online" was one the most important drawbacks. Moreover, offline correlation procedure was dealt with only in a limited way as an external ROOT macro. Online analysis and possibility to perform fast, more detailed preliminary analyses, is important for effective operation of the experiment. Therefore an improvement of the analysis code and implementation of correlation procedure from the code for the old SHIP detection system was needed.

A.1 Detection System and Electronics

High flexibility and mobility of the system was achieved by using small chamber for silicon detectors and by employing very compact digital data acquisition system. Overall layout of the detectors is similar to the old set-up, but with several important differences. Instead of the PSSD, a double sided silicon strip detector (DSSD) was chosen as a main focal plane detector. It has thickness of $300\,\mu$m and sensitive surface of $60\times60\,\mathrm{mm}^2$. Both sides of the DSSD are divided into 60 strips, front strips are perpendicular to strips on the back side. Advantage of the DSSD over the PSSD is the fact, that both positions, horizontal and vertical, are determined by strip numbers. As a result, ballistic[1] and position calibrations are not needed any more. Similarly to the old set-up, the DSSD is surrounded by the BOX

---

[1] Position sensitivity of the PSSD is achieved by using a resistive layer, which causes signal dependence on the position along the strip and needs to be corrected by ballistic calibration. More details are in Section 4.1.

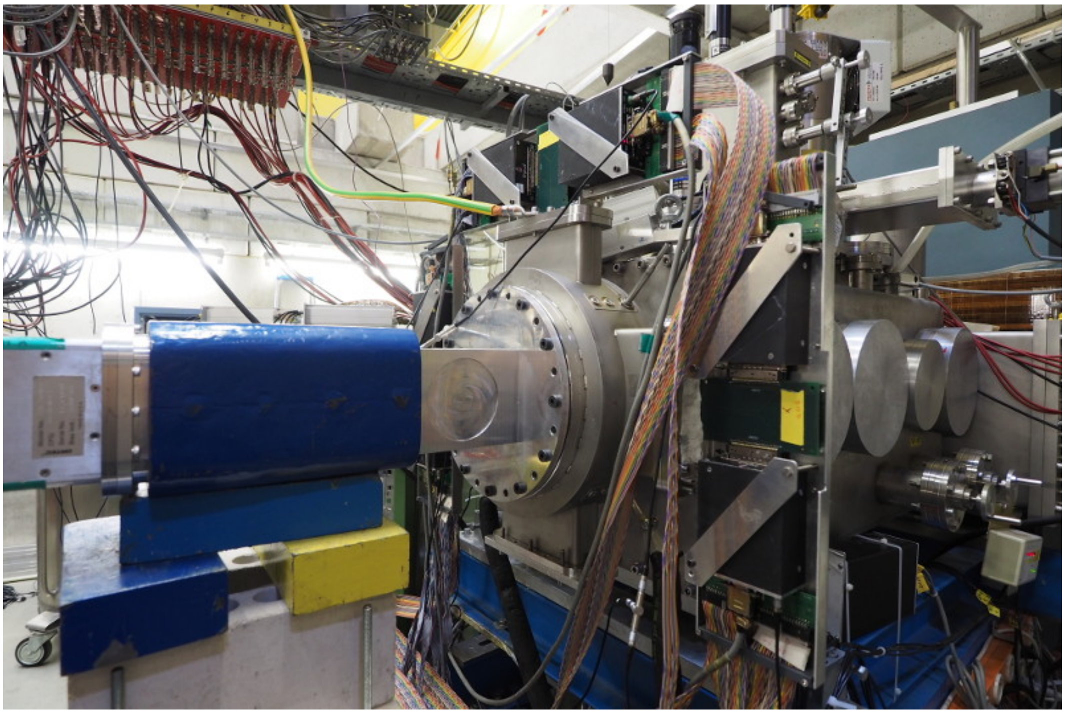

Figure A.1: MoDSS attached to the end of the SHIP beamline. Detector chamber is the part with circular shaped area (aluminium window). Blue segment to the left from the chamber is a shielding of the Ge-clover detector.

system in upstream direction. The BOX consists of 4 identical silicon strip detectors with total number of 32 independent segments. The assembly of silicon detectors is placed in a small chamber with dimensions of $\sim\ 7 \times 7 \times 8$ cm (Fig. A.1). Each side of the chamber, except the open side facing the beamline, has a thin aluminium window of 1.5 mm thickness in order to minimize shielding of emitted γ rays, which are detected outside of the chamber. The chamber is mounted on a flange with short piece of a vacuum pipe that can be connected into the beamline. Four vacuum feedthroughs for silicon detectors are incorporated into the piece of vacuum pipe. Germanium detectors may be placed close to aluminium windows to detect γ rays. To achieve high granularity for γ-γ coincidences and high detection efficiency, five Ge-clover detectors could be mounted around the chamber in ideal case, one placed to each window.

Although an analogue DAQ system was used in early stages of MoDSS development and still can be optionally used, the set-up relies on digital electronics under normal conditions. Output of charge-sensitive preamplifiers is sent to flash ADC modules FEBEX3A (Front End Board with optical link EXtension, Fig. A.2). The whole signal evolution (trace) is recorded with 50 MHz sampling frequency, that is with 20 ns sample time. Traces are analysed by FPGA modules built into FEBEX cards to obtain time and energy information. Since the whole trace is stored, pulse-shape analysis can be performed later if needed. Each FEBEX module can simultaneously process data from 16 independent detectors or detector strips. Data then flow from FEBEX cards to Multi-Branch System (MBS) [Bar00], which builds

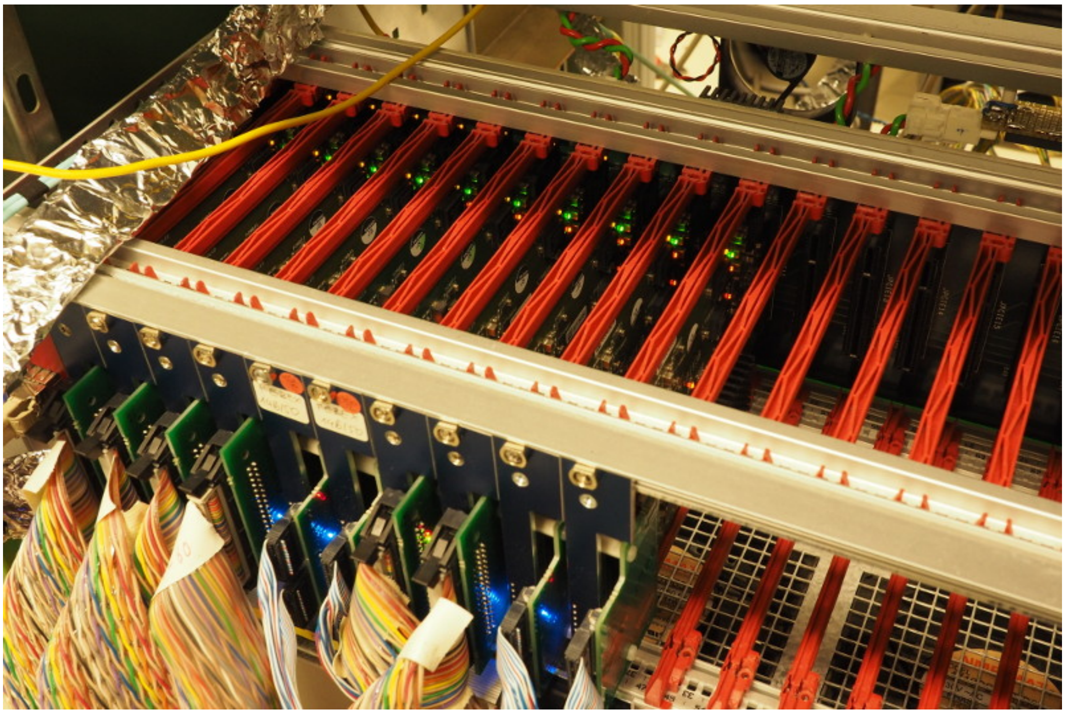

Figure A.2: FEBEX modules in operation.

events and streams them to data files stored on hard drive and to online analysis in Go4 system [Go4] (if the online analysis is running). Go4 is object-oriented analysis framework based on ROOT [ROOT] analysis system. An event is a set of all information from all detectors within a given time window after one of the detectors was triggered. For instance, when α decay occurs in one strip of the DSSD, a trace is recorded for a specific time and during this time, also traces from all other detectors are recorded. The time depends on the settings, usually 1024 samples are taken per a trace, which results in time of 20.48 μs.

A.2 Analysis Code

Go4 enables division of the analysis code into subsequent steps. Output of one step serves as an input of the next step. Go4 also provides basic templates of classes and functions from which the code needs to be developed in order to use its features and functionalities. The analysis code for the old set-up (I will refer to it further as the SHIP Analysis) was divided into three steps: Unpack, Analysis and Correl (Correlations). Once the code is divided into steps, one can choose during launch of the analysis which step will be actually running (for example, output of the Unpack step may be stored into root-file, and then the Analysis step may be fed from the root-file instead of directly from the Unpack). Events are sent from one step to the next as objects of class XXXXEvent, where XXXX stands for the step, which creates this event as output. Scheme of this process is shown in Fig. A.3. The same approach was taken for the new code (which will be further referred to as the MoDSS Analysis).

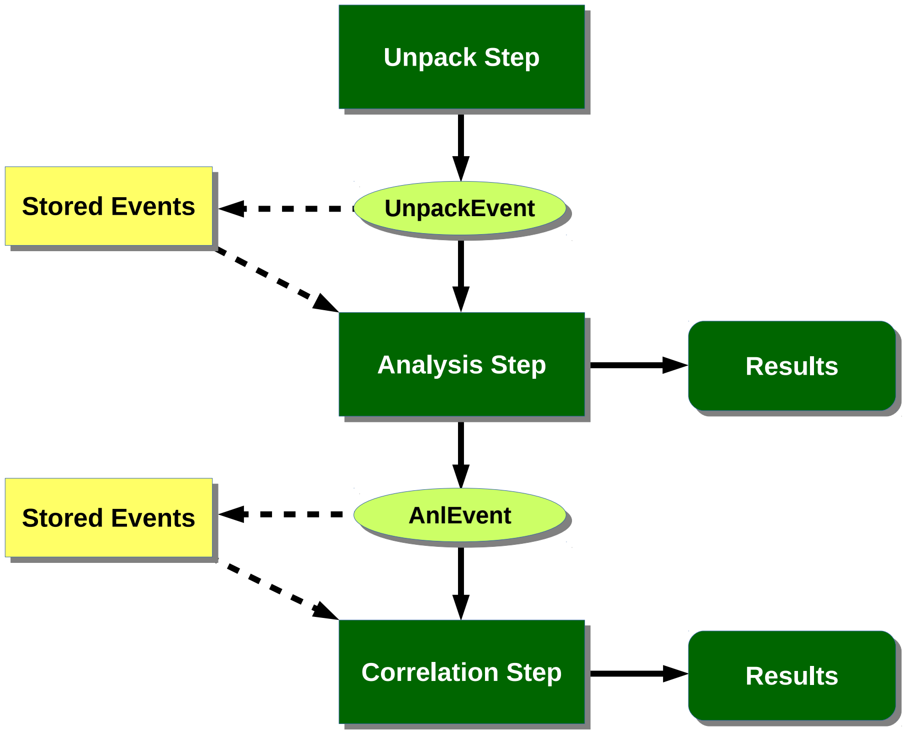

Figure A.3: Scheme of the analysis process. Unpack and Analysis steps may store their output events into files. Analysis and Correlations steps may afterwards take input events either from previous step or from these files. User decides which step/steps will run and what will be used as an input.

Concerning the new set-up, it is particularly useful to be able to store events from previous step. The digital electronics produces large amounts of data (hundreds of GB per day) by recording whole traces. Therefore the Unpack step, which runs through raw data, is significantly slowing down the analysis. The Correlation step, or even the Analysis step, needs to be run repeatedly during detailed offline data analysis while changing various parameters. Using the stored Unpack events, instead of running Unpack step each time, can greatly speed up the analysis process ($\approx 20\times$). Moreover, stored events take up much less disk space ($\approx 220\times$) and thus are more portable.

A.2.1 Analysis Step

Output event from the Unpack step has key variables, energy and time, in form of a three dimensional array: l_E[1][12][16] and hit_time[1][12][16]. The numbers stand for the size of each dimension. First dimension stands for the number of the crate, second dimension stands for the number of FEBEX module and the last one stands for the number of FEBEX channel. This structure of variables was in preliminary MoDSS Analysis only slightly simplified by removing first dimension, since only one crate was used. Resulting two dimensional arrays were used throughout the code, which lead to many doubly nested loops and confusing design. Moreover, if the specific detector was moved from for example module 1 to module 2, this had to be changed everywhere in the Analysis part. Therefore, one of the first changes I did was introduction of different variables and proper implementation of MapHardware() function. In this function, output event from the Unpack is taken as an input event and its member variables are assigned to local variables of the Analysis part. New variables are now divided based on a detector which they represent, e.g. EnonCalX[60] holds uncalibrated energies from 60 strips of one side of the DSSD, EnonCalGam[4] stores uncalibrated energies from 4 crystals of the Ge-clover detector etc. Naming convention was established, that the front side of the DSSD is called X and strip numbers are called X positions or IDX (identifier X),while back side is called Y and strip numbers are called Y positions or IDY (identifier Y).

By proper implementation of MapHardware() function it is meant, that it takes care of any change in the input event. Every experiment with different arrangement of modules will have its own "if" case and specific strip or clover crystal will be filled to the same local variable every time. No change elsewhere in the code is needed so far the same set of detectors is used. Due to changes mentioned above, the code could be significantly simplified and became easier to understand and maintain.

The SHIP Analysis used parameters stored in text files in order to enable setting of various parameters without need of re-compiling the code. Reading from the specific input file, writing to the file and some additional functions are defined in dedicated source and header files. Only calibration parameters were implemented in preliminary MoDSS Analysis. I included additional parameter files from the SHIP Analysis and enabled parameters that are relevant also for the new system.

Next step was implementation of add-back procedure for BOX detectors as well as calibration graphs for these detectors (calibration graphs are produced in the same way as in the SHIP Analysis, which is described in Section 4.3). Moreover, structure of sub-folders holding histograms and histogram names were modified in order to become more comprehensible.

The length of one event in the old set-up was $\approx 5\,\mu$s. This time increased in the new set-up to $20.48\,\mu$s (for trace containing 1024 samples), thus I included time window for prompt coincidences. I put settings for low and high value of this window into parameter file and it is applied on α-γ coincidences in the Analysis part and on α-γ and γ-γ coincidences in the Correlation part. Position of the prompt peak can be deduced from time distribution of α-γ coincidences, example is in Fig. A.4. It has to be noted, that time distribution of α-γ coincidences within one event is wider than $20.48\,\mu$s. The reason is that the values are time differences between signals from DSSD and Ge-clover detector, each of them can have time from the range $(0\,-\,20.48)\,\mu$s. Thus, resulting distribution has limits $\pm\,20.48\,\mu$s. In the case of the BOX detector, implementation of similar window does not seem to be necessary, as 99.76 % of DSSD-BOX coincidences were within the prompt peak.

As a preparation for implementation of the Correlation step, AnlEvent (output of the Analysis step) was defined in corresponding source and header files and filling of its variables

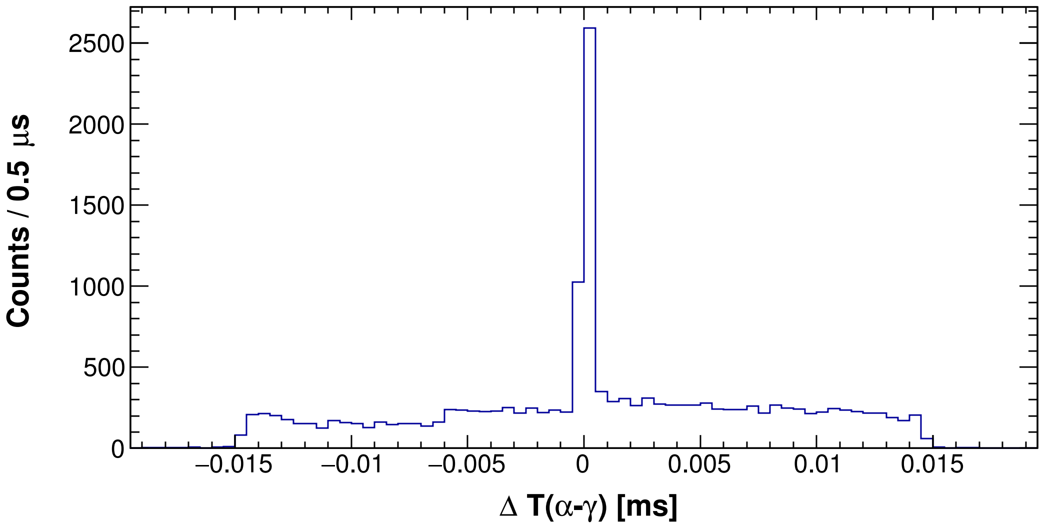

Figure A.4: Time differences between γ rays and α decays within one event. Prompt peak is between -0.5 and 1 μs.

was added to Analysis part. For one event, energy only from one strip is sent from the X side and one from the Y side of the DSSD. If there are more strips with signal during one event, the strip with highest energy is chosen. I tested possible loss of events due to this selection on data from the test measurement performed in October 2015 at GSI. It has to be noted, that during this experiment, only 1/10 of the beam intensity was available most of the time. During pause between beam pulses, only 0.6 % of events had signal in two or more strips of the X side. Moreover, almost all of the events with second highest energy had energies lower than 4 MeV, that is, outside of the energy range of α particles. More complicated situation was during the beam pulses. Over 60 % of the events had signals in two or more strips of the X side. Most of the signals during beam pulses come from scattered projectiles or target nuclei and cause high background. It is very often possible to distinguish these events from ERs on the plot of the energy versus time of flight. In the SHIP Analysis, there was a possibility to apply polygonal condition, that is, to create polygonal window on this plot and only events inside the window would be taken, example of the plot and condition from the MoDSS Analysis is shown in Fig. A.5. These conditions were available in the Correlation step and for high-energy branch also in Analysis step. In the MoDSS Analysis, these conditions were implemented in similar way into Correlation step and also into Analysis step as constraint on the output event in order to minimize loss of true events due to signals in multiple strips caused by the background.

A.2.2 Correlation Step

The Correlation step of the MoDSS Analysis is based on the Correlation step of the SHIP Analysis, since it was rather well written. Naturally, differences between the two set-ups

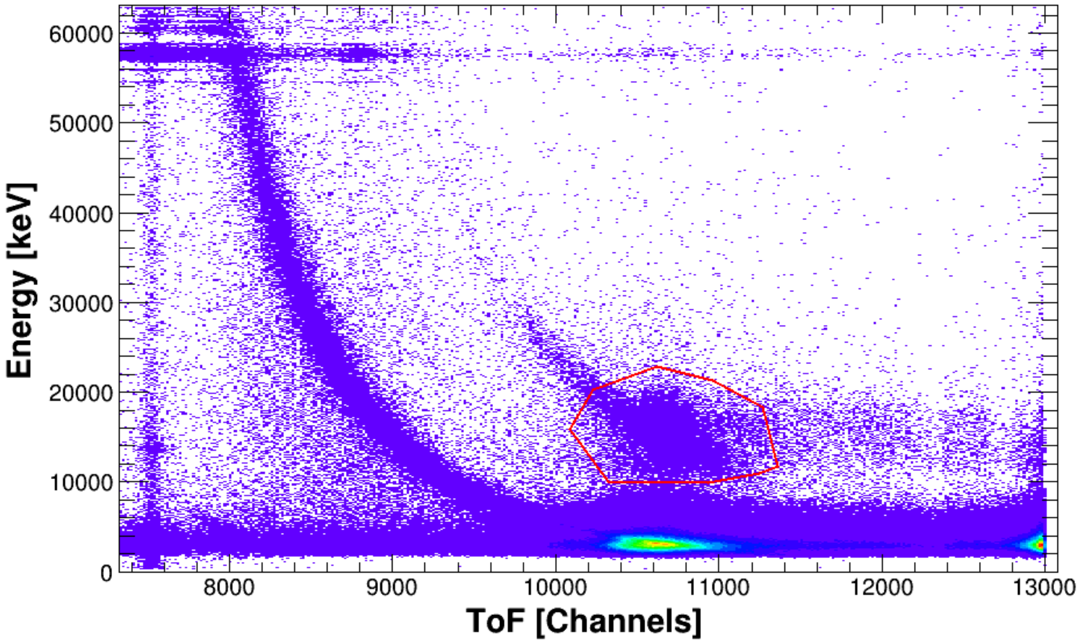

Figure A.5: Energy versus time of flight spectrum from the Y side of the DSSD. Red line shows the example of the polygonal condition.

required many modifications. Most important differences between the set-ups from the point of view of correlations are two sides of the main silicon detector instead of one, the absence of high-energy branch of the electronics and different determination of positions. The old set-up identified position of an event by strip number and vertical position along the strip in mm or channels. The new set-up has strips on both sides of the detector and thus the position is determined by number of the front strip and number of the back strip. Relatively complicated functions dealing with positions along strips could be removed and replaced by newly defined TestPositions function shown in Fig. A.6, which also simplified conditions on positions. The fact that high-energy branch is missing, but now there are two sides of the detector, made to some extent possible to re-use some features designed for the high-energy branch.

```
Bool_t MoDSSCorrelProc::TestPositions(Int_t IDX1, Int_t IDY1, Int_t IDX2, Int_t IDY2)
{
  if ((fCorrelPar->fbTopOrBot) && (((IDX1 == IDX2) && (IDX1 != 0)) ||
  ((IDY1 == IDY2) && (IDY1 != 0)))) return kTRUE;
  else if ((fCorrelPar->fbTopAndBot) && ((IDX1 == IDX2) && (IDY1 == IDY2)) &&
  ((IDX1 != 0) && (IDY1 != 0))) return kTRUE;
  else if ((fCorrelPar->fbOnlyTop) && (IDX1 == IDX2) && (IDX1 != 0)) return kTRUE;
  else if ((fCorrelPar->fbOnlyBot) && (IDY1 == IDY2) && (IDY1 != 0)) return kTRUE;
  else return kFALSE;
}
```

Figure A.6: TestPositions function. It takes strip numbers from mother and daughter event and compares them according to chosen position parameter: either both positions had to be the same, or only front (X), or only back (Y), or either one of them. Old names of correlation parameters are still used, top now stands for IDX and bottom stands for IDY.

All pairs of correlation search from the SHIP Analysis were implemented, specifically recoil-α, α-α, recoil-γ, α-γ, γ-α, γ-γ, recoil-fission, α-fission and γ-fission. They can be further combined by choosing proper parameters, e.g. as recoil-α-α, recoil-γ-α, α-α-fission correlations. Search for γ-γ is done only in such combinations, where the first γ is preceded by recoil or α. It is possible to search for multiple α generations in case of recoil-α and α-α correlations.

Correlations involving fission were implemented only in a limited way, since there is not a high energy branch of the electronics in the new set-up. However, the front side of the DSSD has better energy resolution than the back side and will be primarily used for α-energy range. The back side is not as suitable for α spectroscopy and may be used with a bit lower amplification. Thus, a larger energy range is achieved for the cost of even worse resolution. For example, during the test run in October 2015, the energy range of the back side was up to $\approx 59\,\mathrm{MeV}$. Higher-energy events are present at the end of the spectrum as pile-up and thus we cannot obtain proper energy information for most of the fission events. Nevertheless, it is at least possible to determine that correlation chain ends most probably by fission using pile-up at the end of back side's energy range.

The SHIP Analysis has an interactive user GUI (Graphical User Interface) for changing correlation parameters. The same user GUI was used also in the MoDSS Analysis with a few changes reflecting differences in the set-ups. Comparison of the two user GUIs is shown in Fig. A.7. Printing of correlated events to screen and/or file was implemented as well.

As was mentioned above, the X side of the DSSD has better resolution than the Y side. Therefore, low energy correlations (electrons, α particles) use energies only from X side of the DSSD and the Y side is used only to get position information. However, there was added also a possibility for α particles to use Y energy in case the energy from X side is missing. When this option is activated, the correlation search still uses X energies, but if the X energy is missing, the energy from Y side is checked. This option would be needed if some of the strips from the X side stopped working. Naturally, the X positions would be missing as well and position condition "IDX and IDY" could not be used.

In total, new MoDSS Analysis consists of 17 header files, 15 source files, 4 calibration files, 4 parameter files and a Makefile. The user GUI consists of additional 4 header files, 3 source files, 3 Qt designer files, a Makefile and a Module.mk file.

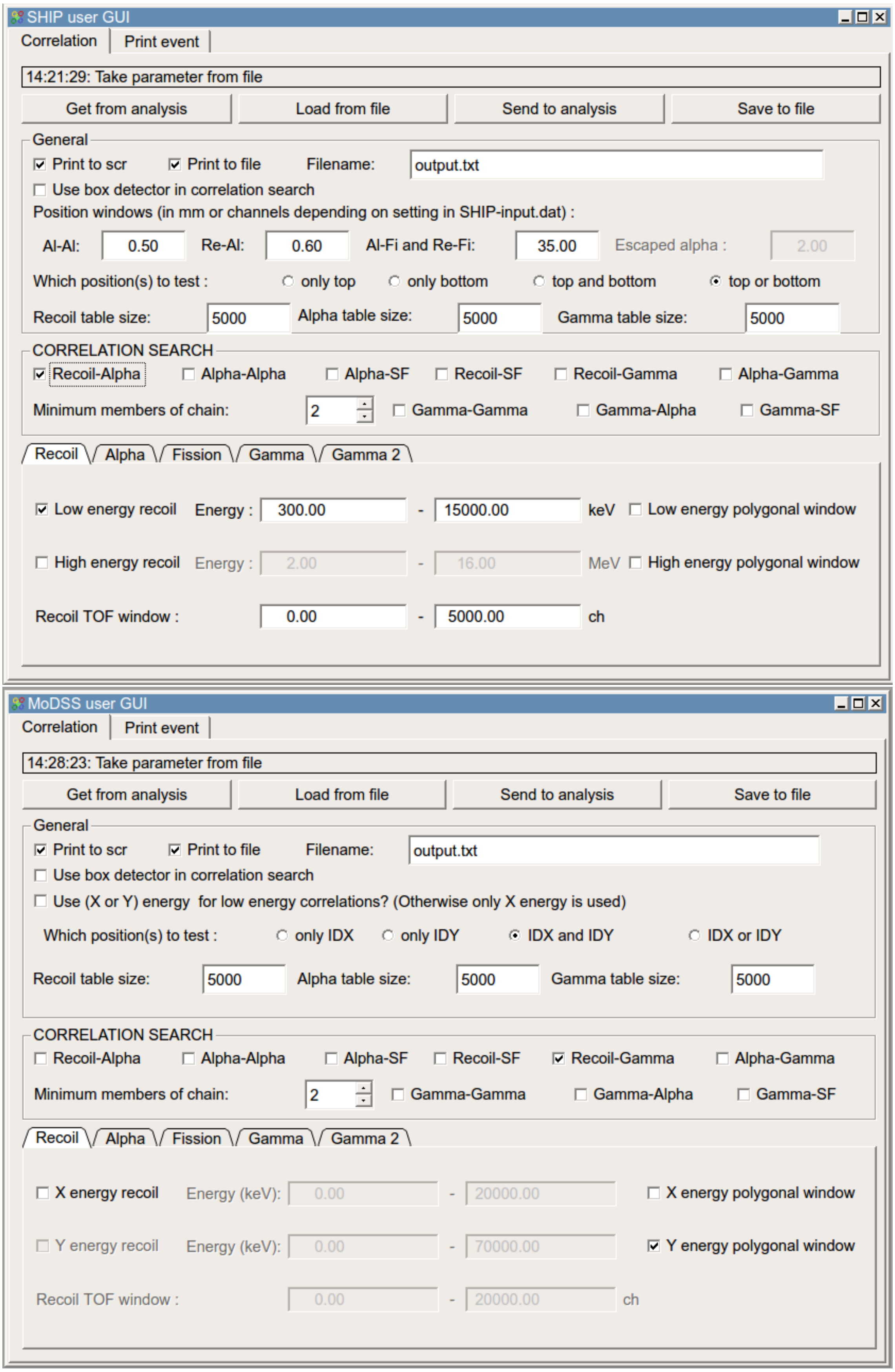

14:21:29: Take parameter from file

General

☑ Print to scr ☑ Print to file Filename: output.txt

☐ Use box detector in correlation search

Position windows (in mm or channels depending on setting in SHIP-input.dat) :

Al-Al: 0.50 Re-Al: 0.60 Al-Fi and Re-Fi: 35.00 Escaped alpha : 2.00

Which position(s) to test : ○ only top ○ only bottom ○ top and bottom ● top or bottom

Recoil table size: 5000 Alpha table size: 5000 Gamma table size: 5000

CORRELATION SEARCH

☑ Recoil-Alpha ☐ Alpha-Alpha ☐ Alpha-SF ☐ Recoil-SF ☐ Recoil-Gamma ☐ Alpha-Gamma

Minimum members of chain: 2 ☐ Gamma-Gamma ☐ Gamma-Alpha ☐ Gamma-SF

☑ Low energy recoil Energy : 300.00 - 15000.00 keV ☐ Low energy polygonal window

☐ High energy recoil Energy : 2.00 - 16.00 MeV ☐ High energy polygonal window

Recoil TOF window : 0.00 - 5000.00 ch

14:28:23: Take parameter from file

General

☑ Print to scr ☑ Print to file Filename: output.txt

☐ Use box detector in correlation search

☐ Use (X or Y) energy for low energy correlations? (Otherwise only X energy is used)

Which position(s) to test : ○ only IDX ○ only IDY ● IDX and IDY ○ IDX or IDY

Recoil table size: 5000 Alpha table size: 5000 Gamma table size: 5000

CORRELATION SEARCH

☐ Recoil-Alpha ☐ Alpha-Alpha ☐ Alpha-SF ☐ Recoil-SF ☑ Recoil-Gamma ☐ Alpha-Gamma

Minimum members of chain: 2 ☐ Gamma-Gamma ☐ Gamma-Alpha ☐ Gamma-SF

☐ X energy recoil Energy (keV): 0.00 - 20000.00 ☐ X energy polygonal window

☐ Y energy recoil Energy (keV): 0.00 - 70000.00 ☑ Y energy polygonal window

Recoil TOF window : 0.00 - 20000.00 ch

Figure A.7: Comparison of the user GUI from the SHIP Analysis (top) and from the MoDSS Analysis (bottom).

A.3 Test of the code on data with production of ^{253}No

As it was mentioned already above, we performed a measurement with MoDSS system in October 2015 at SHIP. To test the new code, I used data from this measurement for reaction $^{48}Ca + ^{207}Pb \longrightarrow ^{253}No + 2n$. Also Figs A.4 and A.5 in earlier Section A.2.1 were produced from the same data. Spectrum of α particles from the measurement is shown in Fig. A.8.

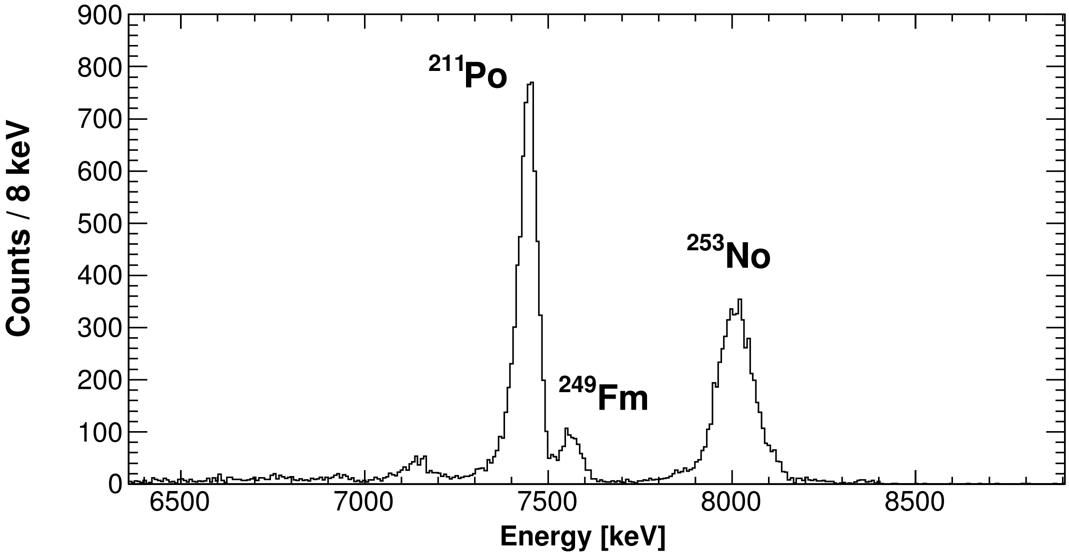

Figure A.8: Alpha particles registered in pauses between beam pulses.

Important feature of the correlation search taken from the SHIP Analysis is a possibility to search for multiple mother events. If there is more possible mother events during chosen time window, all of them (up to a specified number, usually 5) are found. This is significant for two reasons: first, if the real mother is not the first one found, it is not lost and second, a more realistic account for the background is achieved. Due to this feature, it was possible to determine decay curve of relatively long lived ^{253}No (top part of Fig. A.9). Even with long time window, the background could be reasonably estimated by a constant function. Correlation time was 700 s, number of possible mother events was up to 35 and there were no conditions on energy or time of flight of ERs. High granularity of the DSSD was additional factor that made the correlation search with so wide time window possible. Resulting half-life was 1.51(14) min, which is consistent with literature value of 1.62(15) min [NNDC]. Furthermore, severe reduction of the background can be achieved and longer correlation time can be used when polygonal condition on ERs in TOF versus energy plot is applied (top part of Fig. A.9). Correlation time was 1500 s and number of possible mother events was up to 10. The background was reduced more than $10\times$ and the deduced half-life of 1.58(7) min was more precise compared to the case without polygonal condition.

Although this data set was not suitable for search for long α-decay chains, it is possible to use random correlations to test the ability of Correlation step to do such search. I set

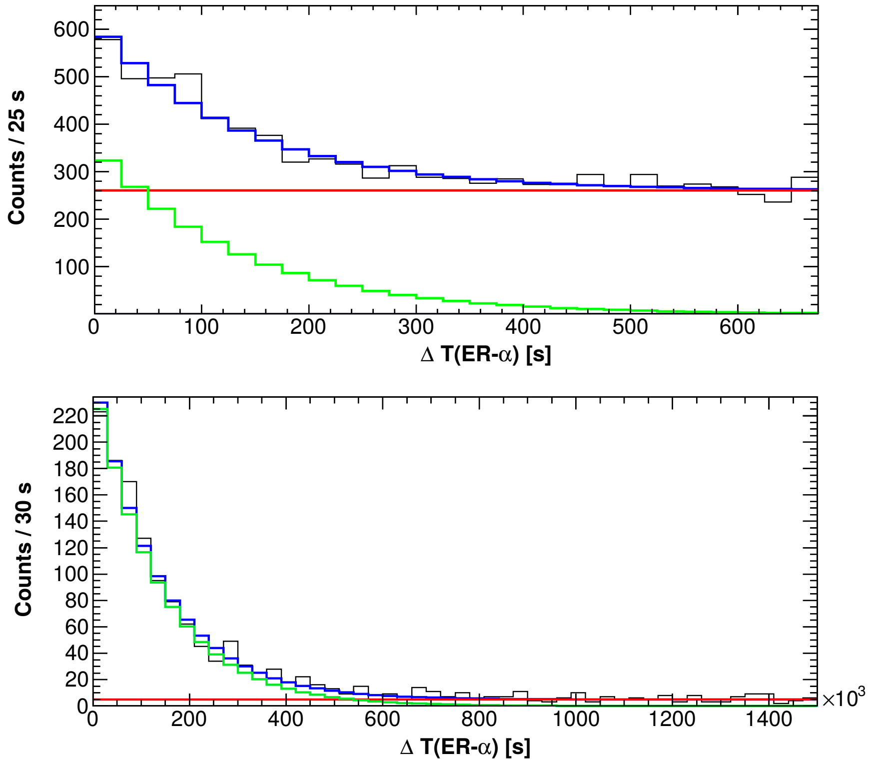

Figure A.9: Time distribution of ER-α(^{253}No) correlations. Blue line is a fit by an exponential function plus constant, green line is the exponential component of the fit and red line is the constant component of the fit. Top figure: No condition on energy or TOF of ERs was applied, number of possible mothers was up to 35. Bottom figure: Polygonal condition on time of flight versus energy distribution of ERs was applied in the Analysis step, number of possible mothers was up to 10.

wide energy and time windows in search for recoil-α-α-α-α correlations and the correlation method successfully found subsequent events at the same positions. Printout of two chains is shown in Fig. A.10.

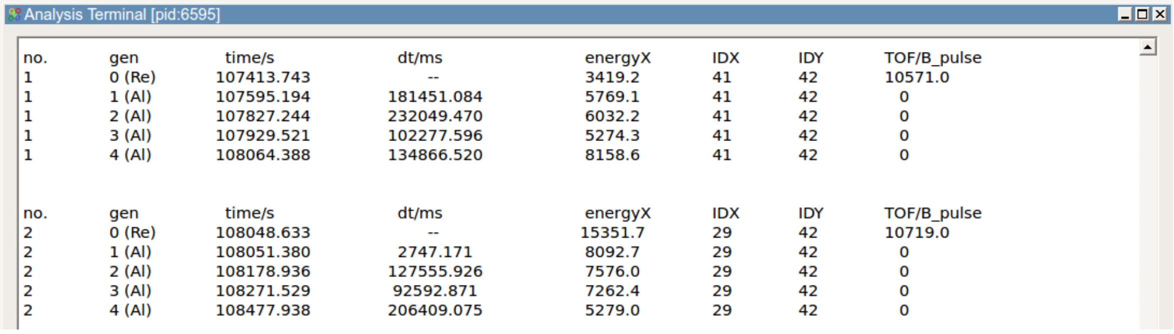

```
no.     gen      time/s        dt/ms         energyX   IDX   IDY   TOF/B_pulse
1       0 (Re)   107413.743       --         3419.2    41    42    10571.0
1       1 (Al)   107595.194    181451.084    5769.1    41    42      0
1       2 (Al)   107827.244    232049.470    6032.2    41    42      0
1       3 (Al)   107929.521    102277.596    5274.3    41    42      0
1       4 (Al)   108064.388    134866.520    8158.6    41    42      0

no.     gen      time/s        dt/ms         energyX   IDX   IDY   TOF/B_pulse
2       0 (Re)   108048.633       --         15351.7   29    42    10719.0
2       1 (Al)   108051.380      2747.171    8092.7    29    42      0
2       2 (Al)   108178.936    127555.926    7576.0    29    42      0
2       3 (Al)   108271.529     92592.871    7262.4    29    42      0
2       4 (Al)   108477.938    206409.075    5279.0    29    42      0
```

Figure A.10: Printout of two random recoil-α-α-α-α correlations to show the ability to search for multiple α generations.

References

[Alb91] D. Alber et al. In: *Z. Phys. A* 339 (1991), p. 225.
DOI: `10.1007/BF01284056`.

[All98] R. G. Allat et al. In: *Phys. Lett. B* 437 (1998), p. 29.
DOI: `10.1016/S0370-2693(98)00939-3`.

[And00] A. N. Andreyev et al. In: *Nature* 405 (2000), p. 430.
DOI: `10.1038/35013012`.

[And04] A. N. Andreyev et al. In: *Nucl. Instrum. Methods A* 533 (2004), p. 409.
DOI: `10.1016/j.nima.2004.07.204`.

[And05] A. N. Andreyev et al. In: *Phys. Rev. C* 72 (2005), p. 014612.
DOI: `10.1103/PhysRevC.72.014612`.

[And06] A. N. Andreyev et al. In: *Phys. Rev. C* 73 (2006), p. 024317.
DOI: `10.1103/PhysRevC.73.024317`.

[And09] A. N. Andreyev et al. In: *Phys. Rev. C* 79 (2009), p. 064320.
DOI: `10.1103/PhysRevC.79.064320`.

[And13a] A. N. Andreyev, M. Huyse, and P. Van Duppen. In: *Rev. Mod. Phys.* 85 (2013), p. 1541.
DOI: `10.1103/RevModPhys.85.1541`.

[And13b] A. N. Andreyev et al. In: *Phys. Rev. Lett.* 110 (2013), p. 242502.
DOI: `10.1103/PhysRevLett.110.242502`.

[And15] B. Andel. In: *AIP Conf. Proc.* 1681 (2015), p. 030012.
DOI: `10.1063/1.4932256`.

[And16] B. Andel et al., accepted to *Physical Review C* (2016).

[Ant] S. Antalic. *Private communication.*
W. Reisdorf. *HIVAP manual* (GSI, Darmstadt, unpublished).

[Ant04] S. Antalic et al. In: *Nucl. Instrum. Methods A* 530 (2004), p. 185.
DOI: `10.1016/j.nima.2004.04.217`.

[Ant05] S. Antalic. “Synthesis and properties of neutron deficient isotopes of elements around Z=100”. PhD thesis. Bratislava: FMFI UK, 2005.

[Ant08] S. Antalic et al. In: *Eur. Phys. J. A* 38 (2008), p. 219. DOI: `10.1140/epja/i2008-10665-7`.

[Ant11] S. Antalic et al. In: *Eur. Phys. J. A* 47 (2011), p. 62. DOI: `10.1140/epja/i2011-11062-y`.

[Ant15] S. Antalic et al. In: *Eur. Phys. J. A* 51 (2015), p. 41. DOI: `10.1140/epja/i2015-15041-0`.

[Bar00] R. Barth et al. *GSI Multi-Branch System User Manual*. Darmstadt: GSI, 2000.

[Bax90] A. M. Baxter et al. In: *Nucl. Phys. A* 515 (1990), p. 493. DOI: `10.1016/0375-9474(90)90595-D`.

[Ben84] C. Bengtsson et al. In: *Phys. Scr.* 30 (1984), p. 164. DOI: `10.1088/0031-8949/30/3/002`.

[Ber85] I. Bergström and B. Fant. In: *Phys. Scr.* 31 (1985), p. 26. DOI: `10.1088/0031-8949/31/1/005`.

[Ber95] L.A. Bernstein et al. In: *Phys. Rev. C* 52 (1995), p. 621. DOI: `10.1103/PhysRevC.52.621`.

[Beu76] H. Beuscher et al. In: *Phys. Rev. Lett.* 36 (1976), p. 1128. DOI: `10.1103/PhysRevLett.36.1128`.

[Bij96] N. Bijnens et al. In: *Z. Phys. A* 356 (1996), pp. 3–4. DOI: `10.1007/s002180050137`.

[BrIcc] *Conversion Coefficient Calculator*. `http://bricc.anu.edu.au/`. T. Kibédi et al. In: *Nucl. Instrum. Methods A* 589 (2008) p. 202. DOI: `10.1016/j.nima.2008.02.051`.

[Byr90] A. P. Byrne et al. In: *Phys. Rev. C* 42 (1990), R6. DOI: `10.1103/PhysRevC.42.R6`.

[Cas05] R. F. Casten. *Nuclear Structure from a Simple Perspective*. New York: Oxford University Press Inc., 2005. ISBN: 0-19-850724-0.

[Coc11] T. E. Cocolios et al. In: *Phys. Rev. Lett.* 106 (2011), p. 052503. DOI: `10.1103/PhysRevLett.106.052503`.

[Coh74] S. Cohen, F. Plasil, and W. J. Swiatecki. In: *Ann. Phys.* 82 (1974), p. 557. DOI: `10.1016/0003-4916(74)90126-2`.

[Dra01] G. D. Dracoulis et al. In: *Phys. Rev. C* 63 (2001), p. 061302. DOI: `10.1103/PhysRevC.63.061302`.

[Dra05] G. D. Dracoulis et al. In: *Phys. Rev. C* 72 (2005), p. 064319. DOI: `10.1103/PhysRevC.72.064319`.

[Dup00] P. Van Duppen and M. Huyse. In: *Hyperfine Interact.* 129 (2000), p. 149. DOI: `10.1023/A:1012649513990`.

[Dup85] P. Van Duppen et al. In: *Phys. Lett.* 154B (1985), p. 354. DOI: `10.1016/0370-2693(85)90408-3`.

[Dup91] P. Van Duppen et al. In: *Nucl. Phys. A* 529 (1991), p. 268. DOI: `10.1016/0375-9474(91)90796-9`.

[Fan71] B. Fant. In: *Phys. Scr.* 4 (1971), p. 175. DOI: `doi:10.1088/0031-8949/4/4-5/005`.

[Fan90] B. Fant, T. Weckström, and A. Källberg. In: *Phys. Scr.* 41 (1990), p. 652. DOI: `doi:10.1088/0031-8949/41/5/005`.

[Fir96] R. B. Firestone et al. *Table of Isotopes*. CD-ROM Edition, John Wiley & Sons, New York. 1996.

[Fol95] H. Folger et al. In: *Nucl. Instrum. Methods A* 362 (1995), p. 64. DOI: `10.1016/0168-9002(95)00527-7`.

[Gho50] S. N. Ghoshal et al. In: *Phys. Rev.* 80 (1950), p. 939. DOI: `10.1103/PhysRev.80.939`.

[Go4] *The Go4 Project*. `https://www.gsi.de/en/work/fairgsi/rare_isotope_beams/electronics/data_processing/data_analysis/the_go4_home_page.htm`.

[GSI] *GSI*. `https://www.gsi.de/`.

[Hal90] H. L. Hall and D. C. Hoffman. In: *J. Radioanal. Nucl. Chem.* 142 (1990), p. 53. DOI: `10.1007/BF02039453`.

[Hal92] H. L. Hall and D. C. Hoffman. In: *Annu. Rev. Nucl. Par. Sci.* 42 (1992), p. 147. DOI: `10.1146/annurev.ns.42.120192.001051`.

[Hel99] K. Helariutta et al. In: *Eur. Phys. J. A* 6 (1999), pp. 289–302. DOI: `10.1007/s100500050347`.

[Her08] R. D. Herzberg and P. T. Greenlees. In: *Prog. Part. Nucl. Phys.* 61 (2008), p. 674. DOI: `10.1016/j.ppnp.2008.05.003`.

[Hes05] F. P. Heßberger et al. In: *Eur. Phys. J. A* 26 (2005), p. 233. DOI: `10.1140/epja/i2009-10899-9`.

[Hes10] F. P. Heßberger et al. In: *Eur. Phys. J. A* 43 (2010), p. 55. DOI: `10.1140/epja/i2009-10899-9`.

[Hod00] E. Gadioli P. E. Hodgson and E. Gadioli Erba. *Introductory Nuclear Physics*. New York: Oxford University Press Inc., 2000. ISBN: 0-19-851989-3.

[Hof00] S. Hofmann and G. Münzenberg. In: *Rev. Mod. Phys.* 72 (2000), p. 733. DOI: `10.1103/RevModPhys.72.733`.

[Hof07] S. Hofmann et al. In: *Eur. Phys. J. A* 32 (2007), p. 251. DOI: `10.1140/epja/i2007-10373-x`.

[Hof12] S. Hofmann et al. In: *Eur. Phys. J. A* 48 (2012), p. 62. DOI: `10.1140/epja/i2012-12062-1`.

[Hof79] S. Hofmann et al. In: *Z. Phys. A* 291 (1979), p. 53. DOI: `10.1007/BF01415817`.

[Huy92] M. Huyse et al. In: *Phys. Rev. C* 46 (1992), p. 1209. DOI: `10.1103/PhysRevC.46.1209`.

[Isa11] P. Van Isacker. In: *J. Phys.: Conf. Ser.* 322 (2011), p. 012003. DOI: `10.1088/1742-6596/322/1/012003`.

[Jul01] R. Julin, K. Helariutta, and M. Muikku. In: *J. Phys. G* 27 (2001), R109. DOI: `10.1088/0954-3899/27/7/201`.

[Kal13] Z. Kalaninová et al. In: *Phys. Rev. C* 87 (2013), p. 044335. DOI: `10.1103/PhysRevC.87.044335`.

[Ket03] H. Kettunen et al. In: *Eur. Phys. J. A* 16 (2003), p. 457. DOI: `10.1140/epja/i2002-10130-9`.

[Kra88] K. S. Krane. *Introductory Nuclear Physics*. Hoboken: John Wiley and Sons, 1988. ISBN: 0-471-80553-X.

[Kug00] E. Kugler. In: *Hyperfine Interact.* 129 (2000), p. 23. DOI: `10.1023/A:1012603025802`.

[LISE] *Program LISE++*. `http://lise.nscl.msu.edu/lise.html`.
O. B. Tarasov and D. Bazin. In: *Nucl. Instrum. Methods B* 266 (2008) p. 4657. DOI: `10.1016/j.nimb.2008.05.110`.

[Lob68] K. E. G. Löbner. In: *Phys. Lett.* 26B (1968), p. 369. DOI: `10.1016/0370-2693(68)90614-X`.

[Maj86] A. Maj et al. In: *Z. Phys. A* 324 (1986), p. 123. DOI: `doi:10.1007/BF01325123`.

[Maj90] A. Maj et al. In: *Nucl. Phys. A* 509 (1990), p. 413. DOI: `doi:10.1016/0375-9474(90)90430-T`.

[Man88] L. G. Mann et al. In: *Phys. Rev. C* 38 (1988), p. 74. DOI: `10.1103/PhysRevC.38.74`.

[May79] T. Mayer-Kuckuk. *Fyzika atomového jádra*. Praha: SNTL - Nakladatelství technické literatury, 1979.

[Maz08] M. Mazzocco et al. In: *Nucl. Instrum. Methods B* 266 (2008), p. 3467.
DOI: `10.1016/j.nimb.2008.04.017`.

[Mol95] P. Möller et al. In: *At. Data and Nucl. Data Tables* 59 (1995), p. 185.
DOI: `10.1006/adnd.1995.1002`.

[Mun79] G. Münzenberg et al. In: *Nucl. Instrum. Methods* 161 (1979), p. 65.
DOI: `10.1016/0029-554X(79)90362-8`.

[NNDC] *National Nuclear Data Center*.
`http://www.nndc.bnl.gov`.

[Pol97] A. R. Poletti et al. In: *Nucl. Phys. A* 615 (1997), p. 95.
DOI: `10.1016/S0375-9474(96)00428-9`.

[Rei81] W. Reisdorf. In: *Z. Phys. A* 300 (1981), p. 227.
DOI: `10.1007/BF01412298`.

[Rei92] W. Reisdorf and M. Schädel. In: *Z. Phys. A* 343 (1992), p. 47.
DOI: `10.1007/BF01291597`.

[ROOT] *ROOT - An Object Oriented Data Analysis Framework*.
`https://root.cern.ch/`.
R. Brun and F. Rademakers. In: *Nucl. Instrum. Methods A* 389 (1997) p. 81.
DOI: `10.1016/S0168-9002(97)00048-X`.

[Ryt91] A. Rytz. In: *At. Data and Nucl. Data Tables* 47 (1991), p. 205.
DOI: `10.1016/0092-640X(91)90002-L`.

[San12] K. P. Santhosh, Jayesh George Joseph, and B. Priyanka. In: *Nucl. Phys. A* 529 (2012), p. 877.
DOI: `10.1016/j.nuclphysa.2012.01.009`.

[Sar96] Š. Šáro et al. In: *Nucl. Instrum. Methods A* 381 (1996), p. 520.
DOI: `10.1016/S0168-9002(96)00651-1`.

[Sch14] H. P. gen. Schieck. *Nuclear Reactions: An Introduction*. Springer-Verlag Berlin Heidelberg, 2014. ISBN: 978-3-642-53985-5.

[Shi10] Yue Shi et al. In: *Phys. Rev. C* 82 (2010), p. 044314.
DOI: `10.1103/PhysRevC.82.044314`.

[Suh07] J. Suhonen. *From Nucleons to Nucleus*. Springer-Verlag Berlin Heidelberg, 2007. ISBN: 978-3-540-48859-0.

[Sul07] B. Sulignano et al. In: *Eur. Phys. J. A* 33 (2007), p. 327.
DOI: `10.1140/epja/i2007-10469-3`.

[Tay96] R. B. E. Taylor et al. In: *Phys. Rev. C* 54 (1996), p. 2926.
DOI: `10.1103/PhysRevC.54.2926`.

[Vel03] K. Van de Vel et al. In: *Phys. Rev. C* 68 (2003), p. 054311.
DOI: `10.1103/PhysRevC.68.054311`.

[Wal99] P. Walker and G. Dracoulis. In: *Nature* 399 (1999), p. 35.
DOI: `10.1038/19911`.

[Wau93] J. Wauters et al. In: *Phys. Rev. C* 47 (1993), p. 1447.
DOI: `10.1103/PhysRevC.47.1447`.

[Wau94] J. Wauters et al. In: *Phys. Rev. Lett.* 72 (1994), p. 1329.
DOI: `10.1103/PhysRevLett.72.1329`.

[Xu04] F. R. Xu et al. In: *Phys. Rev. Lett.* 92 (2004), p. 252501.
DOI: `10.1103/PhysRevLett.92.252501`.

[You95] W. Younes et al. In: *Phys. Rev. C* 52 (1995), R1723.
DOI: `http://dx.doi.org/10.1103/PhysRevC.52.R1723`.

List of Publications

Publications in current contents:

- *Short-lived isomers in ^{192}Po and ^{194}Po*
  B. Andel, A.N. Andreyev, S. Antalic, F.P. Heßberger, D. Ackermann, S. Hofmann, M. Huyse, Z. Kalaninová, B. Kindler, I. Kojouharov, P. Kuusiniemi, B. Lommel, K. Nishio, R.D. Page, B. Sulignano, and P. Van Duppen
  Accepted to Phys. Rev. C (2016)

- *Alpha- and EC- decay measurements of ^{257}Rf*
  F.P. Heßberger, S. Antalic, A.K. Mistry, D. Ackermann, **B. Andel**, M. Block, Z. Kalaninová, B. Kindler, I. Kojouharov, M. Laatiaoui, B. Lommel, J. Piot, and M. Vostinar
  Submitted to Eur. Phys. J A (2016)

- *β-delayed fission of ^{230}Am*
  G.L. Wilson, M. Takeyama, A.N. Andreyev, **B. Andel**, S. Antalic, W.N. Catford, L. Ghys, H. Haba, F.P. Heßberger, M. Huang, D. Kaji, Z. Kalaninová, K. Morimoto, K. Morita, M. Murakami, K. Nishio, R. Orlandi, A.G. Smith, K. Tanaka, Y. Wakabayashi, and S. Yamaki
  To be submitted to Phys. Rev. C (2016)

- *Levels in ^{223}Th populated by α decay of ^{227}U*
  Z. Kalaninová, S Antalic, F.P. Heßberger, D. Ackermann, **B. Andel**, B. Kindler, M. Laatiaoui, B. Lommel and J. Mauer
  Phys. Rev. C **92**, 014321 (2015)

- *Evolution of fission-fragment mass distributions in the neutron-deficient lead region*
  L. Ghys, A.N. Andreyev, M. Huyse, P. Van Duppen, S. Sels, **B. Andel**, S. Antalic, A. Barzakh, L. Capponi, T.E. Cocolios, X. Derkx, H. De Witte, J. Elseviers, D.V. Fedorov, V.N. Fedosseev, F.P. Heßberger, Z. Kalaninová, U. Köster, J.F.W. Lane, V. Liberati, K.M. Lynch, B.A. Marsh, S. Mitsuoka, P. Möller, Y. Nagame, K. Nishio, S. Ota, D. Pauwels, R.D. Page, L. Popescu, D. Radulov, M.M. Rajabali, J. Randrup, E. Rapisarda, S. Rothe, K. Sandhu, M.D. Seliverstov, A.M. Sjödin, V.L. Truesdale,

C. Van Beveren, P. Van den Bergh, Y. Wakabayashi and M. Warda
Phys. Rev. C **90**, 041301(R) (2014)

- *Decay of* $^{201-203}$*Ra and* $^{200-202}$*Fr*
  Z. Kalaninová, S Antalic, A.N. Andreyev, F.P. Heßberger, D. Ackermann, **B. Andel**, L. Bianco, S. Hofmann, M. Huyse, B. Kindler, B. Lommel, R. Mann, R.D. Page, P.J. Sapple, J. Thomson, P. Van Duppen and M. Venhart
  Phys. Rev. C **89**, 054312 (2014)

- *α decay of the very neutron-deficient isotopes* $^{197-199}$*Fr*
  Z. Kalaninová, A.N. Andreyev, S Antalic, F.P. Heßberger, D. Ackermann, **B. Andel**, M.C. Drummond, S. Hofmann, M. Huyse, B. Kindler, J.F.W. Lane, V. Liberati, B. Lommel, R.D. Page, E. Rapisarda, K. Sandhu, Š. Šáro, A. Thornthwaite and P. Van Duppen
  Phys. Rev. C **87**, 044335 (2013)

- *New developments of the in-source spectroscopy method at RILIS/ISOLDE*
  B.A. Marsh, **B. Andel**, A.N. Andreyev, S. Antalic, D. Atanasov, A.E. Barzakh, B. Bastin, Ch. Borgmann, L. Capponi, T.E. Cocolios, T. Day Goodacre, M. Dehairs, X. Derkx, H. De Witte, D.V. Fedorov, V.N. Fedosseev, G.J. Focker, D.A. Fink, K.T. Flanagan, S. Franchoo, L. Ghys, M. Huyse, N. Imai, Z. Kalaninová, U. Köster, S. Kreim, N. Kesteloot, Yu. Kudryavtsev, J. Lane, N. Lecesne, V. Liberati, D. Lunney, K.M. Lynch, V. Manea, P.L. Molkanov, T. Nicol, D. Pauwels, L. Popescu, D. Radulov, E. Rapisarda, M. Rosenbusch, R.E. Rossel, S. Rothe, L. Schweikhard, M.D. Seliverstov, S. Sels, A.M. Sjödin, V. Truesdale, C. Van Beveren, P. Van Duppen, K. Wendt, F. Wienholtz, R.N. Wolf and S.G. Zemlyanoy
  Nucl. Instrum. Meth. B **317**, 550 (2013)

Other publications:

- *Production and decay spectroscopy of* ^{192}*Po and* ^{194}*Po*
  B. Andel
  AIP Conf. Proc. **1681**, 030012 (2015)

- *Nuclear structure studies in the seaborgium region at SHIP*
  S Antalic, F.P. Heßberger, **B. Andel**, D. Ackermann, S. Heinz, S. Hofmann, Z. Kalaninová, B. Kindler, J. Khuyagbaatar, M. Laatiaoui, B. Lommel, J. Piot and M. Vostinar
  AIP Conf. Proc. **1681**, 030013 (2015)

- *First Experimental Tests of the Modernized VASSILISSA Separator*
  A.V. Yeremin, A.G. Popeko, O.N. Malyshev, A. Lopez-Martens, K. Hauschild, O.

Dorvaux, B. Gall, V.I. Chepigin, A.I. Svirikhin, A.V. Isaev, E.A. Sokol, M.L. Chelnokov, A.N. Kuznetsov, A.A. Kuznetsova, A.V. Belozerov, K. Rezynkina, F. Dechery, F. Le Blanc, J. Piot, J. Gehlot, D. Tonev, E. Stefanova, D. Pantelika, C. Nita, **B. Andel**, S. Mulins, P. Jones and S. Ntshangase
Phys. Part. Nuclei Letters **12**, 35 (2015)

- *Experimental Tests of the Modernized VASSILISSA Separator (SHELS) with the Use of Accelerated* ^{50}*Ti Ions*
  A.V. Yeremin, A.G. Popeko, O.N. Malyshev, B. Gall, Z. Asfari, A. Lopez-Martens, K. Hauschild, O. Dorvaux, B.N. Gikal, S.L. Bogomolov, V.N. Loginov, A.E. Bondarchenko, V.I. Chepigin, A.I. Svirikhin, A.V. Isaev, E.A. Sokol, M.L. Chelnokov, A.N. Kuznetsov, A.A. Kuznetsova, Yu.A. Popov, K. Rezynkina, F. Dechery, **B. Andel**, S. Hofmann, J. Maurer, S. Heinz and J. Rubert
  Phys. Part. Nuclei Letters **12**, 43 (2015)

- *Total kinetic energy release in spontaneous fission of* ^{255,256,258}*Rf*
  F.P. Heßberger, D. Ackermann, **B. Andel**, S Antalic, C. Droese, J. Even, Z. Kalaninová, M. Laatiaoui, J. Piot and M. Vostinar
  GSI Scientific Report 2014, 165 (2015)

- *(11^{-}) isomeric state in* ^{194}*Po*
  B. Andel, A.N. Andreyev, S. Antalic, F.P. Heßberger, D. Ackermann, S. Hofmann, M. Huyse, Z. Kalaninová, B. Kindler, B. Lommel, R. Mann, K. Nishio, R.D. Page, B. Sulignano, and P. Van Duppen
  GSI Scientific Report 2014, 166 (2015)

- *Alpha decay of* ^{227}*U and excited levels in* ^{223}*Th studied at SHIP*
  Z. Kalaninová, S Antalic, F.P. Heßberger, D. Ackermann, **B. Andel**, B. Kindler, M. Laatiaoui, B. Lommel and J. Mauer
  GSI Scientific Report 2014, 167 (2015)

- *Direct proof of electron capture decay of* ^{258}*Db*
  F.P. Heßberger, D. Ackermann, **B. Andel**, S Antalic, C. Droese, J. Even, Z. Kalaninová, M. Laatiaoui, J. Piot and M. Vostinar
  GSI Scientific Report 2014, 177 (2015)

- *Decay of* $^{201-203}$*Ra*
  Z. Kalaninová, S Antalic, A.N. Andreyev, F.P. Heßberger, D. Ackermann, **B. Andel**, L. Bianco, S. Hofmann, M. Huyse, B. Kindler, B. Lommel, R. Mann, R.D. Page, P.J. Sapple, J. Thomson, P. Van Duppen and M. Venhart
  GSI Scientific Report 2013, 128 (2014)

- *Decay of* ^{200,201}*Fr*
  Z. Kalaninová, S Antalic, A.N. Andreyev, F.P. Heßberger, D. Ackermann, **B. Andel**, L. Bianco, S. Hofmann, M. Huyse, B. Kindler, B. Lommel, R. Mann, R.D. Page, P.J. Sapple, J. Thomson, P. Van Duppen and M. Venhart
  GSI Scientific Report 2013, 129 (2014)

- *Alpha Decay of* $^{197-199}$*Fr*
  Z. Kalaninová, A.N. Andreyev, S Antalic, F.P. Heßberger, D. Ackermann, **B. Andel**, M.C. Drummond, S. Hofmann, M. Huyse, B. Kindler, J.F.W. Lane, V. Liberati, B. Lommel, R.D. Page, E. Rapisarda, K. Sandhu, Š. Šáro, A. Thornthwaite and P. Van Duppen
  GSI Scientific Report 2012, 134 (2013)

- *Vplyv meteorologických parametrov na objemovú aktivitu radónu vo viacpodlažnom dome*
  M. Müllerová, **B. Andel**, and K. Holý
  Bezpečnost jaderné energie, Roč. 20(58), 215 (2012)

Conferences:

- *Production and* γ *spectroscopy of* ^{194,192}*Po*
  B. Andel, A.N. Andreyev, S. Antalic, F.P. Heßberger, D. Ackermann, S. Hofmann, M. Huyse, Z. Kalaninová, B. Kindler, B. Lommel, K. Nishio, R.D. Page, B. Sulignano, and P. Van Duppen
  21st Conference of Slovak Physicists, Nitra, Slovakia
  Book of Abstracts, p. 19 (2015)

- *Decay spectroscopy of* (11^-) *isomeric states in* ^{194}*Po and* ^{192}*Po*
  B. Andel, A.N. Andreyev, S. Antalic, F.P. Heßberger, D. Ackermann, S. Franchoo, S. Hofmann, M. Huyse, Z. Kalaninová, B. Kindler, I. Kojouharov, B. Lommel, R. Mann, K. Nishio, R.D. Page, J.J. Ressler, B. Streicher, B. Sulignano, and P. Van Duppen
  Zakopane Conference on Nuclear Physics, Zakopane, Poland
  Book of Abstracts, p. 151 (2014)

- *Alpha decay of* $^{197-199}$*Fr*
  Z. Kalaninová, A.N. Andreyev, S. Antalic, F.P. Hessberger, D. Ackermann, **B. Andel**, M.C. Drummond, S. Hofmann, M. Huyse, J. Lane, V. Liberati, B. Lommel, R.D. Page, E. Rapisarda, K. Sandhu, Š. Šáro, A. Thornthwaite, and P. Van Duppen

Shape Coexistence Across the Chart of the Nuclides, York, United Kingdom Book of Abstracts, p. 17 (2013)

- *Production and decay studies of* $^{197-202}$*Fr at SHIP*
  Z. Kalaninová, S. Antalic, A.N. Andreyev, F.P. Hessberger, D. Ackermann, **B. Andel**, M.C. Drummond, S. Hofmann, M. Huyse, J. Lane, V. Liberati, R.D. Page, E. Rapisarda, K. Sandhu, A. Thornthwaite, and P. Van Duppen
  Nuclear Structure and Related Topics, Dubna, Russia
  Book of Abstracts, p. 50 (2012)